



UNIVERSITY OF KWAZULU-NATAL

School of Physics

A thesis submitted in partial fulfillment of the requirements for the
degree of Master of Science

MODELLING DIODE-PUMPED SOLID-STATE LASERS

by

Edward H. Bernhardt

Supervisors:

Dr. Andrew Forbes
Dr. Christoph Bollig

August 2008

Declaration

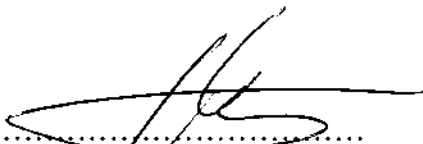
This dissertation describes the work undertaken at the CSIR National Laser Centre (Pretoria), while I was enrolled at the School of Physics, University of KwaZulu-Natal (Durban), under the supervision of Dr. Andrew Forbes and Dr. Christoph Bollig between January 2007 and April 2008.

I, the undersigned, hereby declare that the work reported in this dissertation to be my own research, unless specifically indicated to the contrary in the text. This dissertation has not been submitted in any form for any degree or examination to any other university.

Signed: 

On this... 22 ...day of... May2008

As the candidate's Supervisors we hereby certify that this statement is correct and that we agree with the submission of this dissertation.


.....
Dr. Andrew Forbes
(SUPERVISOR)


.....
Dr. Christoph Bollig
(CO-SUPERVISOR)

On this... 18day of... September2008

Abstract

This thesis consists of three main parts. An introduction to diode-pumped solid-state lasers, thermal modelling of solid-state lasers and rate-equation modelling of solid-state lasers.

The first part explains the basic components and operation principles of a typical diode-end-pumped solid-state laser. The stimulated emission process, solid-state laser gain media, various pump geometries and a basic end-pumped laser resonator configuration are among the topics that are explained.

Since thermal effects are one of the main limiting factors in the power-scaling of diode-pumped solid-state lasers, the second part of this thesis describes numerical and analytical thermal models that determine the thermal lens and thermally induced stresses in a laser crystal. As a first step, a time-independent numerical thermal model which calculates the three-dimensional temperature distribution in the laser crystal is implemented. In order to calculate the time dependent thermally induced stresses in a laser crystal, a coupled thermal-stress finite element analysis model was implemented. Even though some steady-state analytical solutions for simple crystal geometries do exist, the finite element analysis approach was taken so that the time dependent thermally induced stresses could be calculated for birefringent crystals of various geometries. In order to validate the numerical results, they are compared to experimental data and analytical solutions where possible.

In the last part, the population dynamics inside the laser gain medium are described and modelled with a quasi-three-level rate-equation model. A comprehensive spatially resolved rate-equation model is developed and discussed. In order to simplify the implementation of the rate-equation model as a computer simulation, the spatial dependence of the laser parameters is ignored so that the model reduces to a single-element plane-wave model. The simplified rate-equation model is implemented and solved numerically. The model is applied to a four-level CW and Q-switched Nd:YLF laser as well as a quasi-three-level QCW Tm:GdVO₄ laser. The models' predictions are thoroughly verified with experimental results and also with analytical solutions where possible.

Acknowledgements

There are so many people that I would like to thank for their support, encouragement and advice during the past year. In particular I want to express my endless gratitude towards :

My supervisors, Dr. Christoph Bollig and Dr. Andrew Forbes. Christoph, your passion for lasers already inspired me as an undergraduate student to pursue my post-graduate studies and career in laser physics. Thank you for teaching me everything I know about solid-state lasers. Andrew, I appreciate the fact that you were never too busy to help or to give advice. You are a great role-model and mentor.

Dr. Lourens Botha and Daniel Esser. Even though you weren't my official supervisors, you were always available to answer any questions. Daniel, thank you for the valuable comments on my dissertation.

All the staff at the National Laser Centre for creating a great academic working environment.

The National Laser Centre for the financial support that made my MSc possible. A special thanks for enabling me to present my work at the ASSP conference in Japan.

Andrew Mori, Melanie McLaren and Cobus Jacobs. You guys are great! AMD, thank you for always dreaming with me about the next rock face, bike trip, squirrel suit or which ever adventure we could think of. Melanie, thanks for your constant smile, cheerful attitude and the great coffee. Cobus, you were always keen to brainstorm about new ideas, thanks.

My parents, for all their encouragement, advice and love. Thank you for the great example that you have set to me throughout my life.

Michelle, my beautiful wife. You are the greatest blessing in my life. Thank you for your never ending support and love.

Contents

Abstract	i
Acknowledgements	ii
List of Figures	vi
List of Tables	ix
I Introduction to Diode-Pumped Solid-State Lasers	1
1 Introduction	2
1.1 Light Amplification by Stimulated Emission of Radiation	3
1.2 Solid-State Laser Gain Media	4
1.2.1 Host Materials	5
1.2.2 Active Ions	7
1.3 Diode-End-Pumping	7
1.4 Resonator	8
II Thermal Modelling of Solid-State Lasers	10
2 End-Pumped Solid-State Laser Thermal Model	11
2.1 Overview	11
2.2 Heat Diffusion Equation	12
2.2.1 Derivation	12
2.2.2 Heat Load	15
2.2.3 Analytical Solutions	17
2.2.4 Numerical Solutions	21
2.2.5 Comparison between Analytical and Numerical Solutions	24
2.3 Thermal Effects	27
2.3.1 Thermal Lensing	28

CONTENTS

2.3.2	Thermally Induced Stresses	29
3	Continuous Wave Pumped Nd:YAG Rod	31
3.1	Temperature Distribution	32
3.2	Thermal Lensing	36
3.3	Thermally Induced Stresses	38
3.4	Summary	42
4	Continuous Wave Pumped Nd:YAG Slabs	43
4.1	Analytical Equation for the Maximum Stress in an Anisotropic Slab . .	43
4.2	Power Scaling of Slabs	44
4.3	The Influence of the Pump Beam Size on the Critical Pump Power and Maximum Stress	44
4.4	Aspect Ratio of the Slab	47
4.5	Summary	48
5	Quasi-Continuous Wave Pumped Tm:YLF Rod	49
5.1	Single-Pulse	50
5.2	Duty Cycle	53
5.3	Summary	57
6	A Time-Dependent Analytical Thermal Model	59
III	Rate-Equation Modelling of Solid-State Lasers	62
7	Introduction to Rate-Equation Modelling	63
7.1	Overview	63
7.2	The Rate-Equation Approximation	64
7.3	Idealised Laser Models	65
7.3.1	Four-Level Lasers	65
7.3.2	Three-Level Lasers	66
7.4	Quasi-Three-Level Lasers	68
8	A Single-Element Plane-Wave Rate-Equation Model	72
8.1	Spatially Resolved Rate-Equation Model	72
8.1.1	Energy-Level Population Densities	72
8.1.2	Pump Light Distribution	74
8.1.3	Total Laser Photon Number and Laser Light Distribution	75
8.2	Single-Element Plane-Wave Approximation	76
8.2.1	Energy-Level Population Densities	76
8.2.2	Total Laser Photon Number	80

CONTENTS

8.3	Summary	81
9	Nd:YLF Laser	82
9.1	Experimental Setup	82
9.2	CW Operation	83
9.2.1	Threshold and Efficiency	83
9.2.2	Relaxation Oscillations	85
9.2.3	Output Coupler Transmission	88
9.3	Q-Switched Operation	89
9.3.1	Q-Switched Pulses	90
9.3.2	Average Power and Pulse Energy	94
9.4	Summary	95
10	Tm:GdVO₄ Laser	96
10.1	Experimental Setup	97
10.2	QCW Operation	97
10.2.1	Threshold and Efficiency	98
10.2.2	Relaxation Oscillations	101
10.2.3	Output Coupler Transmission	102
10.3	Summary	104
IV	Conclusion and Summary	106
A	Nd:YLF Laser Model - Additional Information	109
B	Tm:GdVO₄ Laser Model - Additional Information	112
	List of Publications	115
	References	117

List of Figures

1.1	An energy level representation of the pumping process.	4
1.2	An energy level representation of the stimulated emission process.	5
1.3	Neodymium doped YAG crystals.	6
1.4	Schematic diagram of side-pump and end-pump geometries.	8
1.5	Schematic diagram of a basic solid-state laser resonator.	9
2.1	A three-dimensional closed system.	14
2.2	A cylindrical rod, square rod and a slab gain media.	16
2.3	The transverse pump intensity profiles for various super-Gaussian coefficients.	18
2.4	The circularly symmetric transverse pump intensity profiles for various super-Gaussian coefficients.	19
2.5	An illustration of Euler's method.	22
2.6	An illustration of Euler's method.	22
2.7	A three-dimensional finite element discretization in ABAQUS.	24
2.8	The analytical temperature distribution in the Nd:YAG rod.	25
2.9	The temperature distribution on the pump face of the Nd:YAG rod.	26
2.10	A fractured Nd:YLF cylindrical crystal rod.	27
3.1	The transverse intensity profiles of the pump beams that are implemented in this chapter.	33
3.2	The calculated temperature profiles on the pump face of the Nd:YAG crystal.	34
3.3	The analytical temperature distribution in the Nd:YAG laser rod.	35
3.4	The variation of the thermal lens focal length and optical power with incident pump power.	37
3.5	The thermal lens focal length and optical power as a function of pump beam radius.	37
3.6	The stresses on the pump face of the Nd:YAG.	38
3.7	The analytical maximum stress in the Nd:YAG laser rod under lasing and non-lasing conditions.	40

LIST OF FIGURES

3.8	The critical incident pump power as a function of pump beam radius. .	41
3.9	The dependence of the maximum stress on the pump beam radius in the laser rod.	41
4.1	The maximum stress in the slab as a function of incident pump power.	45
4.2	The critical incident pump power as a function of pump beam size. . .	46
4.3	The dependence of the maximum stress in the slab on the pump beam size.	46
4.4	The critical pump power as a function of the aspect ratio of the slab. .	47
5.1	The numerical temperature and stress distributions in the Tm:YLF rod.	51
5.2	The analytical values for the maximum stress in the Tm:YLF rod as a function of incident pump power.	52
5.3	The maximum stress in the YLF rod during a single 10 ms QCW pump pulse with a peak power of 200W.	53
5.4	The maximum stress intensity as a function of time for various incident pump powers.	54
5.5	The critical incident pump power as a function of a single QCW pump pulse duration.	54
5.6	The time dependence of the maximum tensile stress in the Tm:YLF rod that are induced by various QCW pump powers and duty cycles. . . .	55
5.7	The average pump power at which fracture occurs, as a function of pump duty cycle.	56
5.8	The incident peak power at which fracture occurs as a function of pump duty cycle.	57
6.1	The temperature in the centre of the Tm:YLF rod as a function of time while the rod is subjected to a QCW-pump.	60
6.2	The temperature in the centre of the Tm:YLF rod as a function of time while the rod is subjected to a QCW-pump.	61
7.1	A schematic diagram of an idealised four-level laser model.	65
7.2	A schematic diagram of an idealised three-level laser model.	67
7.3	The energy diagram of Tm:YAG.	69
7.4	A schematic diagram of a quasi-three-level laser model.	70
8.1	A schematic diagram of a quasi-three-level laser model.	73
8.2	A comparison between the laser gain medium in the spatially resolved and single-element plane-wave models.	77
8.3	A schematic diagram of the resonator.	79
9.1	The experimental setup of the Nd:YLF laser.	83

LIST OF FIGURES

9.2	Power scaling of the Nd:YLF laser.	84
9.3	The total laser photon number and upper manifold population density of the Nd:YLF laser during the main relaxation oscillation spikes.	85
9.4	The relaxation oscillation spikes at full pump power.	87
9.5	Relaxation oscillation pulses according to the rate-equation model at two different periods during the relaxation oscillation process.	88
9.6	The laser power as a function of output coupler transmission.	89
9.7	An example of the modulated loss that the AOM introduces in the resonator.	90
9.8	A single Q-switched pulse along with the population density.	91
9.9	An oscilloscope trace of a single pulse along with a pulse as produced by the rate-equation model.	92
9.10	The pulse train during Q-switch operation as produced by the rate-equation model.	93
9.11	The population density of N_2 during Q-switch operation as delivered by the rate-equation model.	93
9.12	The average power and pulse energy of the laser as a function of pulse repetition frequency.	94
10.1	The cross-relaxation process in Tm^{3+}	97
10.2	The experimental setup of the Tm:GdVO ₄ laser (Esser <i>et al.</i> , 2008).	98
10.3	The laser threshold as a function of wavelength for various output couplers.	99
10.4	Power scaling of the Tm:GdVO ₄ laser.	100
10.5	The relaxation oscillations of the Tm:GdVO ₄ laser at an incident pump power of 37.3 W.	101
10.6	The population inversion density during the relaxation oscillations of the Tm:GdVO ₄ laser.	102
10.7	The Tm:GdVO ₄ laser wavelength as a function of output coupler transmission.	103
10.8	The output power of the Tm:GdVO ₄ laser as a function of the output coupler transmission.	104
A.1	The effective absorption cross-sections of Nd:YLF.	110
A.2	The effective emission cross-sections (sigma-polarization) of Nd:YLF.	111
B.1	The effective absorption cross-sections of Tm:GdVO ₄	113
B.2	The effective absorption and emission cross-sections of Tm:GdVO ₄	114

List of Tables

2.1	Input parameters that were used for the calculation of the temperature in the Nd:YAG.	25
3.1	Input parameters for the calculation of thermal effects in this chapter. .	32
5.1	Input parameters that are used for the calculations in this chapter. . .	50
A.1	The parameters of the Nd:YLF laser that were used in the rate-equation model.	109
B.1	The parameters of the Tm:GdVO ₄ laser that were used in the rate-equation model.	112

Part I

Introduction to Diode-Pumped Solid-State Lasers

Chapter 1

Introduction

A laser is a device that has the ability to generate or amplify spatially and temporally coherent radiation at frequencies which include the largest part of the electromagnetic spectrum (Siegman, 1986). Due to the high coherence of laser light it is possible to achieve much higher intensities than conventional light sources such as lamps, which emit radiation in all directions. Another characteristic of laser light is the fact that it is monochromatic.

The operation of a laser is governed by the way in which electromagnetic radiation interacts with matter. The specific process is known as stimulated emission. It is from this interaction process where the term **LASER** has its origin. It is an acronym for **L**ight **A**mplification by **S**timulated **E**mission of **R**adiation.

The first operation of a laser was that of a solid-state laser which was demonstrated in the form of a Cr^{3+} doped sapphire laser (Maiman, 1960). Since this first laser, several other types of gain media, including gas, liquid, chemical and nuclear have been used for laser operation with emission wavelengths that can range from the ultraviolet, through the visible region, all the way to the infrared part of the electromagnetic spectrum. Its unique attributes have ensured that lasers have found numerous applications in the medical, scientific, military and industrial fields. The ever increasing demand in laser applications ensures that the development of high power diode-pumped solid-state lasers remains a very active area of research.

Even though numerous variations of lasers exist, the work presented in this thesis considers diode-end-pumped solid-state lasers in particular. This specific type of solid-state laser and pump geometry are of great interest due to the many advantages that it possess. Some of the advantages of diode-pumped solid-state lasers include (Fan & Byer, 1988): A higher efficiency than lamp-pumped lasers; Enhanced peak powers due to the long upper state lifetimes; A simpler design than lamp-pumped lasers due to its simpler cooling geometry; A higher brightness than conventional diode lasers; Sharper emission spectra than diode lasers; Very good laser beam quality with nearly diffraction-limited operation.

The main purpose of the work presented here, is to use existing laser theory in order to develop mathematical models that can be implemented in the form of a computer simulation of the laser. Two main models are developed: A thermal model of a diode-end-pumped solid-state laser that can explain and predict the thermal effects such as thermal lensing and thermally induced stresses in these lasers. The second model is a rate-equation model that depicts the behaviour of the population dynamics in the laser gain medium.

Before the models are developed and discussed in later chapters, the rest of this chapter is devoted to explaining the basic components and operation principles of diode-pumped solid-state lasers.

1.1 Light Amplification by Stimulated Emission of Radiation

As mentioned before, the process which governs the operation of a laser is a process known as stimulated emission.

Atomic systems such as atoms and ions can only exist in discrete energy levels. When such an atomic system changes from one energy level to another, it is associated with the absorption or emission of a photon (Koechner, 1996). The frequency of this photon is proportional to the energy difference between the two energy levels and can be described by the Bohr frequency relation

$$E = h\nu \tag{1.1}$$

where $E = E_2 - E_1$ is the energy difference between the two energy levels, h is Planck's constant and ν is the frequency of the emitted or absorbed photon which can interact with the system.

At thermal equilibrium, the population of the energy levels in an atomic system can be described by a Maxwell-Boltzmann distribution so that the lower energy levels have a higher population than the higher energy levels. When a photon with frequency ν , as described in equation 1.1, interacts with the atomic system, the atom/ion is raised into a higher energy level while the photon is absorbed. In a laser context, this absorption process which excites atoms/ions from a lower energy state into a higher more energetic state is referred to as "pumping" the gain medium (see Figure 1.1). Note that the pumping process as it is referred to in this work refers to optically pumped lasers. There are other laser pumping techniques such as electrical and chemical pumping of which the details will not be discussed in the context of this work.

For laser action to occur, the gain medium has to be pumped so that a condition of "population inversion" is achieved. Population inversion is the state where more ions/atoms are in some higher quantum energy level than in some lower level in the laser

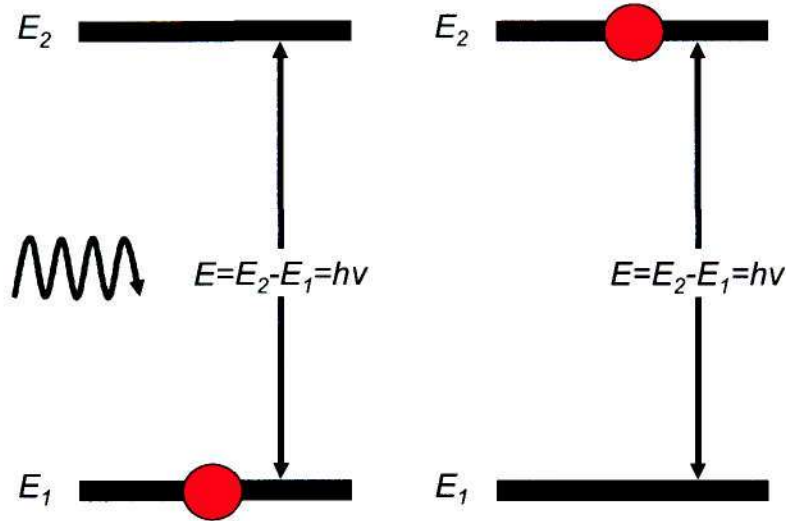


Figure 1.1: An energy level representation of the pumping process.

gain medium (Siegman, 1986). The pump process can be used to achieve population inversion in the gain medium since the upper laser levels in most lasers are metastable energy levels (relatively long lifetimes) (Siegman, 1986). The pumping process is thus a way to deposit energy in the laser gain medium which can in turn be extracted via the laser beam.

Once population inversion in the gain medium has been achieved, it is possible to amplify electromagnetic radiation of a specific frequency via the process of stimulated emission as it passes through the gain medium. When a photon of the correct frequency is incident on the population inverted gain medium, it will cause the atoms/ions in the higher energy level to fall down to some lower energy level while an additional photon is emitted (see Figure 1.2). The emitted photon is indistinguishable from the incident photon since it has the same direction, frequency, phase and polarization (Koechner, 1996). This amplification process forms the foundation of how a laser operates.

1.2 Solid-State Laser Gain Media

In order for a material to be a suitable laser gain medium, it must have sharp fluorescent emission lines, strong absorption bands and an adequate quantum efficiency for the particular fluorescent transition that is of interest (Koechner, 1996). A further requirement is that the pump band of the gain medium falls within the emission

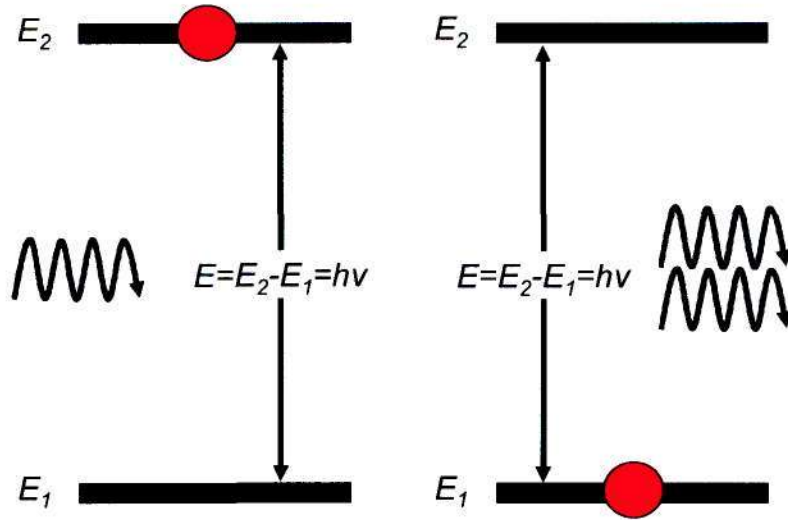


Figure 1.2: An energy level representation of the stimulated emission process.

spectrum of a pump source which is readily available. These particular features can generally be found in optically transparent solids, such as crystal, glass or ceramic, which contain a small amount of an active element, such as rare earth ions, in which optical transitions can occur. Due to the nature of this work, only solid-state gain media will be considered.

1.2.1 Host Materials

It is of utmost importance that the host material must have very good optical, mechanical and thermal properties in order to survive the harsh operating conditions of lasers. The key criteria for selecting a laser active ion host are summarized as follow (Koechner, 1996):

- The host must possess good optical properties. This includes a homogeneous refractive index to ensure a good beam quality. Ideally the temperature dependence of the refractive index should be as small as possible to reduce the effect of thermal lensing under severe pumping conditions. Another requirement is that the scattering losses in the host should be minimal in order to restrict the overall losses in the gain medium.
- The host should have mechanical and thermal properties that will allow high-power operation without being subject to excessive stresses, and ultimately frac-

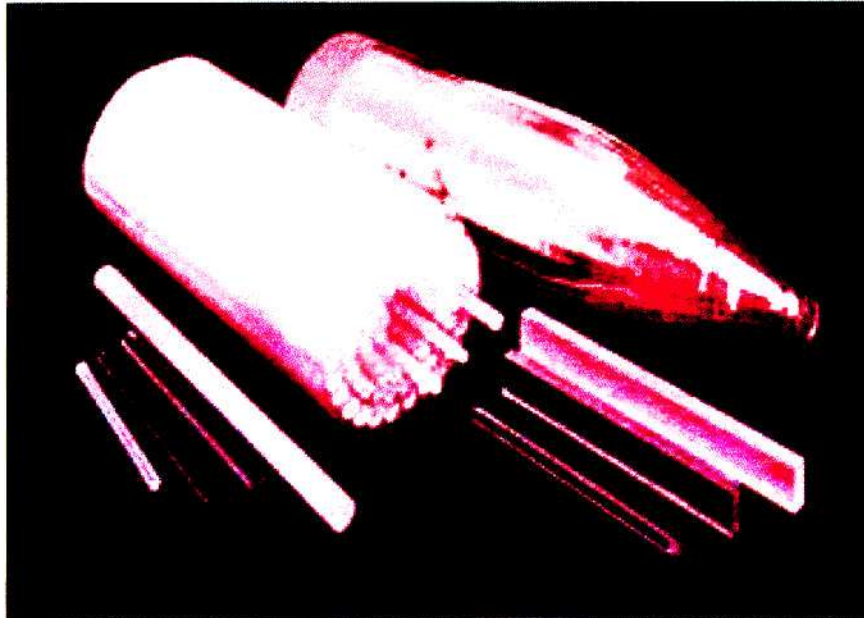


Figure 1.3: Neodymium doped YAG crystals (VLOC YAG Brochure, 2008).

ture, due to the thermal load. A high thermal conductivity is thus of great importance.

- The host must have lattice sites that are able to accept the dopant ions. The effect of the local crystal field must be such that it induces the required spectroscopic properties.
- It must be possible to grow the host to adequate sizes while still maintaining a good optical and mechanical quality.

There are three primary groups of solid-state host materials which possess the above mentioned qualities: single crystals, glasses and ceramics. Of these host gain media, Neodymium doped yttrium aluminium garnet ($Y_3Al_5O_{12}$, referred to as YAG) single crystals are the most widely used solid-state laser gain media. See Figure 1.3 for examples of single crystal gain media (YAG) doped with rare earth ions (Neodymium).

Due to the recent advances in the ceramic manufacturing process, high quality, high transparent ceramics with much lower scattering losses can be fabricated (Qi *et al.*, 2005). The optical absorption, fluorescence and emission spectra as well as physical properties of ceramics have been measured and compared with those of single crystals. The ceramic features seem to compare very well with that of the single crystals (Kracht *et al.*, 2005) (Kumar *et al.*, 2004) (Qi *et al.*, 2005).

1.2.2 Active Ions

Rare earth (lanthanide) ions are very good candidates to act as active ions in solid-state laser materials since they possess numerous sharp emission lines throughout most of the visible and infrared part of the electromagnetic spectrum (Koechner, 1996). The emission lines remain very sharp, even in the presence of a local crystal field (Stark effect), due to the shielding of the outer electrons.

The outermost electrons of these ions form a complete rare gas shell, which is the xenon shell with two $5s$ and six $5p$ electrons (Koechner, 1996). Inside this xenon shell is the $4f$ shell. While the $4f$ shells remains incomplete (i.e. not filled with 14 electrons), electrons that are already present in the $4f$ shell can be raised into these empty levels by light absorption. The sharp absorption and emission lines that are observed in rare earth ions are due to these particular transitions which are shielded by the outer xenon shell (Koechner, 1996).

Rare earth ions are used in solid-state laser gain media in either a divalent or trivalent form. A divalent rare earth ion is formed when the atom loses its outer $6s$ electrons. Additionally, a trivalent ion also gives up the $5d$ electron, or if it has none, it gives up one of the $4f$ electrons (Koechner, 1996).

The specific rare earth ions that are considered in this work includes trivalent Neodymium (Nd^{3+}), Thulium (Tm^{3+}) and Holmium (Ho^{3+}).

1.3 Diode-End-Pumping

The two main methods which are used to optically pump solid-state gain media are lamp-pumping and diode-pumping. Diode-pumped lasers are more efficient than lamp-pumped lasers due to the fact that the diode lasers that are used for pumping have a much narrower spectral output (Fan, 1995). This makes it possible to select a pumping source with a very good overlap with the gain medium's absorption band without wasting too much of the pump radiation at wavelengths that are not absorbed by the gain medium.

Another advantage of using diode-pumping instead of lamp-pumping is that diode-pump systems usually lead to a lower thermal load in the gain medium (Fan, 1995) (Chen *et al.*, 1990). A lower thermal load in the gain medium will result in lower thermally induced stresses. Due to the directionality and high radiance of diode-lasers, a higher pump power density can also be achieved than with lamp-pumped lasers.

Flash lamp pump and diode-pump sources can be implemented in a variety of geometries of which only side-pump and end-pump geometries will be considered in this work (Figure 1.4). In a side-pump setup the pump light is radiated perpendicular to the laser mode into the gain medium. In the case of an end-pump geometry, the pump light is inserted parallel to the laser mode.

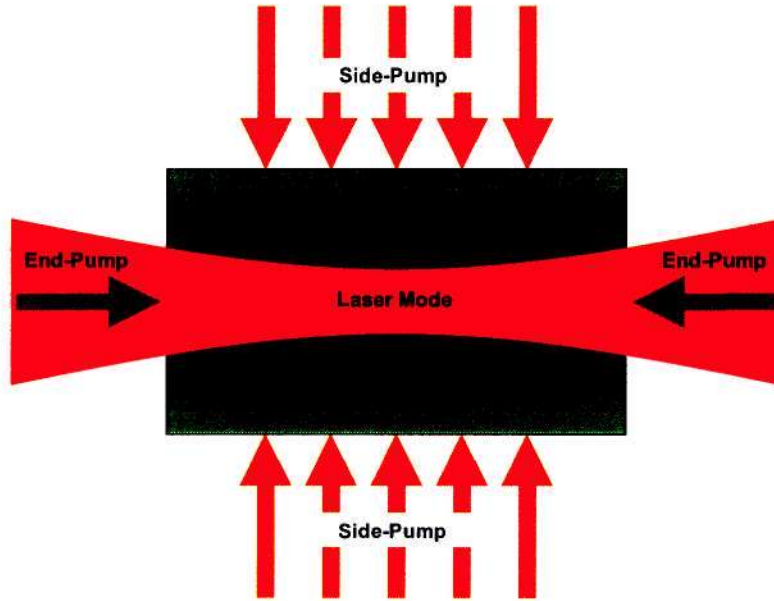


Figure 1.4: Schematic diagram of side-pump and end-pump geometries.

End pump geometries allow a very good spatial overlap between the pump radiation and the fundamental TEM_{00} transverse laser mode inside the gain medium which makes them more efficient than side-pump geometries (Rustad, 1994). Other very attractive features of end-pumped lasers include a very compact design with high beam quality (Koechner, 1996). The fact that a good laser beam quality along with a high efficiency can be achieved simultaneously with an end-pumped geometry makes end-pumped lasers very attractive.

All the lasers that are considered throughout the rest of this work, have been diode-end-pumped.

1.4 Resonator

In its most elementary form, an optical resonator consists of two opposing mirrors with the laser gain medium placed in between them (Figure 1.5). One of these mirrors will usually be $\sim 100\%$ reflective at the laser wavelength, while the other is partially transmissive at the laser wavelength. For an end-pump configuration, the former is referred to as the pump mirror while the latter is called the output coupler.

Once population inversion in the gain medium has been achieved through optical

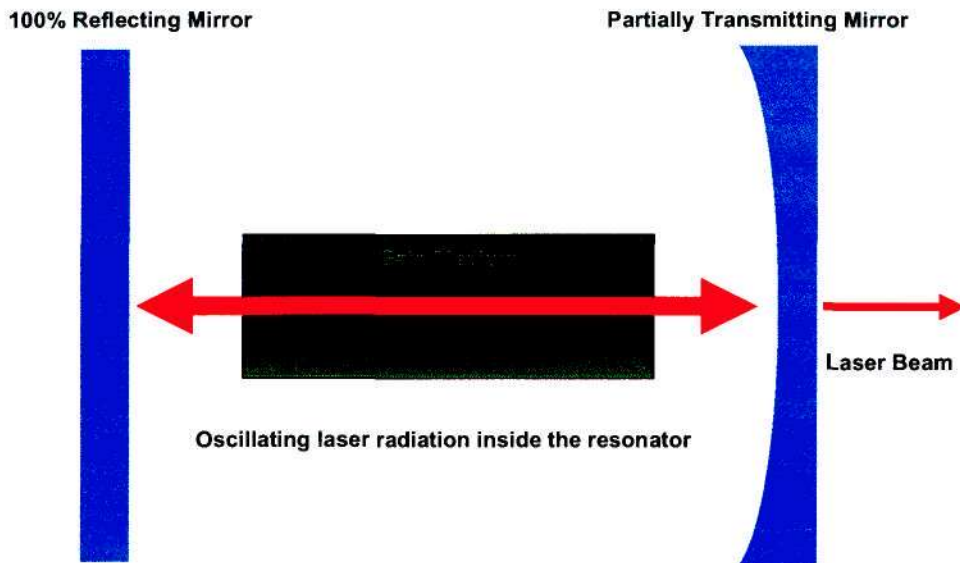


Figure 1.5: Schematic diagram of a basic solid-state laser resonator.

pumping, it is possible to amplify electromagnetic radiation of a specific frequency via the process of stimulated emission as it passes through the gain medium. Laser radiation which has been initiated by a spontaneously emitted photon along the optical axis of the resonator is reflected between the two mirrors (assuming that the resonator is aligned). Each time the radiation passes through the laser gain medium it is further amplified by stimulated emission. If the net laser amplification in the gain medium exceeds the net loss in the system (including scattering and output coupler losses), coherent optical oscillations will build up in the resonator (Siegman, 1986). Since the output coupler is partially transmissive at the laser wavelength, a monochromatic and highly directional beam of laser radiation is coupled out of the resonator.

Part II

Thermal Modelling of Solid-State Lasers

Chapter 2

End-Pumped Solid-State Laser Thermal Model

2.1 Overview

Thermal effects remain one of the main factors that limit power scaling of diode-end-pumped solid-state lasers (Pfister *et al.*, 1994). The importance of the thermal effects in solid-state lasers ensured that it remained a very popular research topic over the last couple of decades and it drew the attention of many laser physicists.

Some of the earliest pioneering work in thermal effects in solid-state lasers was done by Koechner. He starts by publishing experimental data for thermally induced stress-birefringence in Nd:YAG crystals (Koechner & Rice, 1970). Koechner then calculated analytical solutions for temperature distribution, thermally induced stresses and thermal lensing in the case of a uniformly pumped laser gain medium (Koechner, 1988). The temperature profile for a uniformly pumped laser rod was found to be parabolic within the rod. The thermally induced stresses that are induced by this temperature gradient were calculated and the maximum tensile stress in the rod was found to occur on the surface of the rod, in the tangential direction.

In analogy to Koechner's model of a uniformly pumped rod, Egglestone developed a model to determine the temperature and stress distributions in uniformly pumped infinite-length Nd:YAG and Nd:glass slabs (Egglestone *et al.*, 1984). A very important relation which predicts the maximum pump power at which fracture will occur in a uniformly pumped slab is derived. The fracture power can be expressed as a function of the fracture pump power of a uniformly pumped rod as well as the aspect ratio of the slab.

Cousins presented a steady state analytical model to calculate temperature and stress in thin edge- and face-cooled disks by making use of cylindrical symmetry (Cousins, 1992). Yan applied Cousins' approach to a top-hat pumped laser rod of

finite length (Yan & Lee, 1994). The analytical stress distribution throughout the rod was presented. Similar to Koechner's result for a uniformly-pumped rod of finite length, the maximum stress in the rod was found to occur on the surface of the rod (Yan & Lee, 1994). A very interesting conclusion from this work by Yan was that the maximum stress in the laser rod is nearly independent of pump beam size in the case where the pump beam radius is much smaller than the rod radius. Yan verified this statement with experimental data.

The abovementioned analytical models are very useful to estimate the influence of the laser crystal geometry and material parameters on the thermal effects. However, all the existing analytical models are restricted to continuous-wave pumped isotropic crystal hosts with very basic gain medium geometries.

With the modern advances in the processing power and memory of computers, finite element analysis (FEA) has become a very powerful alternative to analytical solutions. This approach allows the calculation of numerical solutions for arbitrary gain materials and geometries as well as various pump setups and cooling methods which are usually much closer to reality than the often crude assumptions in analytical models.

Pfistner did some of the earliest work on numerical simulations of thermal and stress distributions in anisotropic Nd:YLF laser rods (Pfistner *et al.*, 1994). He found that higher doping concentrations lead to a better spatial mode overlap of the pump, but also induced a stronger thermal lens. He also concluded that a face-cooled laser rod had higher induced stresses.

Paschotta used FEA to investigate the thermal effects in laser media with a slab geometry (Paschotta *et al.*, 2000). A key result from this work is that the induced stresses in the slab are very strongly dependent on the horizontal pump beam size along the width of the slab, while there is a negligible dependence on the vertical pump beam size.

In the work presented here, both analytical and numerical solutions of thermal effects are discussed in detail and compared to each other as well as experimental results.

2.2 Heat Diffusion Equation

2.2.1 Derivation

The temperature distribution in a solid-state laser gain medium is described by the three-dimensional heat diffusion equation. In this section, the heat diffusion equation will be derived from first principles. This derivation is very similar to the approach taken by (Lienhard & Lienhard, 2008).

From the first law of thermodynamics it follows that for a closed system

$$\frac{dU}{dt} = Q - W \quad (2.1)$$

where U is the total energy in the system, Q is the heat that enters the system and W is the work that is done by the system. The derivative is taken with respect to the time, t . Assume that the system does no work. Equation 2.1 now reduces to

$$\frac{dU}{dt} = Q \quad (2.2)$$

Let the closed system be an arbitrary three-dimensional volume that is at rest (see Figure 2.1). Note that the term “closed system” as it is used here, refers to a system that can exchange heat and work with its surroundings, but no matter.

The surface is denoted as S , while the volume is denoted as R . Let a surface and volume element be dS and dR respectively. There are two vectors defined on dS as illustrated in Figure 2.1. One of them is the unit normal vector \vec{n} (with $|\vec{n}| = 1$), while the other is the heat flux vector, $\vec{q} = -k\nabla T$, at that point on the surface, according to Fourier’s law, with k the thermal conductivity and T the temperature. This vector points in the direction where the temperature gradient is the highest. Further, allow for a volumetric heat release to be distributed throughout the volume R . This volumetric heat is denoted by \tilde{q} .

The heat conducted out of a surface area dS can be written as

$$(-k\nabla T) \cdot (\vec{n}dS) \quad (2.3)$$

where the dot product selects the component of the heat flux that is perpendicular to the surface of ds . To get the total heat that is added to the volume R , the heat that is generated in R should be added to the heat that flows into S . The total heat addition into R is now

$$Q = - \int_S (-k\nabla T) \cdot (\vec{n}dS) + \int_R (\tilde{q})dR \quad (2.4)$$

The total internal energy in the system can be written as

$$U = \int_R (\rho u)dR \quad (2.5)$$

where ρ is the density of the material and $u = cT$ is the energy per mass with c the material’s specific heat capacity and T the material’s absolute temperature in Kelvin. It follows from equation 2.5 that

$$\frac{dU}{dt} = \int_R \left(\rho c \frac{\partial T}{\partial t} \right) dR \quad (2.6)$$

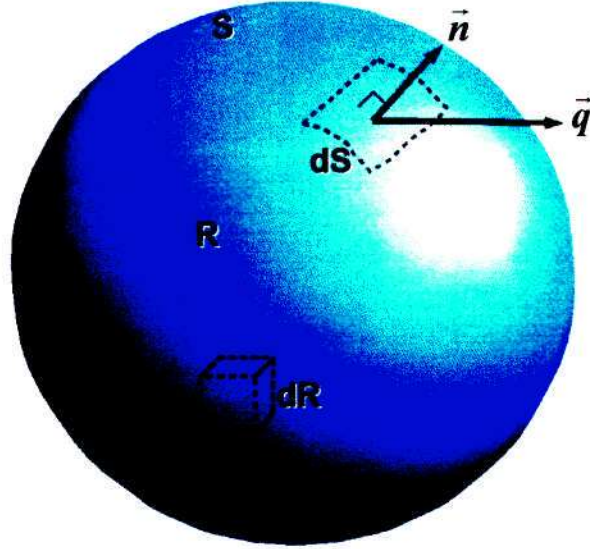


Figure 2.1: An arbitrary three-dimensional volume that is considered to be a closed system.

If equations 2.4 and 2.6 are substituted into equation 2.2 then

$$\int_S (k\nabla T) \cdot (\vec{n}dS) = \int_R \left(\rho c \frac{\partial T}{\partial t} - \tilde{q} \right) dR \quad (2.7)$$

From Gauss' theorem it follows that

$$\int_S \vec{A} \cdot (\vec{n}dS) = \int_R (\nabla \cdot \vec{A}) dR \quad (2.8)$$

By making use of Gauss' theorem, the surface integral on the left side of equation 2.7 can be converted into a volume integral so that equation 2.7 now becomes

$$\int_R \left(\nabla \cdot k\nabla T - \rho c \frac{\partial T}{\partial t} + \tilde{q} \right) dR = 0 \quad (2.9)$$

Since the volume R was chosen to be arbitrary, the integrand must be zero. This leads to the three-dimensional heat diffusion equation

$$\rho c \frac{\partial T}{\partial t} = \tilde{q} + k\nabla^2 T \quad (2.10)$$

This is the equation that is used to calculate the three-dimensional transient temperature profiles in the laser gain media.

2.2.2 Heat Load

The energy that is deposited into the gain medium via the optical pump and is not in turn released in the form of emission (such as fluorescence and laser emission) is converted into heat. The heat generation in the laser gain medium is mainly due to non-radiative energy transitions that are associated with

- The energy difference between the pump and laser photons (also known as quantum defect heating)
- Absorption of the pump light into energy levels other than the intended pump level
- Upconversion processes such as energy transfer upconversion (ETU) and excited state absorption (ESA) into higher energy levels and the subsequent non-radiative decay out of the higher levels
- Spontaneous non-radiative decay from the upper laser level

For a typical 1% doped Nd:YAG laser, about 35 – 40% of the absorbed pump power is converted into heat under the condition of no laser extraction (Fan, 1993)(Weber *et al.*, 1999). Roughly 25% is due to the quantum defect, while the additional contributions are responsible for the remaining 10–15% (Weber *et al.*, 1999). Under lasing conditions the heat load reduces to 24% of the absorbed pump power (Fan, 1993).

The ability to efficiently extract the generated heat from the gain medium is one of the main considerations that dominates the laser design, especially for high average-power systems (Koechner, 1996).

In general, the heat density \tilde{q} (units $\text{W}\cdot\text{m}^{-3}$), that is added to a laser gain medium via the pump radiation can be described by (Clarkson, 2001)

$$\tilde{q}(x, y, z) = \alpha\eta I_p(x, y, z) \quad (2.11)$$

where η is the percentage of absorbed pump power that is converted into heat, α is the absorption coefficient of the crystal and $I_p(x, y, z)$ is the intensity of the pump radiation. The pump intensity profile is dependent on the pump delivery system. In this work, two typical pump delivery systems are considered, diode-stack- and fibre-coupled pumping.

In the following two sections the transverse intensity profile of the pump beam is defined in the $x - y$ plane while z is the direction of pump light propagation (see Figure 2.2).

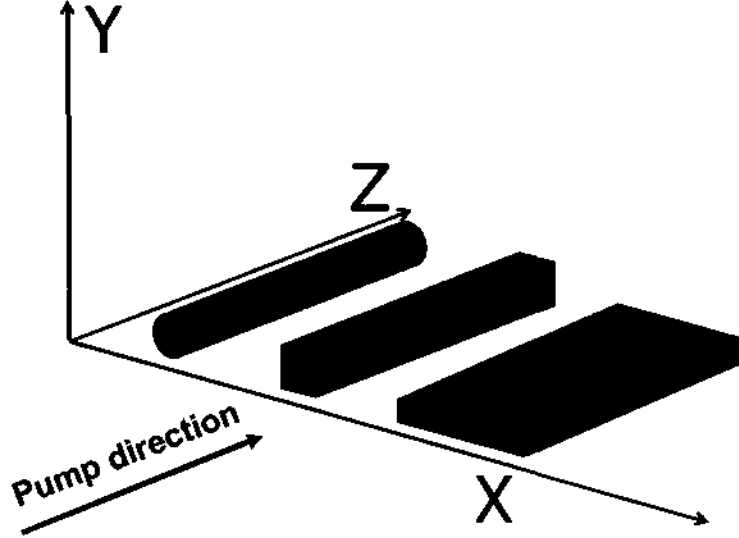


Figure 2.2: The coordinate system that is used when defining the pump beam intensity profiles. From left to right is a cylindrical rod, square rod and a slab.

Diode-Stack Pumping

For the discussion that is about to follow, the pump beam is considered to be collimated inside the laser gain medium. Since the lengths of all the laser gain media that are considered in this work are well within the Rayleigh length of the pump beams, this is a valid assumption. The Rayleigh length is the distance from the waist of the beam to a point along the propagation direction where the cross-sectional area of the beam is doubled.

In the case of diode-stack pumping, it is not unusual that the pump beam waist in the x and y directions are different due to the properties of the diode-stack. In this case the pump light intensity can be described by (LASCAD, 2008)

$$I_p(x, y, z) = P_p e^{-\alpha z} C e^{-2 \left(\left| \frac{x}{w_x} \right|^{SG_x} + \left| \frac{y}{w_y} \right|^{SG_y} \right)} \quad (2.12)$$

where P_p is the pump power that is incident on the gain medium and C is a normalisation factor so that transverse distribution of the pump intensity is normalised. From this condition it follows that

$$\int_{-\infty}^{\infty} \int_{-\infty}^{\infty} C e^{-2 \left(\left| \frac{x}{w_x} \right|^{SG_x} + \left| \frac{y}{w_y} \right|^{SG_y} \right)} dx dy = 1 \quad (2.13)$$

This implies that

$$C = \frac{SG_x SG_y}{4\Gamma\left(\frac{1}{SG_x}\right)\Gamma\left(\frac{1}{SG_y}\right)2^{-\left(\frac{1}{SG_x}+\frac{1}{SG_y}\right)}w_x w_y} \quad (2.14)$$

where SG_x and SG_y are the super-Gaussian coefficients for the x and y directions respectively ($SG = 2$ for a perfect Gaussian beam and $SG \rightarrow \infty$ for a top-hat beam), Γ is the gamma-function and w is the pump beam radius (with the x and y subscripts indicating the particular direction).

If the pump beam radii in the x and y directions are equal and $SG_x = SG_y = SG$, then equation 2.14 reduces to

$$C = \frac{SG^2\left(2^{\frac{1}{SG}}\right)^2}{4\Gamma\left(\frac{1}{SG}\right)^2 w_p^2} \quad (2.15)$$

As an example, consider the the transverse pump intensity profiles with various super-Gaussian coefficients that are incident on a $2 \times 2 \text{ mm}^2$ crystal face (see Figure 2.3). The beam radii are 0.2 mm and 0.6 mm in the x and y directions respectively. These intensity profiles are typical of a pump beam that is produced by a diode-stack.

Fibre-Coupled Pumping

For fibre-coupled pumping a circular symmetric pump beam is assumed. In analogy to the previous section, the general transverse pump intensity profile is defined as

$$I_p(x, y, z) = P_p e^{-\alpha z} C e^{-2\left|\frac{\sqrt{x^2+y^2}}{w_p}\right|^{SG}} \quad (2.16)$$

or in cylindrical coordinates

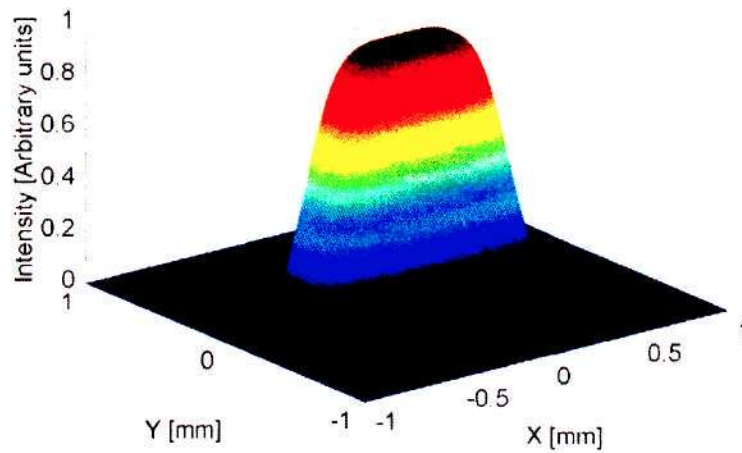
$$I_p(r, z) = P_p e^{-\alpha z} C e^{-2\left|\frac{r}{w_p}\right|^{SG}} \quad (2.17)$$

As an example, consider the the transverse pump intensity profiles (with various super-Gaussian coefficients) that are incident on a $2 \times 2 \text{ mm}^2$ crystal face (see Figure 2.4). The pump beam radius is 0.5 mm.

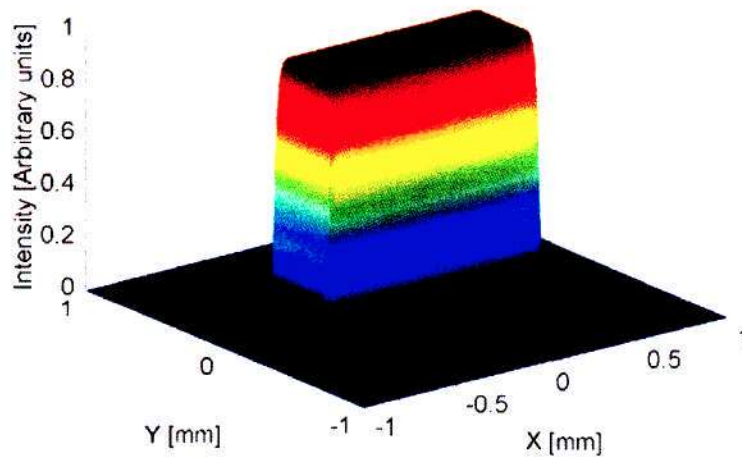
It is generally considered that a top-hat transverse intensity profile is a very good approximation for a fibre-coupled diode pump where the fibre face is imaged onto the laser crystal (Chénais *et al.*, 2004). For this reason, only analytical solutions for a top-hat pump beam will be discussed in the next section.

2.2.3 Analytical Solutions

A great advantage of analytical solutions is that the influence of various parameters can be analyzed directly by evaluating the analytical expression (Schmid *et al.*, 2000).

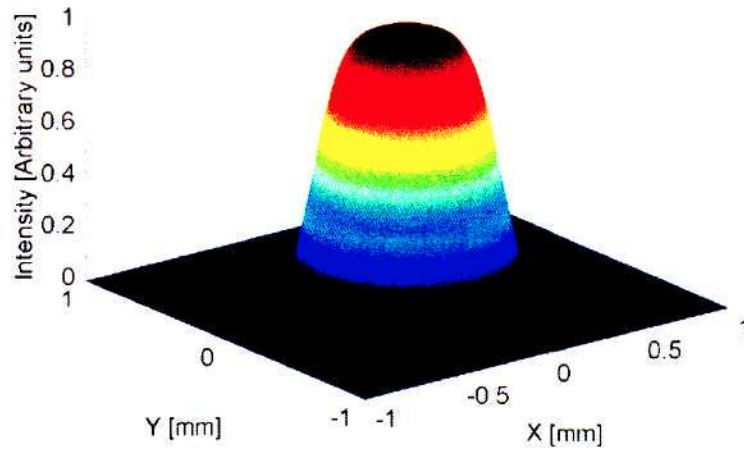


(a) Both super-Gaussian coefficients = 5.

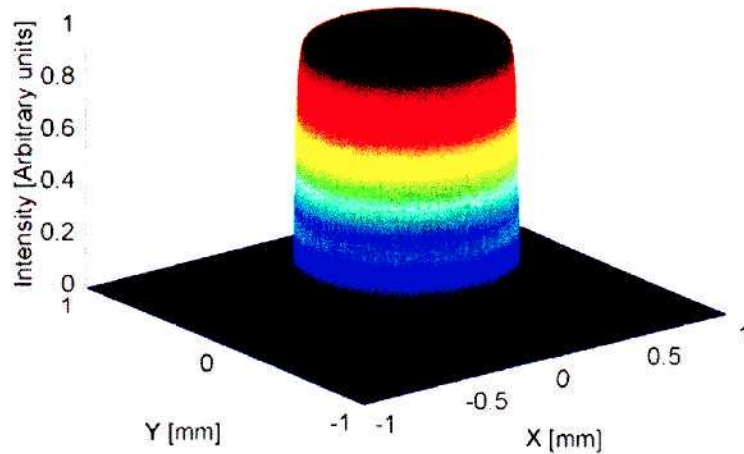


(b) Both super-Gaussian coefficients = 50.

Figure 2.3: The transverse pump intensity profiles for various super-Gaussian coefficients with the beam radii 0.2 mm and 0.6 mm in the x and y directions respectively.



(a) Super-Gaussian coefficient = 5.



(b) Super-Gaussian coefficient = 50.

Figure 2.4: The circularly symmetric transverse pump intensity profiles for various super-Gaussian coefficients and beam radius of 0.5 mm.

This can be achieved without computing all the thermal and thermo-optical effects for different values of every parameter. Another important advantage of analytical expressions is that they are very fast to calculate.

The analytical solutions of a continuous-wave (CW) end-pumped cylindrical laser rod with radius R and length L , is discussed in this section. The pump beam has a top-hat transverse intensity distribution with radius $w(z)$.

The heat diffusion equation (equation 2.10) can be written in cylindrical coordinates

$$k \left(\frac{1}{r} \frac{\partial}{\partial r} \left(r \frac{\partial T}{\partial r} \right) + \frac{1}{r^2} \frac{\partial^2 T}{\partial \Theta^2} + \frac{\partial^2 T}{\partial z^2} \right) + \tilde{q} = \rho c \frac{\partial T}{\partial t} \quad (2.18)$$

The following assumptions are made:

- The solutions are steady state so that the time dependence term is zero as in the case of continuous-wave pumping.
- There is no axial heat-flux (Chénais *et al.*, 2004)
- The pump profile is axisymmetric (Chénais *et al.*, 2004)
- The thermal conductivity is independent of temperature
- The material properties are independent of orientation (i.e. an isotropic material)
- The edge of the crystal ($r = R$) is kept at a constant temperature by making use of a heat sink ($T(R, z) = T_R$)

With these assumptions, equation 2.18 now reduces to the following time-independent expression

$$\frac{1}{r} \frac{\partial}{\partial r} \left(r \frac{\partial T}{\partial r} \right) + \frac{\partial^2 T}{\partial z^2} = \frac{-\tilde{q}}{k} \quad (2.19)$$

The heat load that is added to the laser rod via the pump beam is defined as

$$\tilde{q}(r, z) = \begin{cases} \frac{\alpha \eta P_p e^{-\alpha z}}{\pi w_p(z)^2}, & r \leq w_p(z) \\ 0, & r > w_p(z) \end{cases} \quad (2.20)$$

so that the solution of equation 2.19 is given by (Cousins, 1992) (Chénais *et al.*, 2004)

$$T(r, z) - T(R, z) = \frac{\alpha \eta P_p e^{-\alpha z}}{4\pi k} \times \begin{cases} -\ln \left(\frac{w_p(z)^2}{R^2} \right) + 1 - \frac{r^2}{w_p(z)^2}, & r \leq w_p(z) \\ -\ln \left(\frac{r^2}{R^2} \right), & r > w_p(z) \end{cases} \quad (2.21)$$

From this result it is clear that for a top-hat pump distribution, the temperature profile is parabolic within the pumped region while it is logarithmic outside the pumped region.

2.2.4 Numerical Solutions

In contrast to the simplistic assumptions in most analytical models, numerical models make it possible to investigate complex pump geometries, gain media and cooling techniques. The numerical model that was implemented in this research project was based on the finite element method (FEM). In this approach the partial differential equation that governs the problem (in this case the heat diffusion equation) is approximated by a system of ordinary differential equations, which can be solved by standard techniques such as Euler's method.

Euler's Method

Consider the two-dimensional time independent heat diffusion equation in cartesian coordinates

$$\frac{\partial^2 T(x, y)}{\partial x^2} + \frac{\partial^2 T(x, y)}{\partial y^2} = \frac{-\tilde{q}}{k} \quad (2.22)$$

Now define a grid of discrete nodes over the area where the function is defined (see Figure 2.5). Consider a particular node P in the grid along with its neighboring nodes N , E , S and W (see Figure 2.6).

The derivative of the dependent variable T at that specific node point P can be approximated by

$$\frac{\partial T}{\partial x} \approx \frac{T_e - T_w}{\Delta} \quad (2.23)$$

where Δ is the distance between consecutive nodes on the grid.

The second derivative at a node P can be approximated by

$$\begin{aligned} \frac{\partial^2 T}{\partial x^2} &= \left[\frac{\partial}{\partial x} \left(\frac{\partial T}{\partial x} \right) \right] \\ &\approx \frac{\left(\frac{\partial T}{\partial x} \right)_e - \left(\frac{\partial T}{\partial x} \right)_w}{\Delta} \\ &\approx \frac{1}{\Delta} \left[\frac{T_E - T_P}{\Delta} - \frac{T_P - T_W}{\Delta} \right] \\ &= \frac{1}{\Delta^2} (T_E + T_W - 2T_P) \end{aligned} \quad (2.24)$$

Similarly it can be shown that

$$\frac{\partial^2 T}{\partial y^2} \approx \frac{1}{\Delta^2} (T_N + T_S - 2T_P) \quad (2.25)$$

By applying these approximations, equation 2.22 can now be written as

$$T(x, y) \approx \frac{\tilde{q}\Delta^2}{4k} + \frac{1}{4} (T(x + \Delta, y) + T(x - \Delta, y) + T(x, y + \Delta) + T(x, y - \Delta)) \quad (2.26)$$

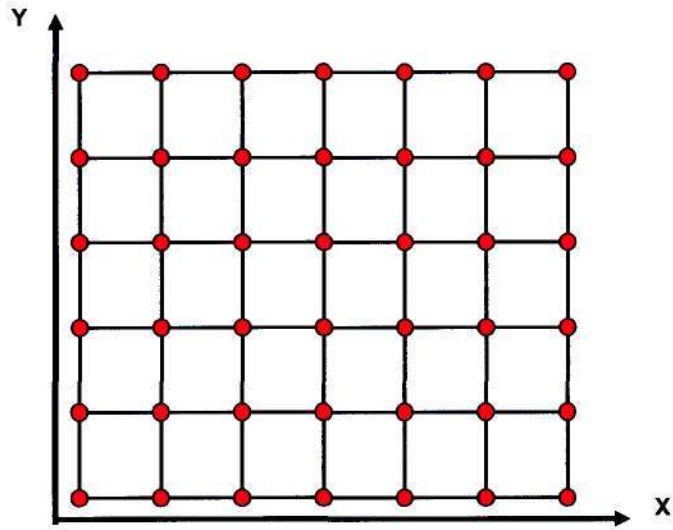


Figure 2.5: A grid that spans the area over which the differential equation will be solved.

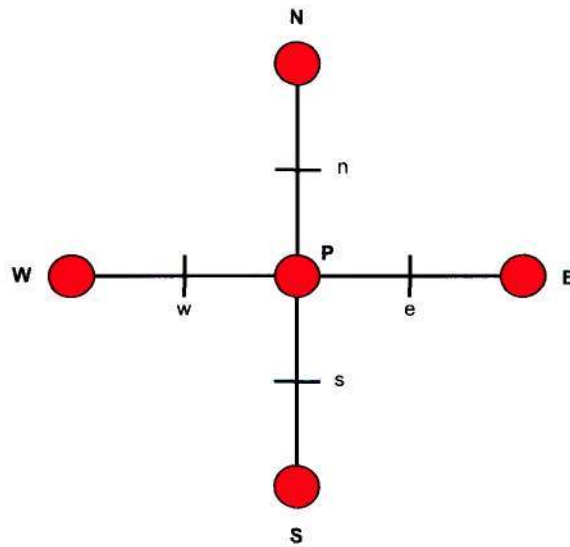


Figure 2.6: A specific node P with its neighboring nodes that illustrates Euler's method.

By iterating through the grid, the temperature at each node can be calculated which makes it possible to estimate the temperature distribution over the entire area with very good accuracy. To increase the accuracy of the results, it is usually sufficient to just decrease the distance (Δ) between nodes. Euler's method is one of the most basic and robust numerical techniques to solve differential equations.

Boundary Conditions

For the nodes that are on the edge of the grid (Figure 2.5), boundary conditions should be implemented. In this work, both Dirichlet and Neumann boundary conditions will be considered.

For a node point that is subject to a Dirichlet boundary condition, the value of the the solution (in this case the temperature) is specified at that particular node.

In the case of a Neumann boundary condition, the derivative of the solution is specified for the nodes that exist on the edge of the finite element grid. In this particular application it will imply that the temperature gradient, instead of just a constant temperature value, is specified for the surface of the crystal.

The most realistic boundary condition to describe the interface between the crystal and the copper heat sink is a Neumann boundary condition. It is implemented according to Newton's law of cooling where the temperature gradient on the edge of the crystal is defined as (Chénais *et al.*, 2004)

$$\left. \frac{\partial T}{\partial r} \right|_{r=R} = \frac{H}{-k}(T_{edge} - T_{sink}) \quad (2.27)$$

where H is the heat transfer coefficient which describes the quality of the contact between the gain medium and the copper heat sink, k is the thermal conductivity of the laser gain material while T_{edge} and T_{sink} denote the temperature of the edge of the gain medium and the heat sink respectively.

This more realistic boundary condition will result in an accurate absolute temperature distribution throughout the gain medium. However, it is important to note that the temperature gradient in the gain medium is independent of the surface temperature of the gain medium (Koechner, 1996).

Finite Element Analysis with MATLAB and ABAQUS

In this work, two commercial software packages were used to perform the finite element analysis.

MATLAB's partial differential equation toolbox was used to calculate the steady state temperature distribution in isotropic laser rods such as Nd:YAG. Since there exist analytical solutions for the case of isotropic rods, the MATLAB implementation of the FEM was merely used as quick verification of the analytical results.

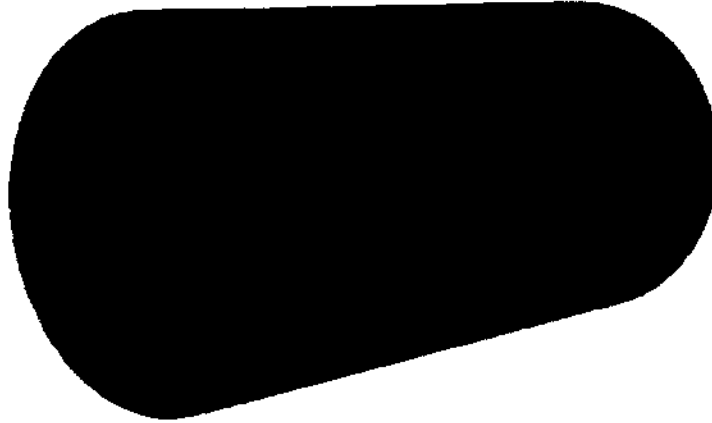


Figure 2.7: An example of the three-dimensional finite element discretization of a laser rod that is implemented in ABAQUS.

For anisotropic crystals where the material properties are different for the various axes, a more sophisticated commercial software package, ABAQUS, was used. With ABAQUS it is possible to perform a three-dimensional time dependent coupled thermal-stress analysis of the laser rod in order to determine the thermally induced stresses as a function of time. See Figure 2.7 for an example of the three-dimensional finite element discretization that is implemented in ABAQUS.

2.2.5 Comparison between Analytical and Numerical Solutions

Now that the analytical and numerical solutions of the heat diffusion equation have been discussed, they will be compared for the specific case where an isotropic cylindrical crystal is end-pumped by a CW top-hat beam. The input parameters in Table 2.1 were used for the calculations.

The analytical temperature distribution (from equation 2.21) in the laser rod can be seen in Figure 2.8. Note that it is not the absolute temperature that is given but the temperature difference with respect to the crystal edge. The maximum temperature difference of 72°C is located on the pump face in the center of the pump beam.

Since there is an exponential decay of the pump power inside the laser rod (equation 2.20), the pump face is the region of most interest. For this reason, the analytical

CHAPTER 2. END-PUMPED SOLID-STATE LASER THERMAL MODEL

Table 2.1: Input parameters that were used for the calculation of the temperature in the Nd:YAG.

Active ion	Nd
Crystal host	YAG
Doping at.%	1
Thermal conductivity [$\text{W}\cdot\text{m}^{-1}\cdot\text{K}^{-1}$]	13
Absorption coefficient @ 808 nm [cm^{-1}]	9.1
Fractional heat load	0.25
Fraction of pump power that is absorbed	0.935
dn/dT [K^{-1}]	9.86×10^{-6}
Incident pump power [W]	10
Pump beam radius [μm]	125
Crystal radius [mm]	1
Crystal length [mm]	3

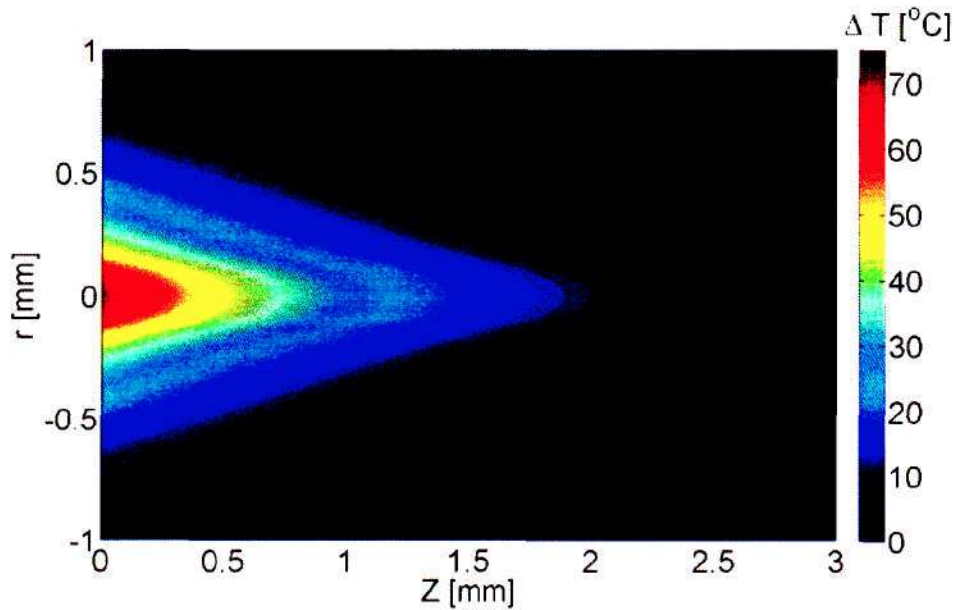


Figure 2.8: The analytical temperature distribution in the Nd:YAG rod which is pumped from the left by a 10 W top-hat beam with a radius of $125 \mu\text{m}$.

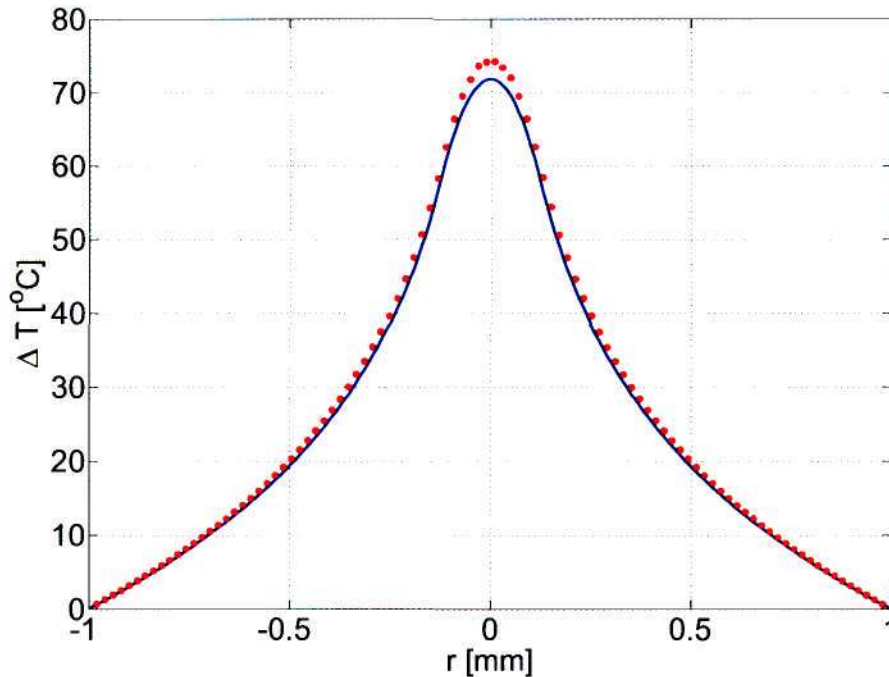


Figure 2.9: The analytical (blue line) and numerical (red dots) temperature distributions on the pump face of the Nd:YAG rod pumped by a 10 W top-hat beam with a radius of $125 \mu\text{m}$.

temperature profile on the pump face is compared to numerical results as produced by a FEM implementation in MATLAB. The temperature distribution comparison of the pump face can be seen in Figure 2.9. The maximum temperature difference of 74.65°C on the pump face, as produced by the numerical calculations, compares very well with the analytical solution. Not only is the maximum temperature of the two models in very good agreement, but also the respective profiles of the temperature distribution throughout both the pumped and unpumped regions are in very good agreement. As expected, the temperature profile is parabolic within the pumped region, while it decreases logarithmically in the unpumped region.

Note that in this implementation the boundary conditions were specified to be Dirichlet where the crystal edge was set to zero.

The comparison between analytical and numerical solutions is merely a check for consistency. The approach from here on is to use the analytical equations to calculate the temperature distribution for isotropic cylindrical crystals that are end-pumped by a CW top-hat beam. For more complex pump configurations and anisotropic laser

materials, a full FEM is implemented in ABAQUS.

The calculation of the temperature distribution inside the laser gain medium is the first step to ultimately determine the influence that thermal effects might have on the laser's performance.

2.3 Thermal Effects

In the previous section, the calculation of the temperature gradient in a laser rod was investigated. Consequences of the temperature gradient in the gain medium include laser beam distortion due to thermal lensing, depolarization loss due to stress induced birefringence and ultimately fracture of the laser rod (Clarkson, 2001). Of these thermal effects, thermal lensing and crystal fracture will be discussed in particular.

To illustrate the influence of thermal effects, the following discussion is restricted to edge-cooled isotropic cylindrical rods (see Figure 2.10).



Figure 2.10: A fractured Nd:YLF cylindrical crystal rod that is mounted in a copper heat sink.

2.3.1 Thermal Lensing

The refractive index profile in the laser gain medium acts on the laser beam as an arbitrarily shaped lens, which is generally referred to as a thermal lens. The thermal lens forms inside the laser gain medium due to a combination of the following effects:

- The inhomogeneous temperature distribution in a pumped laser rod induces a gradient in the refractive index of the medium due to the refractive index that has a temperature dependence.
- The temperature gradient leads to strains and stresses in the gain medium. The thermally induced strains cause a change in the refractive index (Pfstner *et al.*, 1994)(Weber *et al.*, 1999).
- The end-face of the laser rod forms a bulge due to thermally induced displacements in the rod. The bulge also contributes to the total thermal lens.

In the design of most laser resonators, the thermal lens can be accounted for by adding a thin lens to the resonator stability calculations.

For Nd:YAG laser rods in particular, the strain-induced refractive index changes are small in comparison to the contribution from the temperature gradient (Weber *et al.*, 1999). It is estimated that the temperature dependence of the refractive index of the rod contributes to more than 80% of the thermal lens in Nd:YAG lasers (Clarkson, 2001). In the rest of this discussion the strain- and displacement-induced refractive index changes will be ignored.

The temperature dependence of the refractive index in the rod induces a thermal lens of which the focal length (f_{th}) is given by

$$\frac{1}{f_{th}} = -\frac{\partial n}{\partial T} \int_0^L \left(\frac{\partial^2 T}{\partial r^2} \Big|_{r=0} \right) dz \quad (2.28)$$

where $\frac{\partial n}{\partial T}$ is the temperature dependence of the refractive index of the material and L the length of the rod in the pump light propagation direction.

Consider a cylindrical laser rod which is subjected to a top-hat pump beam so that the temperature distribution can be described by equation 2.21. Under all the assumptions for which equation 2.21 is valid, the focal length of the thermal lens is given by

$$\frac{1}{f_{th}} = \frac{\partial n}{\partial T} \frac{2\eta\gamma P}{4\pi k w^2} \quad (2.29)$$

where η is the fraction of absorbed pump power that is converted into heat and γ is the fraction of incident pump power (P) that is absorbed in the length (L) of the rod. The thermal conductivity of the material is denoted by k while w is the pump beam radius.

2.3.2 Thermally Induced Stresses

Aside from the optical influence that the pump-induced temperature gradient in the laser rod has on the laser, it also has an influence on the mechanical properties of the material (Weber *et al.*, 1999). Stresses inside the laser rod are induced due to the hotter inner region of the rod that is restricted from expansion by the cooler outer region (Pfister *et al.*, 1994). If the induced stresses in the laser rod exceed the tensile strength of the material, the rod will fracture and cause the pump and laser beams to be heavily distorted. The severe distortion losses might even cause the laser to no longer operate. Crystal fracture is one of the primary limiting factors in the power-scaling of diode-end-pumped solid-state lasers which makes it an important effect that has to be considered in the design process.

For isotropic materials such as Nd:YAG, which are subjected to a top-hat pump which is collimated in the crystal, it is possible to solve the stress distribution with analytical equations (Cousins, 1992) (Yan & Lee, 1994) if a plane stress approximation is made. This approximation assumes a thin disk that is only loaded in its own xy -plane and has no stresses in the z -direction.

For a cylindrical rod that is pumped by a CW top-hat beam which induces a temperature distribution in the rod as described in equation 2.21, the thermally induced radial (σ_r) and tangential (σ_θ) stresses on the pump face are given by (Yan & Lee, 1994)

$$\sigma_r(r) = \left(\frac{\alpha_T E \alpha \eta P_p}{4\pi k(1-\nu)} \right) \times \begin{cases} \ln\left(\frac{w_p}{R}\right) + \frac{1}{4} \left(\frac{r^2}{w_p^2} \right) - \frac{1}{4} \left(\frac{w_p^2}{R^2} \right), & r \leq w_p \\ \ln\left(\frac{r}{R}\right) + \frac{1}{4} \left(\frac{w_p^2}{r^2} \right) - \frac{1}{4} \left(\frac{w_p^2}{R^2} \right), & r > w_p \end{cases} \quad (2.30)$$

$$\sigma_\theta(r) = \left(\frac{\alpha_T E \alpha \eta P_p}{4\pi k(1-\nu)} \right) \times \begin{cases} \ln\left(\frac{w_p}{R}\right) + \frac{3}{4} \left(\frac{r^2}{w_p^2} \right) - \frac{1}{4} \left(\frac{w_p^2}{R^2} \right), & r \leq w_p \\ 1 + \ln\left(\frac{r}{R}\right) - \frac{1}{4} \left(\frac{w_p^2}{r^2} \right) - \frac{1}{4} \left(\frac{w_p^2}{R^2} \right), & r > w_p \end{cases} \quad (2.31)$$

where η is the fraction of incident pump power (P_p) that is converted into heat, E is Young's modulus, ν is Poisson's ratio, k the thermal conductivity, α the absorption coefficient and α_T is the linear expansion coefficient of the material.

For the general three-dimensional case, the failure criterion that is considered is the Tresca stress, also known as the stress intensity, which is defined as

$$\sigma_T = \max(|\sigma_1 - \sigma_2|, |\sigma_2 - \sigma_3|, |\sigma_3 - \sigma_1|) \quad (2.32)$$

where σ_1, σ_2 and σ_3 are the principal stresses.

With the plane stress approximation in the cylindrical isotropic rod, the Tresca failure criterion is merely the absolute value of the difference between σ_r and σ_θ .

It is generally accepted that the core of the rod is under compression (negative values of σ_r and σ_θ) while the outer part is in tension (positive values of σ_r and σ_θ). Since most laser gain medium materials are much stronger in compression than in tension, fracture will occur when the maximum tensile stress in the rod exceeds the tensile strength of the material (Cousins, 1992)(Yan & Lee, 1994)(Chénais *et al.*, 2004). From equations 2.30 and 2.31 it follows that the maximum tensile stress occurs on the surface of the rod.

The maximum stress in the rod can be calculated by substituting $r = R$ into equation 2.31 so that

$$\sigma_{max} = \left(\frac{\alpha_T E \alpha \eta P_p}{4\pi k(1-\nu)} \right) \left(1 - \frac{w_p^2}{2R^2} \right) \quad (2.33)$$

where w_p is the pump radius.

Note that the equation for the maximum tensile stress is written incorrectly in some literature. The maximum stress equation as it is written in (Yan & Lee, 1994) overestimates the maximum stress with a factor of two. In (Peng *et al.*, 2005), the entire $(1 - \nu)$ factor is missing in the equation. These errors have been corrected in the work presented here.

The maximum stress on the surface will tend to tear the material in the tangential direction and cause it to fracture along the radial direction (Yan & Lee, 1994).

If the material's fracture stress (σ_{frac}) is known, equation 2.33 can be used to estimate the critical incident pump power (P_c) at which fracture occurs

$$P_c = \left(\frac{4\pi k(1-\nu)\sigma_{frac}}{\eta\alpha\alpha_T E} \right) \left(\frac{1}{1 - \frac{w_p^2}{2R^2}} \right) \quad (2.34)$$

Although equation 2.34 gives a very good estimate of the critical incident pump power, the critical pump power is very strongly dependent on the surface roughness of the rod.

Note that equations 2.30-2.33 are only valid for isotropic rods. For anisotropic crystals such as YLF or YVO₄ where the material properties are not cylindrically symmetric, it is necessary to perform a three-dimensional FEM analysis in order to determine the stress distribution in the laser rod (Pfistner *et al.*, 1994). However, it is shown in Chapter 5 that the analytical stress model for isotropic rods can be used to estimate the stresses in anisotropic rods with reasonable accuracy.

The equations in this section outline the analytical model for the stress distribution in an isotropic laser rod. In the next chapter, these equations will be implemented in an end-pumped Nd:YAG laser model and the results will be discussed in detail.

Chapter 3

Continuous Wave Pumped Nd:YAG Rod

In the previous chapter, the basic theory that describes the temperature distribution inside an isotropic end-pumped cylindrical laser rod was derived. Both analytical and numerical temperature models were considered. The theory behind two of the main thermal effects that are induced by the temperature gradient in the laser rod, namely thermal lensing and thermally induced stresses, were also discussed.

In this chapter, the analytical and numerical models that have been discussed in the previous chapter are applied to an end-pumped Nd:YAG cylindrical rod laser model in order to investigate the temperature distribution and the induced thermal effects.

Note that the main assumptions in the laser model include the following

- The laser rod is isotropic
- The laser rod is cylindrically symmetric
- The material properties are independent of temperature
- The heat flux in the axial direction is neglected
- The pump beam is axisymmetric
- Beer-Lambert absorption of the pump light in the laser rod
- The pump beam in the crystal is perfectly collimated
- The pump is continuous wave (steady-state)
- A constant fraction of absorbed pump light is converted into heat

Table 3.1: Input parameters for the calculation of thermal effects in this chapter.

Parameter	Value	Reference
Active ion	Nd	
Crystal host	YAG	
Doping at. %	1	
Thermal conductivity [$\text{W}\cdot\text{m}^{-1}\cdot\text{K}^{-1}$]	12.9	(VLOC YAG Brochure, 2008)
Absorption coefficient @ 808 nm [cm^{-1}]	4.7	(Didierjean <i>et al.</i> , 2003)
Fractional heat load	0.27	(Didierjean <i>et al.</i> , 2003)
Fraction of pump power that is absorbed	0.85	
Refractive index	1.81	(VLOC YAG Brochure, 2008)
dn/dT [K^{-1}]	8.9×10^{-6}	(VLOC YAG Brochure, 2008)
Incident pump power [W]	8.5	(Didierjean <i>et al.</i> , 2003)
Pump beam radius [μm]	650	(Didierjean <i>et al.</i> , 2003)
Crystal radius [mm]	1	(Didierjean <i>et al.</i> , 2003)
Crystal length [mm]	4	(Didierjean <i>et al.</i> , 2003)
Linear expansion coefficient [K^{-1}]	7.9×10^{-6}	(VLOC YAG Brochure, 2008)
Young's modulus [GPa]	282	(VLOC YAG Brochure, 2008)
Poisson's ratio	0.28	(VLOC YAG Brochure, 2008)

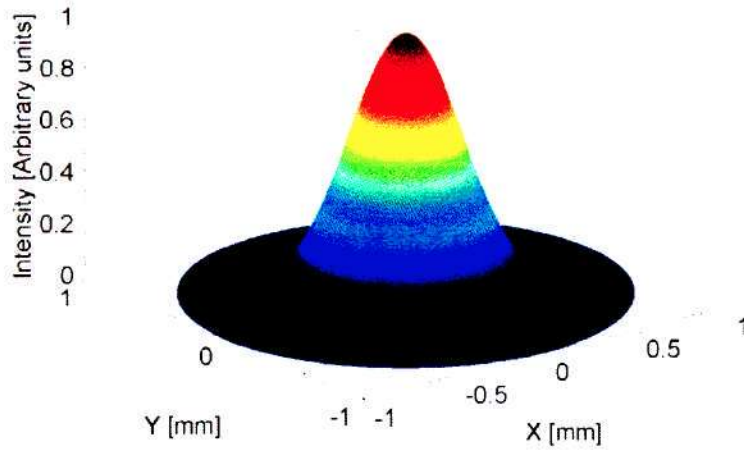
The parameters that are used in the theoretical calculations of this model are listed in Table 3.1. A normal Gaussian pump beam profile as well as a top-hat pump beam profile are implemented. The transverse pump beam intensity profiles that were used in this model can be seen in Figures 3.1(a) & 3.1(b). The temperature distribution, thermal lens and thermally induced stresses that are induced by each of the two pump profiles are calculated and compared.

3.1 Temperature Distribution

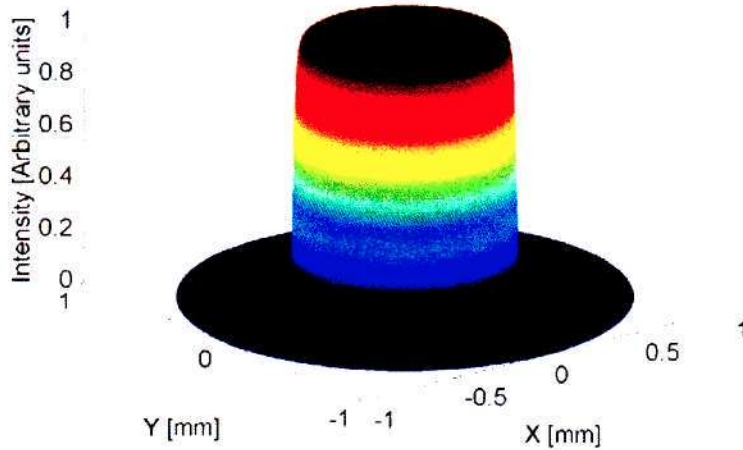
The temperature distribution in the laser rod was calculated for a Gaussian pump beam and a top-hat pump beam. In both cases the results were compared to the measured temperature profile in a crystal that is pumped by a Gaussian beam.

For the top-hat pump beam, the analytical (equation 2.21) and the numerical (based on equation 2.26) temperature profiles on the pump face were compared to experimental data taken from (Didierjean *et al.*, 2003) (see Figure 3.2).

The numerical distribution in the crystal was calculated with MATLAB's partial differential equation toolbox. The surface temperature of the crystal was kept constant



(a) Pump beam with a Gaussian transverse intensity profile.



(b) Pump beam with a top-hat transverse intensity profile.

Figure 3.1: The transverse intensity profiles of the pump beams that are implemented in this chapter.

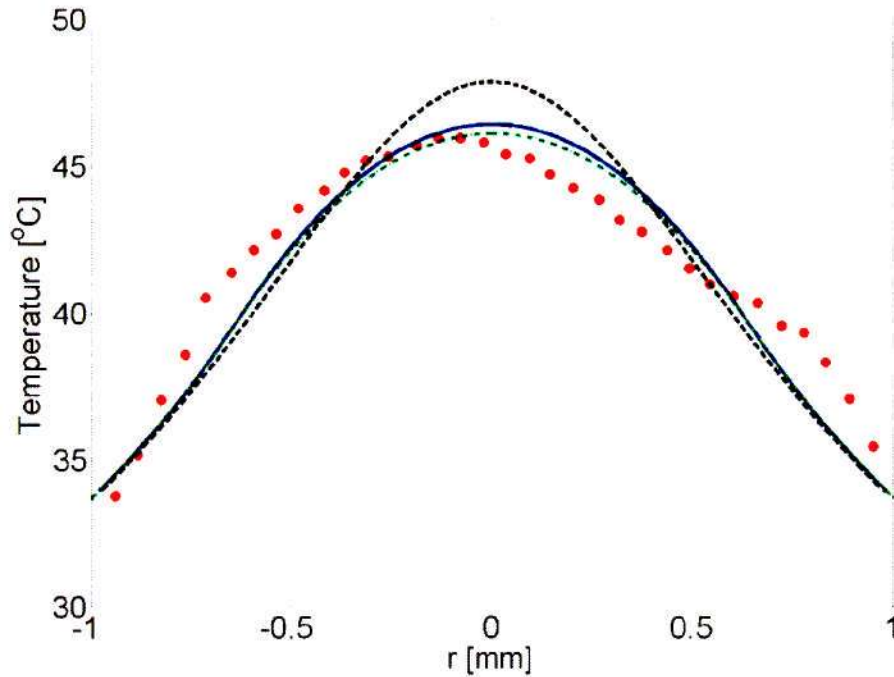


Figure 3.2: The calculated (solid blue line:analytical and dashed green line:numerical) temperature profiles on the pump face of the crystal while subject to a CW top-hat pump beam. The temperature profile due to a Gaussian pump beam is added as a comparison (black dashed line). In the case of the measured (red dots) temperature distribution (Didierjean *et al.*, 2003), the crystal was subject to a CW Gaussian pump beam.

(Dirichlet boundary condition). The theoretically calculated temperature profiles are in very good agreement with the measured temperature profile. The non-symmetric shape of the experimental data is due to a slight dissymmetry in the pump setup.

The analytical temperature distribution throughout the volume of the crystal is shown in Figure 3.3.

For the Gaussian pump beam, only the numerical temperature distribution (based on equation 2.26) was compared to the experimental data, since the analytical solution in equation 2.21 is only valid for a top-hat transverse intensity distribution (see Figure 3.2). The numerical implementation was the same as for the top-hat pump beam. The numerical model predicts the maximum temperature on the pump face to be 48°C which is two degrees higher than the measured value.

It is clear from Figure 3.2 that there is no significant change ($< 5\%$) in the temper-

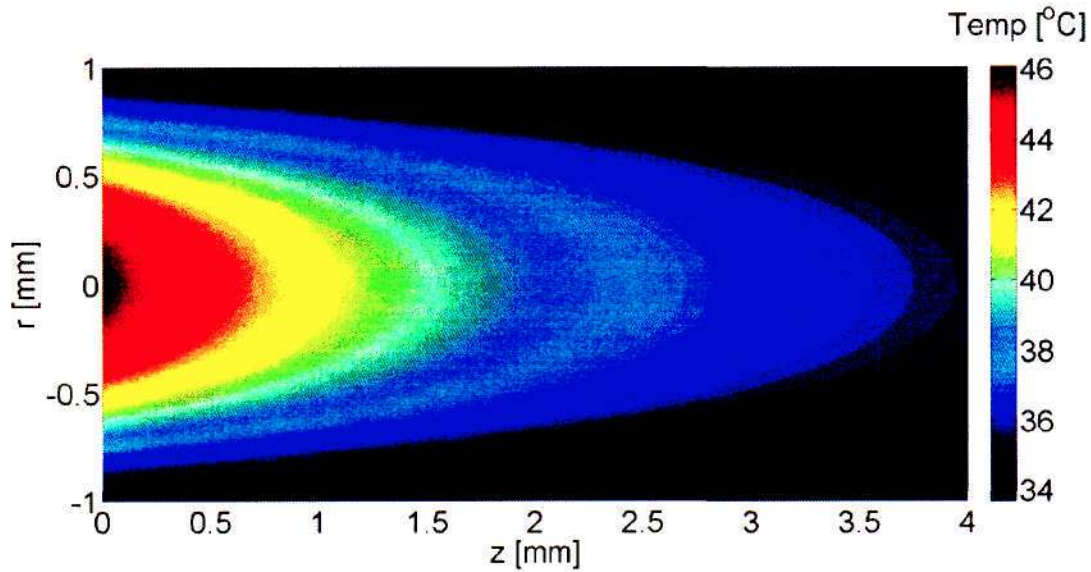


Figure 3.3: The analytical temperature distribution in the Nd:YAG laser rod which is pumped by a 8.5 W top-hat beam with a radius of $650 \mu\text{m}$.

ature distribution on the pump face when a Gaussian pump beam is used instead of a top-hat beam. (Didierjean *et al.*, 2003) describes the pump beam in their experiments as Gaussian, but contradicts the statement by saying the output face of the multi-mode fibre was imaged onto the crystal (this implies a top-hat pump beam). Even though the difference between the temperature profiles are small, it is peculiar that the temperature profile from the top-hat pump beam provides a better fit to the experimental data. It is not clear whether the experimental data was from a top-hat or a Gaussian pump beam.

Note that the experimental data which the models are compared to is the measured temperature distribution across the centre of a square pump face ($2 \times 2 \text{ mm}$) while the theoretical calculations are for a circular ($R = 1 \text{ mm}$) pump face. Even though the pump faces aren't the same shape, the experimental data is added merely to show that the calculated temperature distribution is very close to reality. As long as the area and circumference of the pump faces are roughly the same, the shape of the pump face shouldn't affect the temperature distribution too much in the case of a CW (steady-state) pump.

3.2 Thermal Lensing

In this section, only the temperature dependence of the refractive index is considered to contribute to the thermal lens. This is a very good assumption since the contribution of the “bulging-effect” and thermally induced strains only accounts for $\sim 20\%$ of the thermal lens in Nd:YAG lasers (Clarkson, 2001).

In order to design a laser resonator that is stable under low as well as high power operation, it is very useful to determine the dependence of the thermal lens focal length on the incident pump power. The analytical expression for the thermal lens focal length (equation 2.29) makes it very easy to investigate how various pump parameters such as the incident power and beam radius influence the induced thermal lens. It is clear from equation 2.29 that the thermal lens optical power (inverse of the focal length) is linearly dependent on the incident pump power while the thermal lens focal length is proportional to the inverse of the incident pump power (Figure 3.4). For an incident top-hat pump beam of 8.5 W (radius 650 μm), the thermal lens focal length is ~ 2 m. As the pump power goes to zero, the thermal lens optical power goes to zero, which implies that there is no thermal lens at all. The maximum anticipated incident pump power should be used to get an estimate of the maximum strength of the thermal lens. If the pump power is increased from 8.5 W to 200 W, a much stronger thermal lens with a focal length of 84 mm is induced.

From equation 2.29 it follows that the thermal lens focal length is proportional to the square of the pump beam radius (see Figure 3.5). In order to reduce the strength of the thermal lens, a larger pump beam size should be implemented. In reality, by changing the pump beam radius, many other important aspects of the laser’s operation are influenced, such as the laser threshold. These effects are discussed in later chapters.

It follows from equation 2.28 that even though the temperature profiles in the laser rod due to the respective top-hat and Gaussian pump beams are almost the same, the thermal lens induced by the Gaussian beam is expected to be stronger than that of the top-hat pump beam since the temperature profile in the case of the Gaussian beam has a stronger curvature at $r = 0$ (see Figure 3.2). It is estimated in some literature that the Gaussian pump beam can induce a thermal lens that is up to twice as strong as that of the top-hat pump beam (Clarkson, 2001). The Gaussian beam will also induce a more highly aberrated thermal lens (Clarkson, 2001). The degradation of the laser beam will thus be worse for a Gaussian pump beam. In order to reduce the degradation of the laser beam it must be chosen to be smaller than the pump beam radius so that the laser beam only occupies the central region of the pumped region where the aberrations are smaller (Clarkson, 2001).

For CW lasers it is usually easy to compensate for the thermal lens in the design of the resonator, while in quasi-continuous wave pumped lasers the thermal lens changes drastically during a single QCW-pulse, which makes it extremely difficult to design a resonator which is stable for such a variable thermal lens.

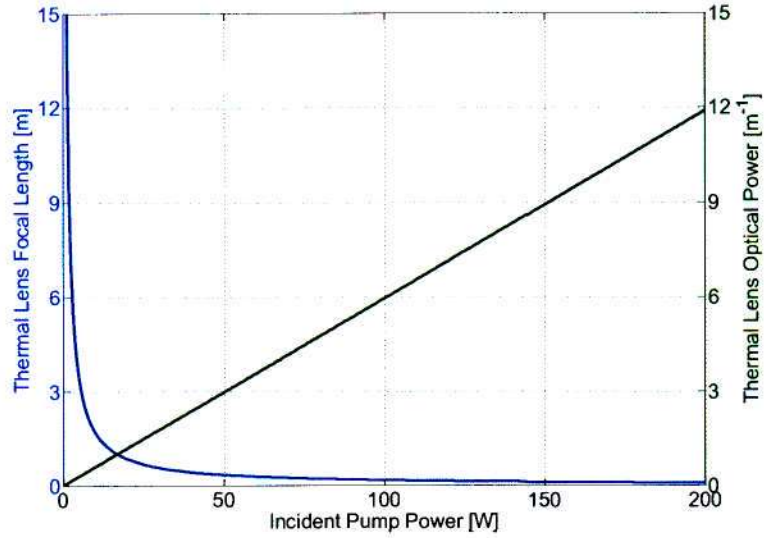


Figure 3.4: The variation of the thermal lens focal length (blue) and optical power (green) with incident pump power (top-hat pump beam) and pump beam radius $650 \mu m$.

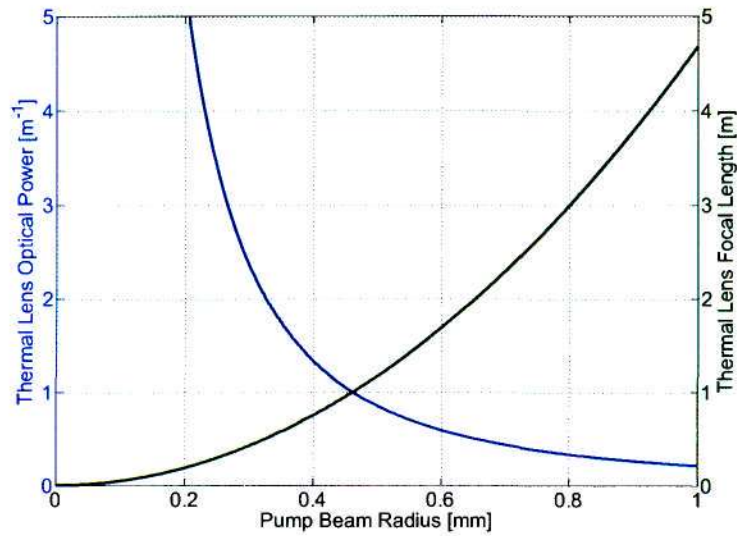


Figure 3.5: The thermal lens focal length (green) and optical power (blue) as a function of pump beam radius. The top-hat pump beam has an incident power of 8.5 W.

3.3 Thermally Induced Stresses

The most important influence that the temperature gradient inside the laser rod has on the mechanical properties of the material, is the stresses that are induced. When the induced stresses in the laser rod exceed the tensile strength of the material the rod will fracture and the laser will no longer operate. For this reason it is important to operate the laser so that the thermally induced stresses are well below the tensile strength of the material.

By making use of the analytical equations 2.30 & 2.31, the stresses on the pump face of the Nd:YAG rod can be determined (see Figure 3.6). As expected, the centre of the rod is under compression while the outer regions are in tension.

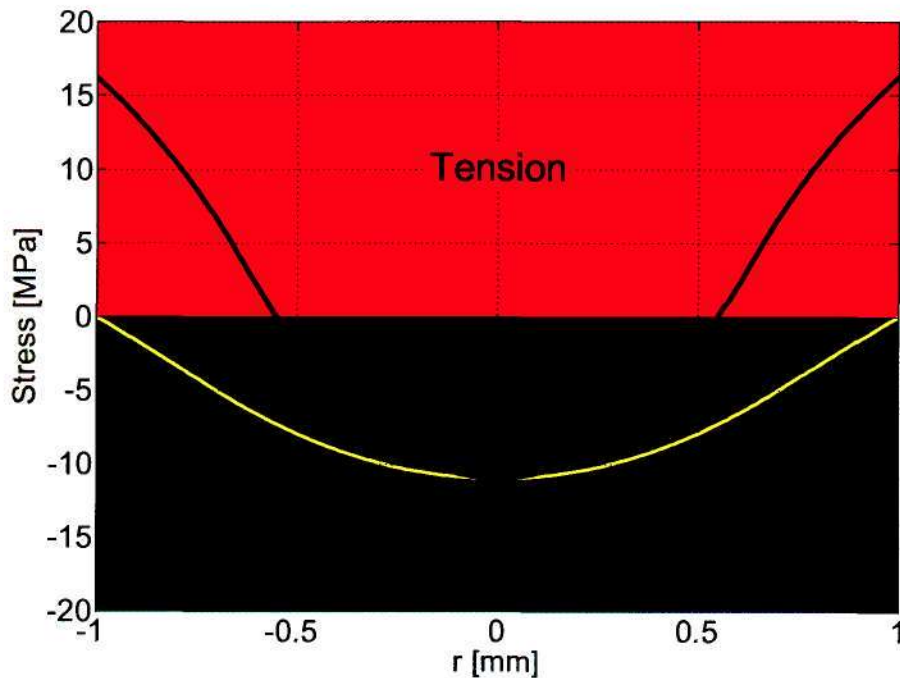


Figure 3.6: The radial (yellow line) and tangential (blue line) stresses on the pump face of the Nd:YAG rod with an 8.5 W incident top-hat pump beam. The green and red regions indicate compression and tension respectively.

With an 8.5 W incident top-hat pump beam, the maximum tensile stress of 16 MPa is found on the edge of the crystal. This value is well below the tensile strength of YAG which is 280 MPa (VLOC YAG Brochure, 2008). The maximum stress in the

laser rod has also been calculated numerically with ABAQUS and found to be within 5% of the analytical value.

The stress intensity distribution in the laser rod while it is pumped by a Gaussian beam has also been investigated numerically and the maximum tensile stress was found to be within 1% of the maximum tensile stress induced by a top-hat pump-beam of the same power.

Now that the stresses have been calculated analytically and verified numerically for an 8.5 W incident pump-beam, it is very important to determine how hard the YAG rod can be pumped before fracture will occur. This power limit can be calculated by making use of equation 2.34 and is referred to as the *critical incident pump power*. Once the critical incident pump power is known, the laser can be operated below this limit to ensure that the crystal will not fracture.

The critical incident pump power has been calculated analytically and numerically for the Nd:YAG crystal under lasing as well as non-lasing conditions. While the laser is not lasing, the fractional heat load (η) is taken as 0.4 (Fan, 1993) as opposed to the 0.27 (Didierjean *et al.*, 2003) under lasing conditions. Figure 3.7 shows the maximum stress intensity in the laser rod as a function of incident pump power. There is a very good agreement between analytical and numerical values for the maximum stress in the laser rod. When there is no laser beam to extract the pump energy from the rod, the critical incident pump power is ~ 100 W. When the laser is functional, the critical incident pump power increases to ~ 150 W since there is a laser beam that can extract energy from the laser rod so that less heat is generated. To prevent thermal fracture, the rod cannot be pumped with more than 150 W under lasing conditions.

A possible method that can be applied to increase the total power that can be deposited into the rod before fracture occurs, is to pump the rod from both sides. Since the maximum tensile stress occurs on the pump face, there will be a very small contribution to the stresses on a particular rod face due to a pump beam that is pumping the opposite rod face. This will make it possible to deposit almost twice as much power inside the rod before fracture will occur.

It is clear from equation 2.34 that the the ratio of the rod radius to the pump beam radius is very important in determining the critical incident pump power. By changing the pump beam radius, many other important aspects of the laser's operation will be influenced, such as the laser threshold. For this discussion, only the effect that the pump beam radius has on the critical incident pump power will be considered. Figure 3.8 shows the critical incident pump power as a function of pump beam radius. As an example, when the pump beam radius is increased from $650 \mu\text{m}$ to $800 \mu\text{m}$, the critical incident pump power will increase from 150 W to about 170 W. The numerical and analytical solutions agree very well for w_p/R larger than 0.5. For w_p/R smaller than 0.5, there is a deviation between the numerical and analytical solutions which increases as the the pump beam radius decreases. For $w_p \ll R$, the analytical solution suggests a constant critical pump power while the numerical solution shows a decrease in the

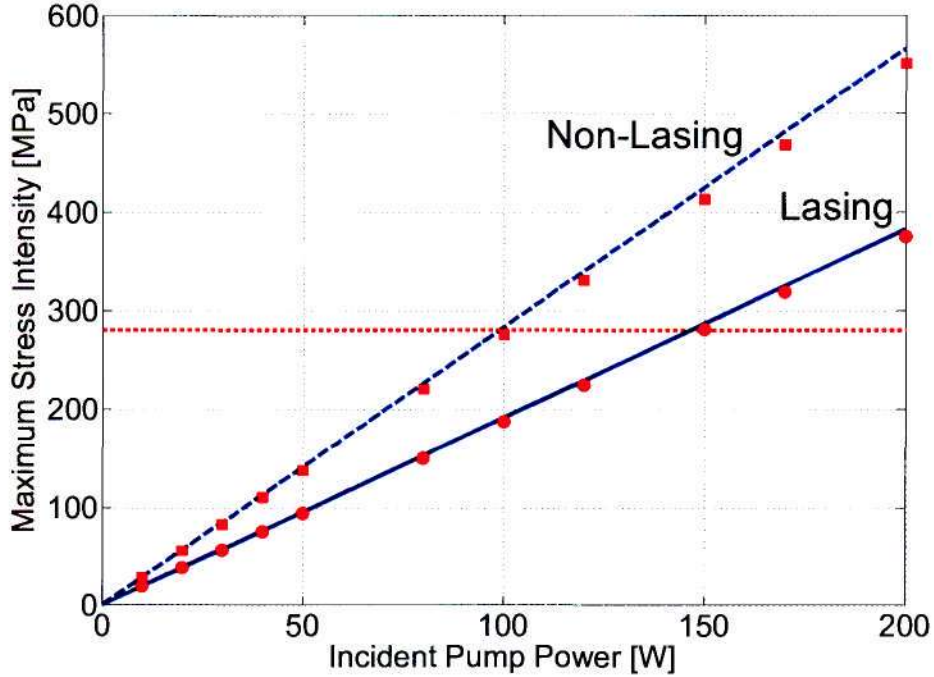


Figure 3.7: The analytical maximum stress intensity (blue lines) in the Nd:YAG laser rod under lasing and non-lasing conditions. In each case the analytical solution is compared to numerical results (red squares: non-lasing and red dots: lasing). The horizontal red line indicates the tensile strength of Nd:YAG.

critical pump power. If the critical pump power was independent of pump beam size for small pump beam radii the pump beam intensity would go to infinity as the pump beam radius goes to zero.

Figure 3.9 shows the pump beam radius dependence of the maximum stress in the laser rod for an incident pump power of 100 W. As before, there is good correspondence between the analytical and numerical values for the maximum stress only for w_p/R greater than 0.5. For $w_p \ll R$, the analytical solution suggests that the maximum stress is independent of the pump beam size while the numerical solution shows an increase in the maximum stress as the pump beam size decreases (increase in pump intensity).

The analytical solutions (equations 2.33 & 2.34) for the maximum stress and critical pump power of the laser rod are a very good approximation for w_p/R greater than 0.5.

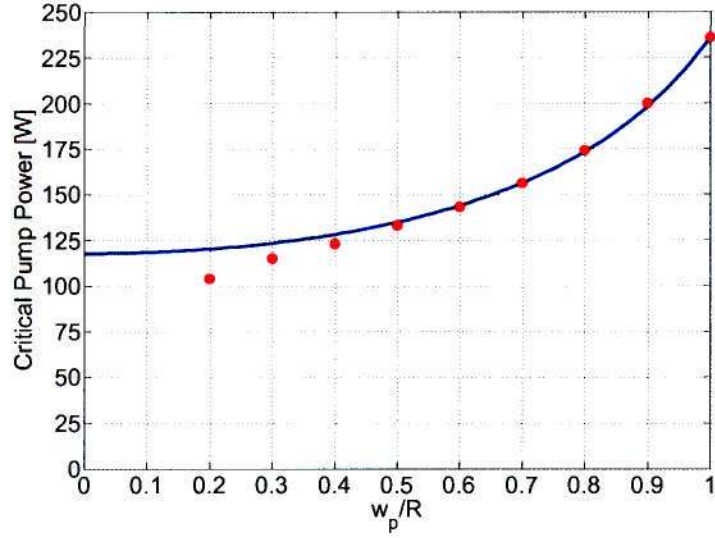


Figure 3.8: The critical incident pump power as a function of pump beam radius. (Blue line: analytical and red dots: numerical)

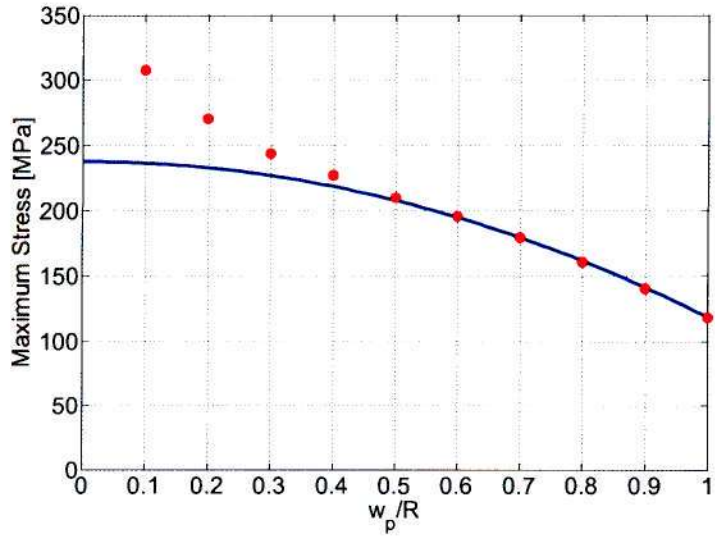


Figure 3.9: The maximum stress as a function of the pump beam radius for a 100 W incident pump beam. (Blue line: analytical and red dots: numerical)

3.4 Summary

The theory surrounding the thermal effects in solid-state lasers that have been discussed in the previous chapter were applied to a CW pumped Nd:YAG laser. The temperature distribution in the laser rod as well as the thermal lens and stresses that are induced due to the temperature gradient have been discussed for this particular laser. The considerations and suggestions in this chapter are purely based on the thermal effects. Pump beams with Gaussian and top-hat transverse intensity profiles were considered. As a verification of the results, analytical and numerical solutions were compared where possible.

The temperature gradient in the laser rod compared very well with experimental data. For a CW pumped laser, the transverse intensity profile of the pump beam seems to make no significant difference in the temperature gradient inside the laser rod.

The thermal lens in the laser rod and its dependence on the incident pump power and pump beam radius was investigated.

The analytical and numerical solutions for the maximum tensile stress in the laser rod are in very good agreement for w_p/R greater than 0.5. For this reason the use of the analytical solutions to determine the maximum stress and critical pump power should be restricted to larger pump beam radii where w_p/R is greater than 0.5. It is not clear why the analytical expression (equation 2.33) cannot accurately determine the maximum stress in the rod for $w_p/R < 0.5$ but it might be due to the maximum stress that occurs elsewhere in the rod and not on the pump face.

An incident pump power of 8.5 W induced a maximum tensile stress of 16 MPa which is well below the tensile strength of YAG. For the pump beam radius of 650 μm , the critical incident pump power is estimated to be 150 W. This power limit can somewhat be increased by using a larger pump beam.

The analysis in this chapter shows how a good thermal model can act as a design tool to address thermally induced effects in end-pumped solid-state lasers.

Chapter 4

Continuous Wave Pumped Nd:YAG Slabs

4.1 Analytical Equation for the Maximum Stress in an Anisotropic Slab

The theory that describes the analytical value of the maximum stress in laser gain media is restricted to cylindrical rods (see Section 2.3.2).

It is well known that the critical pump power at which fracture occurs (P_c) in a uniformly pumped slab, in comparison to a uniformly pumped rod, scales according to (Egglestone *et al.*, 1984)(Koechner, 1996)

$$\frac{P_c(\text{slab})}{P_c(\text{rod})} = \frac{3w}{2\pi t} \quad (4.1)$$

where w is the width in the x -direction and t the thickness in the y -direction of the slab (Figure 2.2).

Paschotta used finite element analysis to investigate the thermally induced stresses in a Yb:YAG slab (Paschotta *et al.*, 2000). He particularly examined the pump beam size dependence of the maximum stress in the slab. He found that the maximum stress is very weakly dependent on the pump beam diameter in the y -direction d_{py} . The maximum stress in the slab varied from 31% to 38% of the tensile strength of YAG when d_{py} was varied over the full thickness of the slab. On the other hand, Paschotta found that the maximum stress in the slab is very strongly dependent on the pump beam diameter in the x -direction d_{px} . He calculated a maximum stress variation of between 10% and 98% (of the tensile strength of YAG) when d_{px} was varied over the full width of the slab.

By ignoring the influence that the size of d_{py} has on the maximum stress in the laser slab and by assuming that the scaling of $P_c(\text{slab})$ for a non-uniformly pumped slab is

also according to equation 4.1, then the critical pump power of the slab is calculated by substituting equation 2.34 into equation 4.1 and by replacing the $(w_p/R)^2$ term in equation 2.34 by $(d_{px}/w)^2$ so that

$$P_c(\text{slab}) = \frac{6wk(1-\nu)\sigma_{frac}}{t\eta\alpha E\alpha_T \left(1 - \frac{d_{px}^2}{2w^2}\right)} \quad (4.2)$$

Equation 4.2 can now be used to investigate the influence that the aspect ratio (w/t) and d_{px} of the slab have on the critical pump power.

Throughout this chapter the same material properties as listed in Table 3.1 are used and the slabs are assumed to be mounted so that the top and bottom surfaces (xz -plane) are in contact with a heat sink.

4.2 Power Scaling of Slabs

One of the main reasons for using slabs instead of rods as gain media is the fact that they have a much higher critical pump power than rods. Exactly how much harder the slab can be pumped in comparison to a rod with the same material properties, depends very strongly on the aspect ratio of the slab as can be seen in equation 4.1.

For a slab with $w = 10$ mm and $t = 2$ mm (length=5 mm), the maximum stress in the slab as a function of incident pump power (with $d_{px} = 9.0$ mm) is shown in Figure 4.1.

For the Nd:YAG rod in the previous chapter, fracture occurred at an incident pump power of 150 W, while thermal fracture of the Nd:YAG slab will only occur at 475 W incident pump power. The power-scaling of the laser becomes easier when there is much more pump power available without damaging the slab. The analytical solution of the maximum stress in the slab is compared to numerical data that have been calculated with a finite element analysis in LASCAD and found to be in perfect agreement as can be seen in Figure 4.1.

4.3 The Influence of the Pump Beam Size on the Critical Pump Power and Maximum Stress

For the specific slab aspect ratio of 5 ($w = 10$ mm and $t = 2$ mm), the critical incident pump power as a function of d_{px} is investigated analytically (Figure 4.2). For d_{px}/w larger than 0.7, the analytical solution provides an accurate solution of the critical pump power. For the cylindrical YAG rod in the previous chapter, the analytical solution was accurate for w_p/R larger than 0.5. The discrepancy between the analytical solution and the numerical results at small pump beam radii is similar

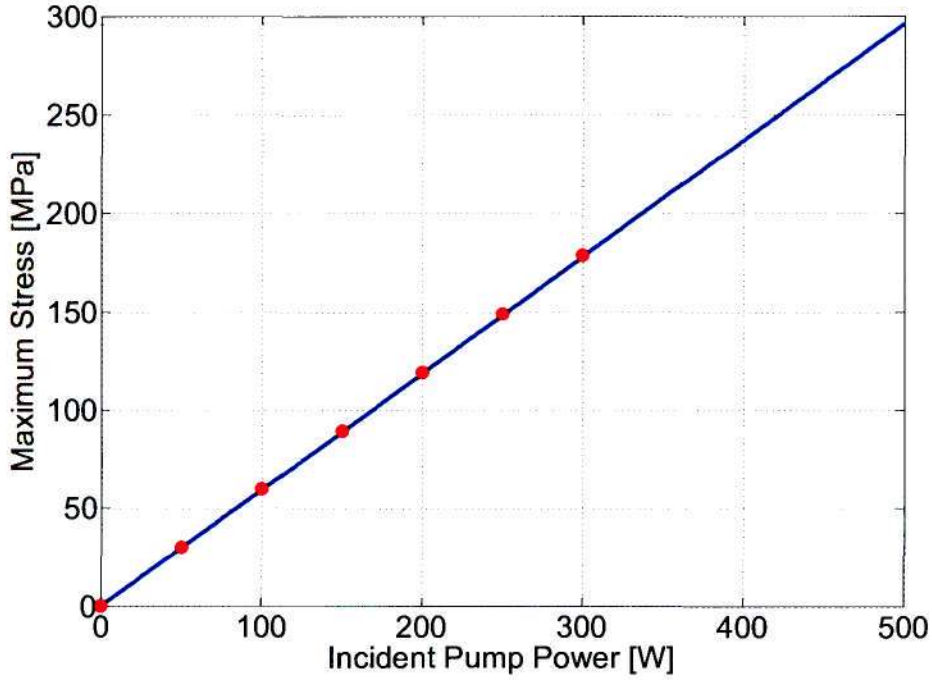


Figure 4.1: The maximum stress in the slab as a function of incident pump power (with $d_{px} = 9.0$ mm). (Blue line: analytical and red dots: numerical)

to the discrepancies that were found in the analysis of the stresses in a cylindrical rod in the previous chapter.

As a further validation, it is also necessary to investigate the variation of the maximum stress as a function of d_{px}/w . This is shown in Figure 4.3 for a CW incident pump power of 100 W. For d_{px}/w larger than 0.7, the analytical solution is consistent with numerical results, while it cannot provide an accurate answer for smaller pump beam radii.

At first glance, the the analytical model seems to be inadequate since it can only produce accurate answers for d_{px}/w larger than 0.7. Fortunately, most slab lasers operate in the region where d_{px}/w is in fact larger than 0.7, which makes equation 4.2 extremely useful in the determination of thermally induced stresses in isotropic slabs.

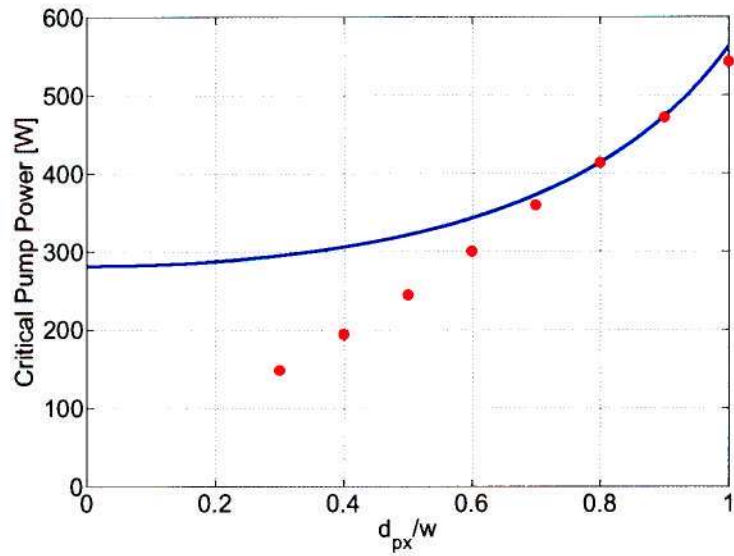


Figure 4.2: The critical incident pump power as a function of d_{px} . (Blue line: analytical and red dots: numerical)

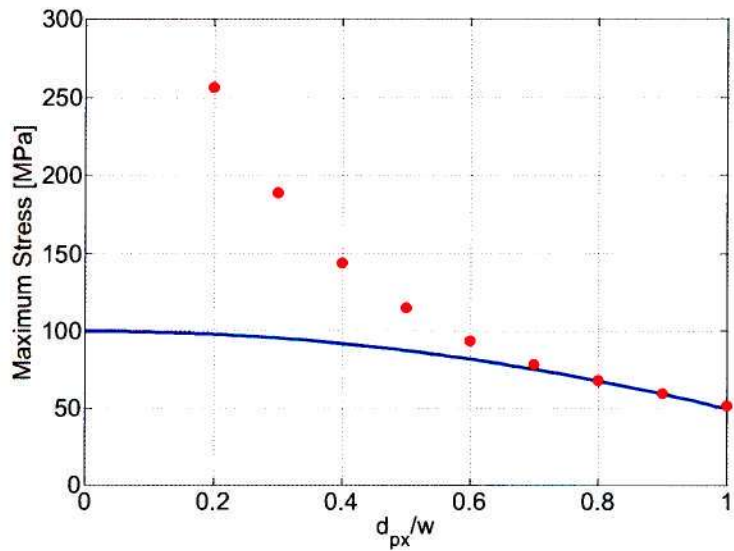


Figure 4.3: The variation of the maximum stress with d_{px}/w for a constant incident pump power of 100 W. (Blue line: analytical and red dots: numerical)

4.4 Aspect Ratio of the Slab

From equation 4.2, it is clear that the fracture limit of the slab can be increased by increasing the aspect ratio of the slab. By fixing the width of the slab at 10 mm and then varying the aspect ratio by changing the thickness of the slab, the critical pump power is determined as a function of aspect ratio (Figure 4.4). For a Nd:YAG slab with $w = 10$ mm and $t = 2$ mm, fracture will occur at an incident pump power of 475 W. This pump power limit can be increased to ~ 950 W with an aspect ratio of 10. The analytical critical pump power as a function of slab aspect ratio is within 10% accuracy of the numerical solution for aspect ratios between 4 and 10. The aspect ratio of the slab can't always be increased to the desired value since it is often limited by the current manufacturing techniques of the specific crystal (in this case YAG) and the propagation of the pump light through the slab.

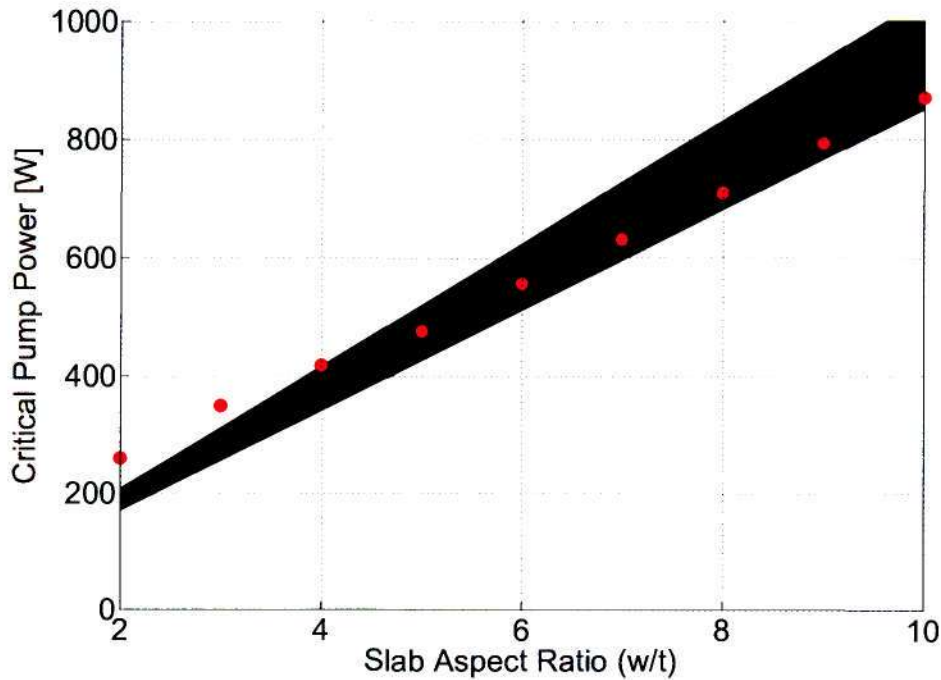


Figure 4.4: The critical pump power as a function of the aspect ratio of the slab. The green region indicates the analytical solution with a 10% error estimation. The red dots are numerical values.

4.5 Summary

In analogy to the analytical equation for the maximum tensile stress in a cylindrical rod, an analytical equation for the critical incident pump power of an isotropic slab has been derived by making use of the well known slab power scaling law (equation 4.1).

Equation 4.2 can be used to investigate the critical pump power as a function of d_{px} and slab aspect ratio.

The analytical equation that has been derived in this chapter is in good agreement with numerical results as long as d_{px}/w is larger than 0.7. Fortunately, for most slab lasers, d_{px}/w is in fact larger than 0.7, which makes equation 4.2 a quick and accurate way to investigate the critical pump power in an isotropic slab.

Even though equation 4.2 provides a robust way to estimate the maximum stress in a slab for large pump beam sizes, more work needs to be done in order to derive an expression for the maximum stress in a slab which is also valid for small pump beam sizes.

Chapter 5

Quasi-Continuous Wave Pumped Tm:YLF Rod

The power scaling of diode end-pumped solid-state lasers is a very active area of research. The main problem that limits the power scaling of these lasers is the generation of heat inside the laser gain medium which can ultimately cause fracture. When the continuous wave (CW) pump power exceeds the fracture power of the crystal, a quasi-continuous wave (QCW) pump is often used to reduce the average pump power to below the fracture pump power.

Due to the anisotropic nature of YLF, it is necessary to perform a three dimensional finite element analysis of the laser material in order to investigate the temporal and spatial behaviour of the thermally induced stresses (Pfistner *et al.*, 1994).

A time-dependent FEM model of a Tm:YLF laser rod has been implemented in ABAQUS. The boundary conditions at the interface between the rod and the copper heat sink were assumed to be Neumann boundary conditions (equation 2.27) with a heat transfer coefficient of $0.9 \text{ W.cm}^{-1}.\text{K}^{-1}$ (Didierjean *et al.*, 2003). Convection on the end-faces of the crystal are ignored in this study. To solve the heat equation numerically, the Tm:YLF rod has been discretized into 5560 finite elements.

For the steady-state CW pump case, the model is compared to experimental fracture data taken from (So *et al.*, 2006). Table 5.1 shows all the model input parameters that were used. For the CW pump case, fracture of the 4% doped Tm:YLF rod was reported at 38.7 W of absorbed pump power, which corresponds to 47.2 W of incident power (So *et al.*, 2006). The transverse intensity profile of the pump beam was assumed to be a super-Gaussian of order 10. This is also referred to as a quasi-top-hat beam and is a very good representation of a fibre-coupled diode pump.

At 47.2 W incident pump power, the maximum temperature in the YLF rod was calculated to be 128 °C, while the maximum stress intensity was calculated to be 40.75 MPa, which agrees very well with the 33-40 MPa tensile strength of YLF that is found in literature (Koechner, 1996) (Peng *et al.*, 2005). Throughout the rest of

Table 5.1: Input parameters that are used for the calculations in this chapter.

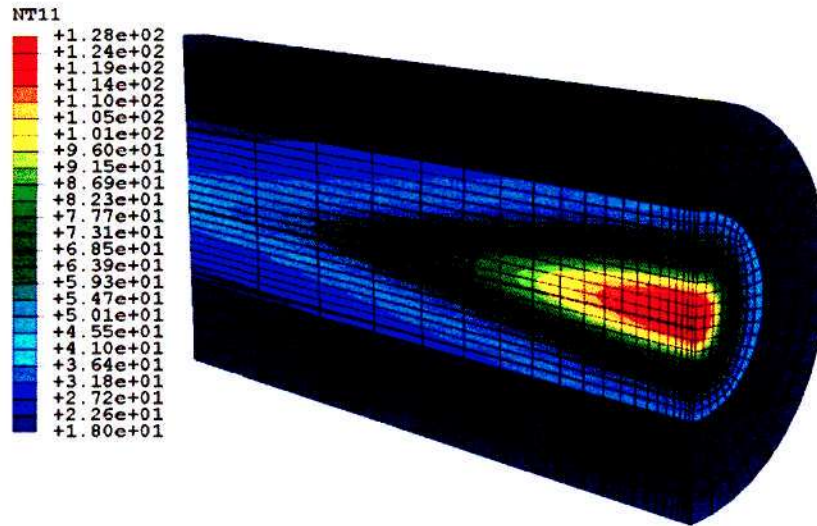
Parameter	Value	Reference
Active ion	Tm	
Crystal host	YLF	
Doping at. %	4	(So <i>et al.</i> , 2006)
Thermal conductivity a [W.m ⁻¹ .K ⁻¹]	7.2	(Pollak <i>et al.</i> , 1982)
Thermal conductivity c [W.m ⁻¹ .K ⁻¹]	5.8	(Pollak <i>et al.</i> , 1982)
Absorption coefficient @ 792 nm [cm ⁻¹]	1.43	(So <i>et al.</i> , 2006)
Fractional heat load	0.33	
Refractive index n _o	1.44	(Walsh, 1995)
Refractive index n _e	1.46	(Walsh, 1995)
Incident pump power [W]	47.18	(So <i>et al.</i> , 2006)
Pump beam radius [μm]	470	(So <i>et al.</i> , 2006)
Crystal radius [mm]	1.5	(So <i>et al.</i> , 2006)
Crystal length [mm]	12	(So <i>et al.</i> , 2006)
Linear expansion coefficient a [K ⁻¹]	13×10 ⁻⁶	(Pollnau <i>et al.</i> , 1998)
Linear expansion coefficient c [K ⁻¹]	8×10 ⁻⁶	(Pollnau <i>et al.</i> , 1998)
Young's modulus [GPa]	75	(Koechner, 1996)
Poisson's ratio	0.33	(Koechner, 1996)
Specific heat [J.kg ⁻¹ .K ⁻¹]	790	(Pollnau <i>et al.</i> , 1998)

this work 40MPa is considered to be the tensile strength of YLF. Figure 5.1 shows the temperature and stress distributions in the Tm:YLF rod at the CW critical incident pump power of 47.2 W. Even though the analytical equation 2.33 for the maximum stress is meant for an isotropic rod, it can be used to model the maximum stress in an anisotropic rod with great success if the material properties are taken to be the worst of the two axes (a- and c-axis) in the rod. Figure 5.2 shows the analytical values for the maximum stress as a function of incident pump power.

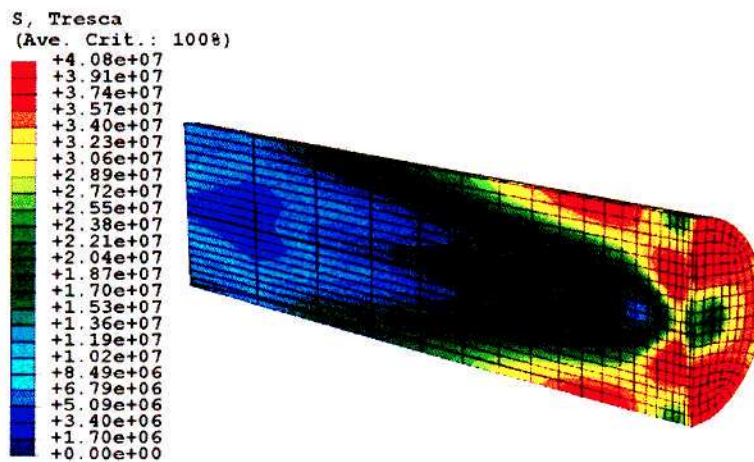
Since there is a very good agreement between the numerically calculated fracture of the YLF rod and experimental fracture data in the case of a CW pump, the model was extended to a time dependent analysis so that it can simulate a modulated or QCW pump.

5.1 Single-Pulse

The first step in the time dependent numerical stress model is to determine the thermally induced stresses during a single QCW pump pulse (see Figure 5.3).



(a) The temperature distribution throughout the Tm:YLF rod. The maximum temperature is 128 °C.



(b) The Tresca stress distribution throughout the Tm:YLF rod while subject to 47.2 W incident CW pump power. The maximum stress is 40.75 MPa.

Figure 5.1: The numerical temperature and Tresca stress distributions in the Tm:YLF rod while subject to 47.2 W incident pump power.

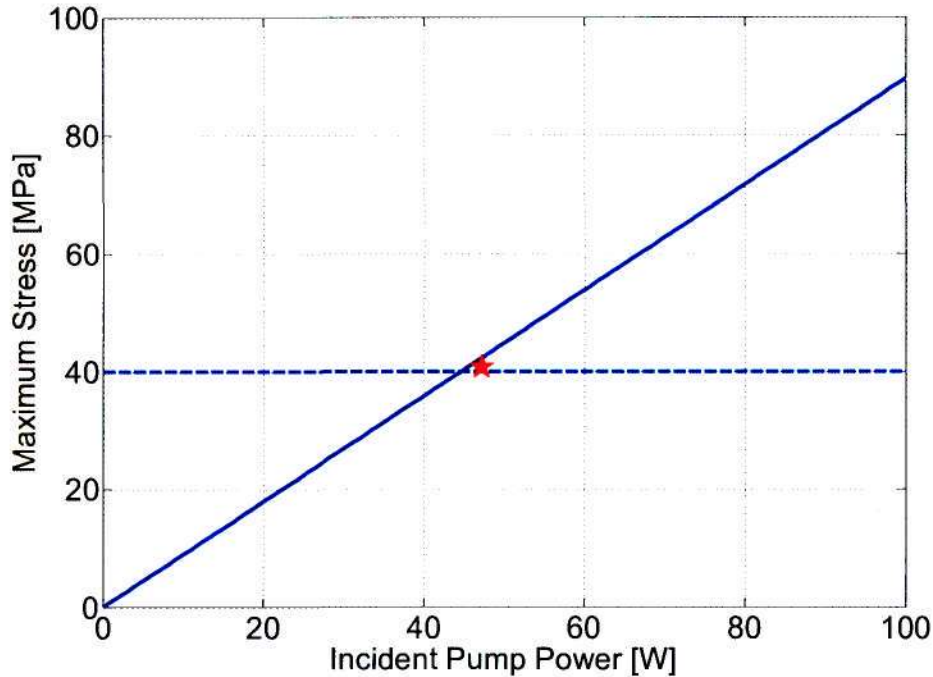


Figure 5.2: The analytical values for the maximum stress in the Tm:YLF rod as a function of incident pump power. The red star indicates the numerical fracture point, while the horizontal dashed blue line represents the fracture limit of YLF.

From Figure 5.3 it is clear that the maximum stress in the YLF rod increases monotonically while the pump pulse is present, reaching a maximum at the end of the pump pulse. This makes it possible to model a single “long” pulse for a particular incident power and simply consider the time that it takes for this incident pump power to induce a tensile stress in the material which is equal to the tensile strength of YLF. The time duration to reach the tensile strength is then considered to be the pulse duration that corresponds to that critical incident pump power (see Figure 5.4). For example, with an incident pump power of 100 W, it takes the YLF rod 40 ms to reach its tensile strength of 40 MPa.

With this approach it is possible to determine the critical incident pump power as a function of a single pump pulse length, as illustrated in Figure 5.5.

As a comparison, a Gaussian pump beam is compared to the quasi-top-hat pump beam. The transverse intensity profile of the pump beam (considering beams with the same size) seems to make no significant difference in the critical incident pump power and the induced stresses for a given QCW pulse duration.

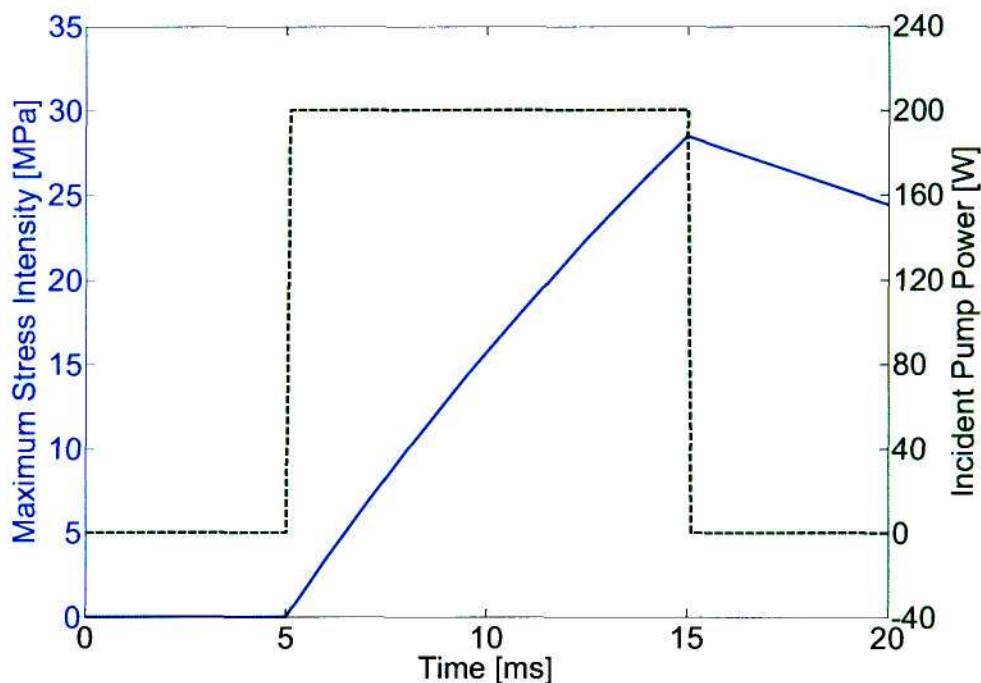


Figure 5.3: The maximum stress in the YLF rod during a single 10 ms QCW pump pulse with a peak power of 200W.

As can be expected, for long pulses the critical pump power at which fracture occurs, converges to the CW critical pump power of 47.2 W, while for a typical QCW pulse duration of 10 ms, fracture occurs at an incident pump power of ~ 250 W, which relates to an incident pump pulse energy of 2.5 J.

Although the critical pump power of a single pump pulse gives valuable information regarding the damage that a single QCW pump pulse can inflict on the laser rod, in practice the rod is pumped with a train of QCW pulses so that it is important to consider the stresses that are induced in the laser rod due to repetitive QCW pulses.

5.2 Duty Cycle

The primary reason for pumping a laser rod with a QCW pump is to reduce the thermal load in the crystal by reducing the average power that is incident on the laser rod.

In this discussion, the influence of the QCW pump duty cycle on the critical average power at which fracture occurs is investigated. The time dependent coupled thermal-

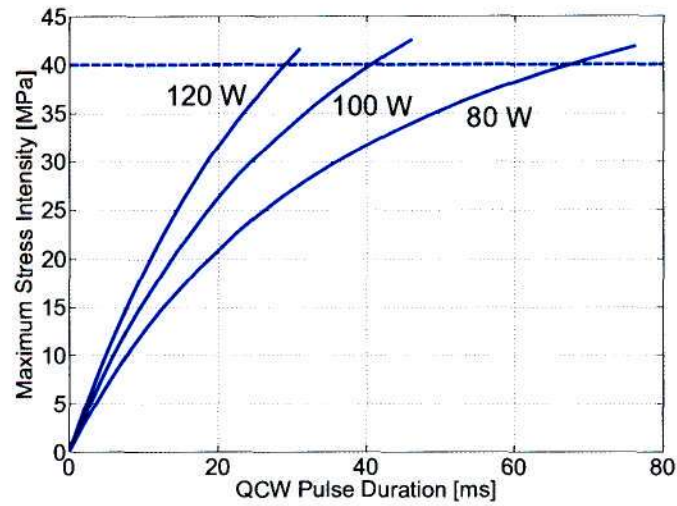


Figure 5.4: The maximum stress intensity as a function of time for various incident pump powers. The horizontal blue line shows the tensile strength of YLF.

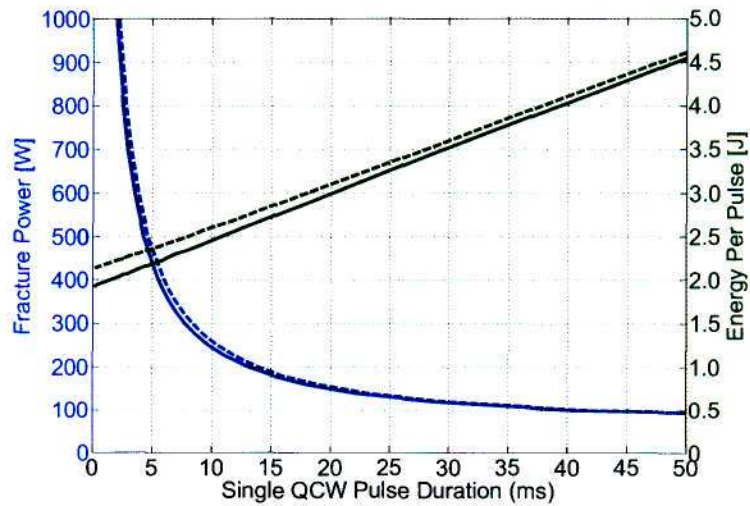


Figure 5.5: The critical incident pump power as a function of a single QCW pump pulse duration. The dotted line represents a top-hat pump beam and the solid line a Gaussian pump beam. The green curves show the energy that is deposited into the YLF crystal as a function of a single QCW pump pulse duration.

stress analysis was also implemented in ABAQUS.

Instead of considering a single QCW, the thermal stresses induced by a train of QCW pulses at various pump duty cycles are investigated.

Figure 5.6 shows the time dependence of the maximum tensile stress in the Tm:YLF rod that are induced by QCW pump pulses with 245 W peak power at a 2% duty cycle as well as pump pulses with a 80 W peak power at a 60% pump duty cycle. Note that the QCW on-time is 10 ms in all cases while the duty cycle is varied by changing the pulse repetition frequency.

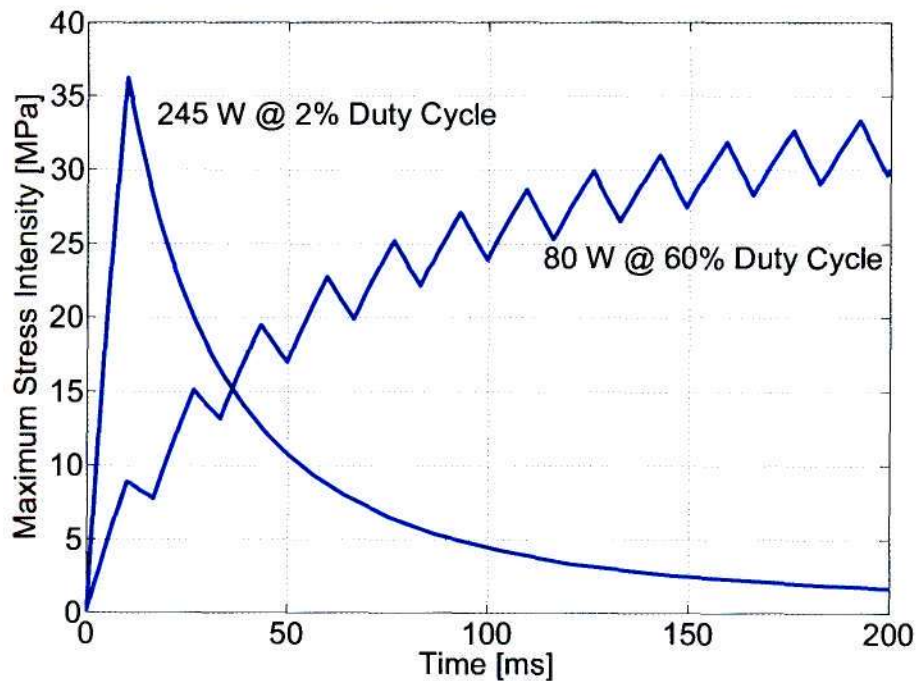


Figure 5.6: The time dependence of the maximum tensile stress in the Tm:YLF rod that are induced by various QCW pump powers and duty cycles.

It is generally believed that a laser rod that is pumped via a QCW pump beam will fracture at an average power which is roughly equal to the CW critical pump power. This hypothesis has been investigated specifically for the Tm:YLF rod that is under discussion.

In order to vary the duty cycle of the pump, the QCW pulse duration was fixed at 10 ms, while the pulse repetition frequency was changed. For the particular case of a 10 ms pump pulse, the duty cycle percentage and the pulse repetition frequency are

the same. In other words, for repetitive pump pulses of 10 ms, a QCW duty cycle of 50% is equivalent to a pulse repetition frequency of 50 Hz.

For duty cycles higher than $\sim 50\%$, it is true that fracture of the Tm:YLF rod occurs at an average power which is equal to the CW critical pump power of 47.2 W. At low duty cycles ($< 50\%$), fracture of the laser rod occurs at average powers that are substantially lower than the CW critical pump power. For a typical QCW duty cycle of 20%, fracture occurs at an average power that is $\sim 70\%$ that of the CW critical pump power. Figure 5.7 shows the average pump power (expressed as a percentage of the CW critical pump power) at which fracture occurs, as a function of pump duty cycle.

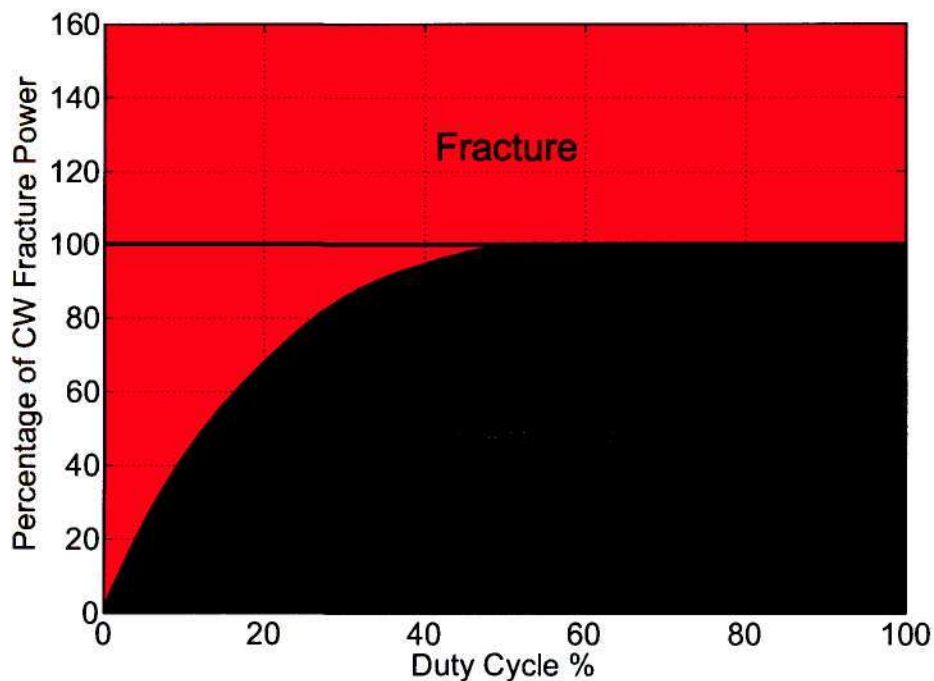


Figure 5.7: The average pump power (expressed as a percentage of the CW critical pump power) at which fracture occurs, as a function of pump duty cycle (fixed QCW on-time of 10 ms).

A possible reason for the deviation of the critical average pump power from the CW critical pump power at low duty cycles, is the fact that the peak power of the individual pulses is very high for low duty cycles. At a duty cycle of 10%, incident peak power is 200 W (see Figure 5.8). The high peak power results in a heat load that is too high to be completely dissipated in the laser rod before the next pump pulse strikes. It seems that this deviation from the CW critical pump power at low duty

cycles, is merely a limitation of the thermal conductivity of the material. The average power fracture limit in laser materials with a higher thermal conductivity should be closer to the CW critical pump power at low duty cycles.

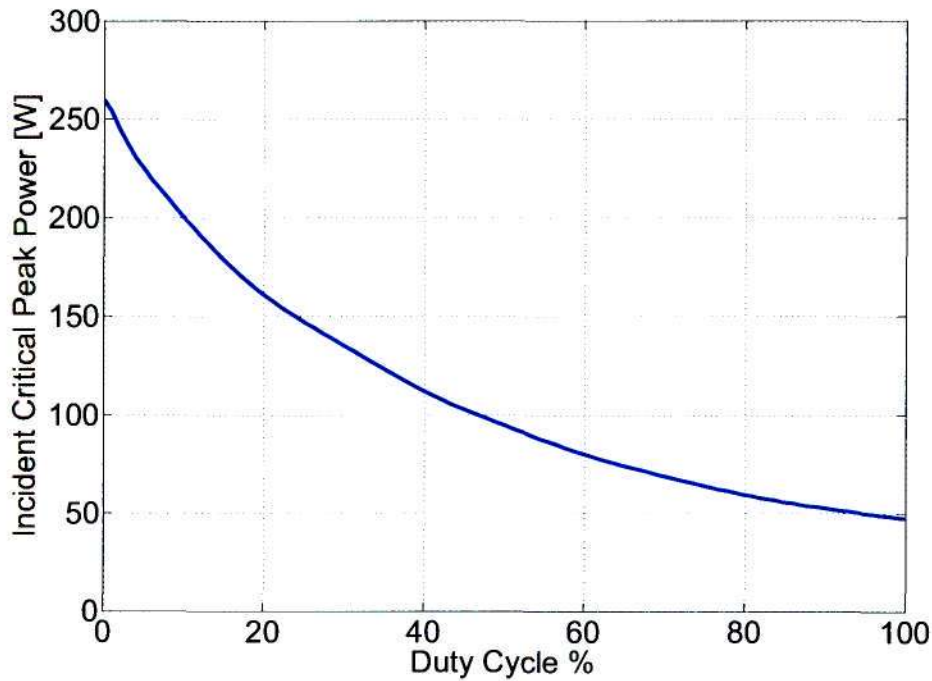


Figure 5.8: The incident peak power at which fracture occurs as a function of pump duty cycle.

5.3 Summary

To calculate the thermally induced stresses inside a Tm:YLF laser rod numerically, a time dependent finite element analysis was implemented in a commercial software package, ABAQUS. The model was validated for the CW pump case by comparing the numerical results with experimental values that were taken from (So *et al.*, 2006). This was followed by a time dependent analysis to show the critical pump power for various pulse lengths and pump duty cycles.

There seems to be no significant difference in the time dependent thermally induced stresses when a top-hat pump profile is used as opposed to a Gaussian pump profile.

CHAPTER 5. QUASI-CONTINUOUS WAVE PUMPED Tm:YLF ROD

For duty cycles higher than $\sim 50\%$ the fracture of the Tm:YLF rod occurs at average powers which are equal to the CW critical pump power. At low QCW pump duty cycles ($< 50\%$), fracture of the Tm:YLF rod occurs at significantly lower average pump powers than the critical pump power in the CW case. The deviation at lower duty cycles is due to the inability of the material to dissipate the high heat load (due to high peak powers) between pulses.

Chapter 6

A Time-Dependent Analytical Thermal Model

The time-dependent analytical thermal model for laser rods that is presented in this chapter was done after this dissertation was completed. This chapter includes a summary of the work as it was accepted for the 3rd EPS-QEOD Europhoton Conference to be held from 31 August - 5 September 2008, Paris, France. This work has also been published in a peer-reviewed journal (Bernhardi *et al.*, 2008a).

One of the main problems that limit the power scaling of diode-end-pumped solid-state lasers is the generation of heat inside the laser gain medium which can ultimately cause fracture. When the continuous wave (CW) pump power exceeds the critical power at which crystal fracture occurs, a quasi-continuous wave (QCW) pump is often used to reduce the average pump power to below the fracture pump power.

In previous work, we investigated the time-dependence of the temperature and the thermally induced stresses in QCW-pumped Tm:YLF laser rods by means of finite element numerical simulations (Bernhardi *et al.*, 2008b). This enabled the prediction of the incident fracture power as a function of QCW-pump duty cycle.

In this paper a time-dependent analytical thermal model that determines the temperature and the thermally induced stresses in isotropic rods is presented. Even though the model is developed for isotropic rods, it is shown that it can also be used to accurately estimate the thermal effects in anisotropic rods. By ignoring axial heat-flow in the radially symmetric rod, the temperature profile on the pumped face of the rod is given by

$$T(r, t) = \sum_{m=1}^{\infty} \int_0^R \int_0^t \frac{2s J_0\left(\frac{\mu_m r}{R}\right) J_0\left(\frac{\mu_m s}{R}\right) Q(s, \tau) e^{-\frac{D\mu_m^2(t-\tau)}{R^2}}}{R^2 J_1^2(\mu_m)} d\tau ds \quad (6.1)$$

where R is the radius of the rod, J_i is a Bessel-function of the first kind with order i , μ_m are the roots of J_0 and $D = k/(\rho c_p)$ with k the thermal conductivity, ρ the density and

c_p the specific heat capacity of the laser rod. $Q(r, t) = I(r, t)\alpha/(\rho c_p)$ is the heat load where $I(r, t)$ is the transverse pump intensity profile and α is the absorption coefficient at the pump wavelength. In the case of a top-hat transverse pump profile, equation 6.1 reduces to

$$T(r, t) = \sum_{m=1}^{\infty} \frac{2wJ_0(\frac{\mu_m r}{R})J_1(\frac{\mu_m w}{R})}{J_1^2(\mu_m)\mu_m R} \int_0^t Q(r, \tau)e^{-\frac{D\mu_m^2(t-\tau)}{R^2}} d\tau \quad (6.2)$$

where w is the pump beam radius. The integral in equation 6.2 can easily be solved numerically for a QCW-pumped laser.

Figures 6.1 & 6.2 show the temperature in the centre of the pumped-face of the Tm:YLF rod as a function of time while the rod is subjected to two different QCW-pump power and pulse repetition frequencies. The analytical model reduces the computation time of the thermal effects from ~ 5.5 hours in the case of the finite element numerical model to less than a minute. By using the analytical model, it is possible to efficiently calculate the thermal influence of various pump scenarios within a short time.

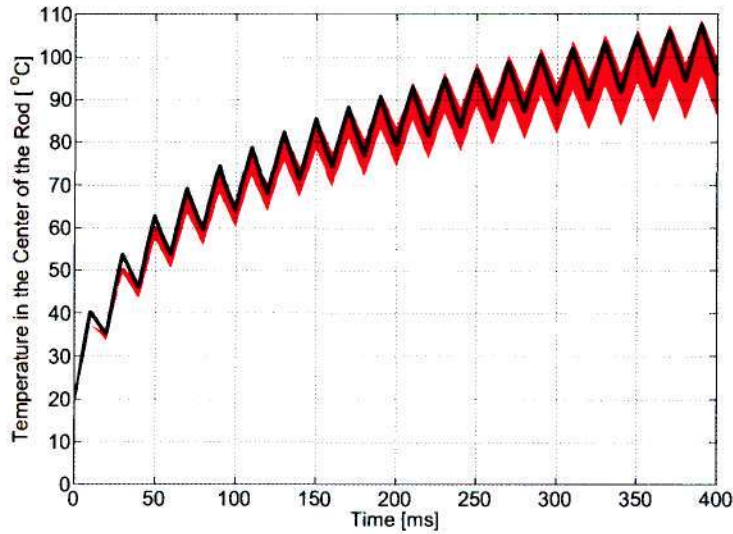


Figure 6.1: The temperature in the centre of the Tm:YLF rod as a function of time while the rod is subjected to a QCW-pump of 90 W @ 50 Hz. The two respective boundaries of the shaded regions indicate the analytical solution as determined with the thermal conductivity of the a- and c-axis of YLF respectively. The black curve shows the solution of the three-dimensional time-dependent coupled-thermal-stress finite element numerical simulation.

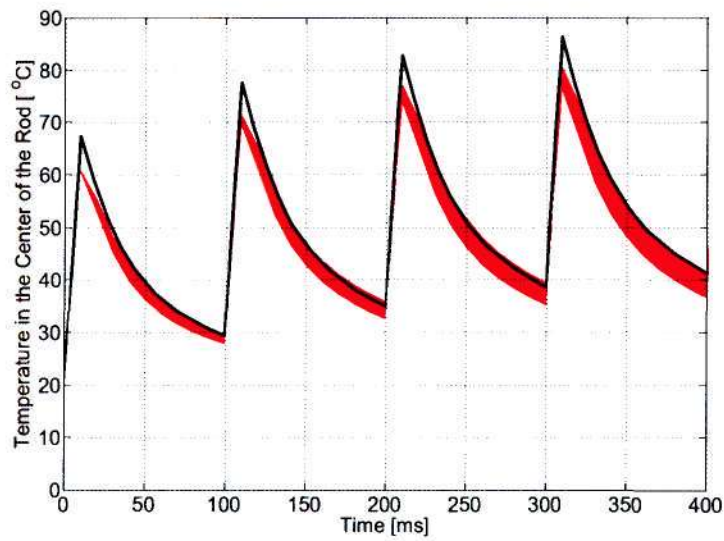


Figure 6.2: The temperature in the centre of the Tm:YLF rod as a function of time while the rod is subjected to a QCW-pump of 200 W @ 10 Hz. The two respective boundaries of the shaded regions indicate the analytical solution as determined with the thermal conductivity of the a- and c-axis of YLF respectively. The black curve shows the solution of the three-dimensional time-dependent coupled-thermal-stress finite element numerical simulation.

Part III

**Rate-Equation Modelling of
Solid-State Lasers**

Chapter 7

Introduction to Rate-Equation Modelling

7.1 Overview

The entire theory that describes laser rate-equations can be found in standard textbooks such as (Loudon, 1983)(Siegman, 1986)(Koechner, 1996). The rate-equations in these textbooks are derived for idealised three- and four-level lasers.

An alternative to the idealised three- and four-level laser models was proposed by Fan & Byer in the form of a quasi-three-level rate-equation model (Fan & Byer, 1987). The main difference between the conventional three-and four-level rate-equation models and the quasi-three-level model is that the latter accounts for the Stark levels within each energy manifold .

In this early work, Fan assumed a perfect overlap between the pump mode and the fundamental laser mode. The model provided a very good understanding of the reabsorption losses in quasi-three-level lasers which enabled him to model the threshold and efficiency with great accuracy.

Building on the foundation that Fan provided, Risk has accounted for the effect of the relative sizes of the pump- and laser beams (Risk, 1988). The influence of the ratio of the pump beam size to laser beam size on the threshold and efficiency of the laser has been investigated in order to find the ratio for which the laser efficiency is at an optimum.

Fan later used his quasi-three-level rate-equation model to investigate the energy storage in Yb:YAG and found that the energy storage in this gain element can at least be as sufficient as that of a four-level Nd:YAG laser (Fan, 1992).

The quasi-three-level rate-equation was then extended to include the dynamics of a co-doped Tm,Ho:YAG laser (Sousa *et al.*, 1997). No upconversion was included in this model.

At about the same time Rustad & Stenersen implemented a rate-equation model for co-doped Tm,Ho which also accounts for upconversion energy transfer in both the Thulium and Holmium ions (Rustad & Stenersen, 1996).

More recently Schellhorn & Hirth have adapted the quasi-three-level rate-equations to model the population dynamics of a novel intracavity configuration where a Ho:YAG laser was intracavity-pumped by a Tm:YLF laser (Schellhorn & Hirth, 2002).

The rate-equations that are discussed and implemented in this work are quasi-three-level rate-equations.

7.2 The Rate-Equation Approximation

In order to develop a comprehensive mathematical model which can explain the operation of a laser, a full quantum mechanical approach can be taken. In such a model, the electromagnetic field as well as the atomic systems are described by quantum mechanical principles which makes the model complex and computationally intensive.

When the bandwidth of the incident light is greater than the particular laser transition linewidth, the atomic system and electric field can be described classically by making use of rate equations (Loudon, 1983). The equivalent of this condition is to require that the energy level population and the electric field don't change significantly within the atomic coherence time (Rustad, 1994).

The rate equations that govern the transient behaviour of the atomic system and the induced electric field are written in a simplified form as (Rustad, 1994)

$$\frac{dN_2}{dt} = R_2 - \frac{N_2}{\tau_2} - \sigma c \Phi (N_2 - N_1) \quad (7.1)$$

$$\frac{dN_1}{dt} = R_1 - \frac{N_1}{\tau_1} + \sigma c \Phi (N_2 - N_1) \quad (7.2)$$

$$\frac{d\Phi}{dt} = \Phi \frac{Gain_{RT} - Loss_{RT}}{Time_{RT}} \quad (7.3)$$

where N_2 and N_1 are the population densities of the upper and lower laser levels respectively. Φ is the laser photon density in the resonator, τ_2 and τ_1 are the lifetimes of the respective energy levels, σ is the stimulated emission cross-section, c is the speed of light and the RT subscript denotes resonator roundtrip.

The R_2 and R_1 in the first term of the population density equations 7.1 & 7.2 represent the excitation rate into the particular energy level. The second term is due to the spontaneous emission out of the energy levels, while the last term is the stimulated emission laser action.

Other mechanisms such as energy-transfer-upconversion which can also change the population density of a particular energy level are omitted in the simplified rate-equations in this section.

7.3 Idealised Laser Models

In this section a brief description of the idealised three- and four-level laser models are given so that they can be compared to the quasi-three-level model. This discussion of idealised laser models is equivalent to that of (Fan, 1995).

7.3.1 Four-Level Lasers

Consider the energy-level scheme in Figure 7.1 which illustrates the operation of an optically pumped four-level laser.

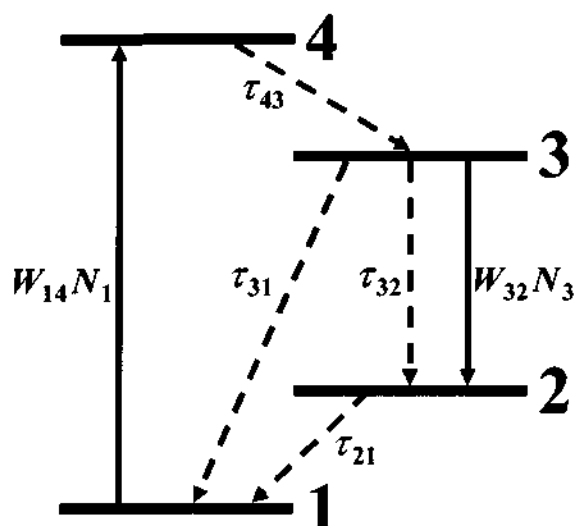


Figure 7.1: A schematic diagram of an idealised four-level laser model (Fan, 1995). See text for a description of all the symbols.

Initially all the atoms of the gain medium are in the ground level 1. The pump radiation excites the atoms from the ground level into level 4. The transition time (τ_{43}) is assumed to be infinitely fast so that the atoms in level 4 decay rapidly into the upper laser level 3. This is a non-radiative transition in which the energy difference between the levels is transferred to the crystal in the form of heat. Due to the infinitely fast decay time, the population density of level 4 is assumed to be zero. The laser action occurs when the atoms are transferred from level 3 into level 2 via the process of stimulated emission. In addition to the stimulated emission process, the atoms can also decay from level 3 into level 2 by spontaneous emission. From level 2, the transition time (τ_{21}) to the ground level 1 is again assumed to be infinitely fast so that level 2 has

a population density of zero. In this non-radiative transition, the energy difference between level 2 and 1 is transferred to the crystal in the form of heat. The relaxation from level 3 directly into the ground level 1 is usually associated with fluorescence.

Since levels 4 and 2 have population densities of zero, the system effectively reduces to a two-level model which only accounts for the population densities in levels 3 and 2. Due to the fact that level 2 is assumed to be empty in the four-level laser model, there exists a population inversion as soon as level 3 is populated.

The rate of change in the population inversion density between the upper and lower laser levels can be explained by the following rate-equation (Fan, 1995)

$$\frac{d\Delta N}{dt} = W_{14}N_1 - \frac{\Delta N}{\tau_3} - 2W_{32}\Delta N \quad (7.4)$$

where $\Delta N = N_3 - N_2 = N_3$ and W_{ij} is a rate constant given by

$$W_{ij} = \frac{\sigma I_{ij}}{h\nu_{ij}} \quad (7.5)$$

where the ij subscript denotes a transition from level i to j . I_{ij} is the intensity of the light that has a photon energy of $h\nu_{ij}$ and σ is the spectroscopic cross-section.

Note that the spontaneous emission processes out of the upper laser level 3 is denoted by τ_3 which accounts for all the radiative and non-radiative spontaneous transitions out of the upper laser level.

The time dependence of the laser light intensity in the laser cavity can be described by (Fan, 1995)

$$\frac{dI_{32}}{dt} = cW_{32}\Delta N h\nu_{32} - \frac{I_{32}}{\tau_c} \quad (7.6)$$

where c is the speed of light and τ_c is the cavity-lifetime denoted by

$$\tau_c = \frac{2L}{c\delta} \quad (7.7)$$

with L the optical length of the cavity and δ the logarithmic roundtrip cavity losses that includes the loss of the output coupler. The first term in equation 7.7 represents the roundtrip gain in the resonator while the second term denotes the roundtrip loss in the resonator.

The most widely-used solid-state laser, namely the 1064 nm Nd:YAG laser is a very good example of a four-level laser.

7.3.2 Three-Level Lasers

The main difference between the three- and four-level laser models is the fact that the ground level is the lower laser level in the case of the three-level model. Figure 7.2 shows a schematic diagram which illustrates the operation of a three-level laser.

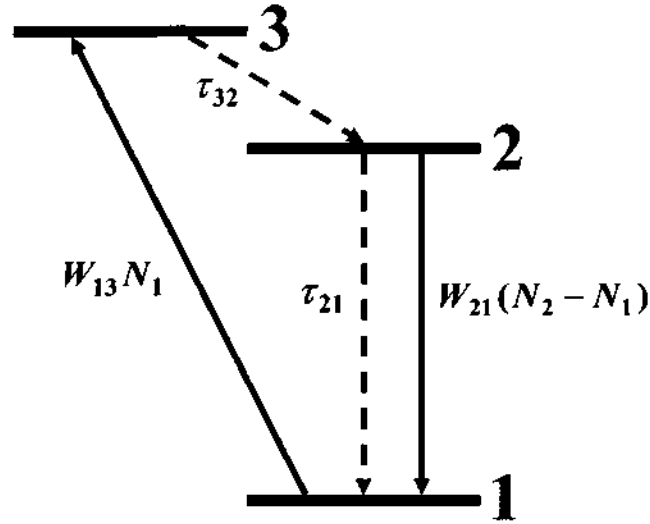


Figure 7.2: A schematic diagram of an idealised three-level laser model (Fan, 1995). See text for a description of all the symbols.

To begin with, the atoms are in the ground level 1. The incident pump radiation causes the atoms to be excited into level 3. Similarly to the four-level laser the non-radiative transition between the upper pump level and the upper laser level is assumed to be infinitely fast so that the population density in level 3 is zero. The assumption of an infinitely fast transition between level 3 and 2 effectively reduces the model to a two level model. The laser action transfers atoms from level 2 into level 1 with the process of stimulated emission. Since the lower laser level is in fact the ground level, it is possible for an atom in the ground level to absorb a laser photon and be excited to level 2 again. The reabsorption of the laser light introduces an additional loss in the system. Due to the fact that there are essentially only two energy levels, more than half of the atoms have to be pumped into the upper laser level 2 in order to reach a population inversion. This causes that more atoms to contribute to the non-radiative transition between levels 3 and 2 which adds heat to the crystal. Even more significant is that the populated lower laser level results in a higher laser threshold than in the case of a four-level laser. The rate-equation that describes the population inversion in the three-level laser model is given by (Fan, 1995)

$$\frac{d\Delta N}{dt} = 2W_{13}N_1 - \frac{N_T + \Delta N}{\tau_2} - 4W_{21}\Delta N \quad (7.8)$$

where $\Delta N = N_2 - N_1$ and $N_T = N_1 + N_2$.

The additional factor of two that is present in the pump and stimulated emission terms is due to the system that comprises of the upper and lower laser level. This implies that an atom that is pumped from the ground level 1 into the upper laser level 2, changes the population inversion by two. The same argument is true for the stimulated emission laser action which transfers atoms from the upper laser level into the ground level. The transient behaviour of the laser light intensity is written in analogy to the four-level laser as (Fan, 1995)

$$\frac{dI_{21}}{dt} = cW_{21}\Delta N h\nu_{21} - \frac{I_{21}}{\tau_c} \quad (7.9)$$

Due to the reabsorption loss in three-level lasers, they are less efficient and require higher pump densities than four-level lasers. A good example of a laser which operates according to the three-level model is a ruby laser.

7.4 Quasi-Three-Level Lasers

The discussion of quasi-three-level lasers in this section is analogous to that of (Fan, 1995).

The most significant difference between a quasi-three-level laser model and the previous idealised models is the fact that the former accounts for the Stark levels within each manifold (Fan, 1995). The Stark levels form as the electric field in the crystal perturbs the energy levels. In rare-earth ions the separation between the individual Stark levels are small because of the shielding from the outer xenon-shell which limits the effect of the crystal field. Figure 7.3 shows the energy-level diagram of a quasi-three-level Tm:YAG laser where the Stark levels within each manifold can be clearly seen. Cross-relaxation is not shown in this figure and will be discussed in Chapter 10. Other examples of quasi-three-level lasers include the ${}^4F_{3/2} \rightarrow {}^4I_{9/2}$ transition in Nd^{3+} and the ${}^5I_7 \rightarrow {}^5I_8$ transition in Ho^{3+} .

To simulate the population density of each Stark levels with a separate rate-equation will result in a complex system of coupled differential equations. In order to simplify the approach, the concept of quasi-thermal equilibrium is introduced (Fan & Byer, 1987). This assumes that the population distribution between the Stark levels within an energy manifold at any given time, is given by a Boltzmann distribution as if the material is in thermal equilibrium. Quasi-thermal equilibrium is a valid assumption if the relaxation time within a manifold is much faster than the time in which the population density changes significantly. For a Q-switched laser the population density typically changes in the nano-second regime.

Let the upper laser manifold be 2 and the lower laser manifold be 1 as illustrated in Figure 7.4. The particular Stark level within the upper manifold from which the laser action occurs is b while the transition terminates in Stark level a in the lower

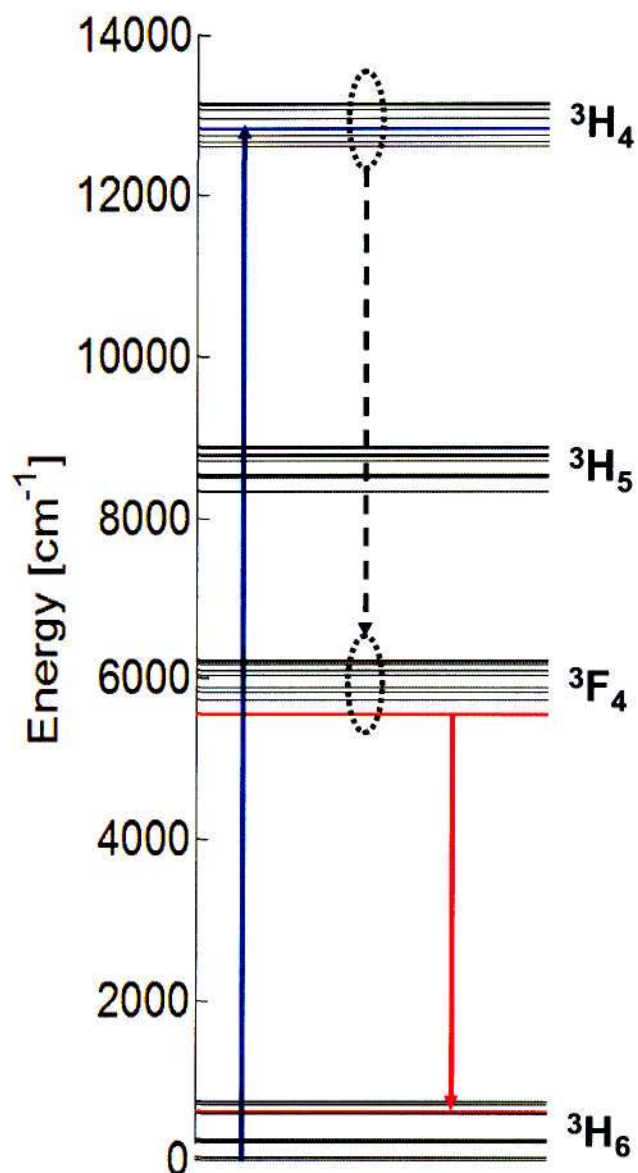


Figure 7.3: The energy diagram of Tm:YAG. The blue arrow indicates the pumping process (780 nm) and the red arrow the laser transition (2022 nm). The dashed line shows the rapid decay from the pump manifold into the upper laser manifold.

laser manifold. From the assumption of quasi-thermal equilibrium it follows that the fraction of the upper manifold population that is in Stark level b can be written as (Fan & Byer, 1987)

$$f_b = \frac{g_b e^{-(E_b - E_0)/kT}}{Z_1} \quad (7.10)$$

where g_b is the degeneracy of Stark level b , E_0 is the energy of the lowest Stark level in the upper manifold and

$$Z_2 = \sum_{i=1}^m g_i e^{-(E_i - E_0)/kT}$$

E_b is the energy of Stark level b , kT is the thermal energy and Z_2 is the partition function of the upper manifold. E_i and g_i are respectively the energies and degeneracies of the upper manifold which consists of m Stark levels. The fraction of the population of the lower laser manifold that is found in Stark level a , is found in a similar way by determining the partition function over the energy levels in the lower manifold and setting $E_0 = 0$.

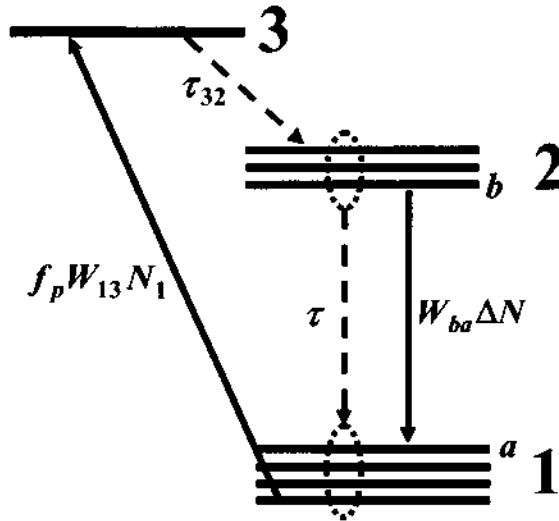


Figure 7.4: A schematic diagram of a quasi-three-level laser model (Adapted from (Fan, 1995)). See text for a description of all the symbols.

The population dynamics of a quasi-three-level laser can be explained in the following way. Initially all the atoms are assumed to be in manifold 1 (Figure 7.4). From the assumption of quasi-thermal equilibrium, let the fraction of the population of manifold 1 that is found in the lower pump level be f_p . The pump radiation transfers atoms

from manifold 1 into the upper pump level from where they quickly decay into the upper laser manifold 2. Similar to the previous idealised laser models, the decay from the upper pump level to the upper laser manifold is instantaneous and the energy difference between the levels is converted into heat. As discussed, the upper and lower laser manifolds are assumed to have an instantaneous Boltzmann distribution so that the population density of the upper laser level is given by $f_b N_2$ while the lower laser level population density is denoted by $f_a N_1$. Atoms are transferred from Stark level b (in manifold 2) to Stark level a (in manifold 1). The spontaneous radiative and non-radiative transitions from manifold 2 into manifold 1 can be from all the Stark levels in manifold 2 into all the Stark levels in manifold 1 and the total decay time is defined as τ .

The rate-equation that describes the population inversion in a quasi-three-level laser can be written as (Fan, 1995)

$$\frac{d\Delta N}{dt} = f_p(f_a + f_b)W_{13}N_1 - \frac{f_a N_T + \Delta N}{\tau} - 2(f_a + f_b)W_{ba}\Delta N \quad (7.11)$$

where $\Delta N = f_b N_2 - f_a N_1$ and N_T is the total dopant concentration.

The transient laser intensity in the cavity is give by (Fan, 1995)

$$\frac{dI_{ba}}{dt} = cW_{ba}\Delta N h\nu_{ba} - \frac{I_{ba}}{\tau_c} \quad (7.12)$$

Note that in the special case where $f_a \rightarrow 0$, $f_p \rightarrow 1$ and $f_b \rightarrow 1$, equation 7.11 reduces to that of the idealised four-level laser (equation 7.4). If $f_a \rightarrow 1$, $f_p \rightarrow 1$ and $f_b \rightarrow 1$, it reduces to the idealised three-level laser (equation 7.8). The quasi-three-level laser model is versatile enough to be able to describe the population dynamics of three- and four-level lasers as will be shown in later chapters.

Chapter 8

A Single-Element Plane-Wave Rate-Equation Model

In this chapter, a general spatially-resolved quasi-three-level rate-equation model is developed from existing theory. In order to simplify the implementation of the model as a computer simulation, the spatially-resolved model is initially reduced to a single-element plane-wave model.

8.1 Spatially Resolved Rate-Equation Model

In this section the population dynamics of a time and spatially dependent quasi-three-level laser as illustrated in Figure 8.1 is discussed in detail.

8.1.1 Energy-Level Population Densities

Instead of considering the transient variation of the population inversion as in equation 7.11, the time variation of the upper and lower laser manifolds are considered individually. Assume that the principle of quasi-thermal equilibrium can be applied within each manifold (Section 7.4). It follows that the population density of the upper laser manifold can be described in analogy to (Fan, 1992) as

$$\frac{dN_2}{dt} = \left(\frac{\sigma_P(I_P^+ + I_P^-)}{h\nu_P} \right) (f'_a N_1 - f'_b N_2) - \left(\frac{\sigma_L(I_L^+ + I_L^-)}{h\nu_L} \right) (f_b N_2 - f_a N_1) - \frac{N_2}{\tau_2} \quad (8.1)$$

where I_P^+ is the pump intensity travelling to the right and I_P^- is the pump intensity travelling to the left (for double pass pumping or pumping from both directions) in the resonator and a similar notation is used for the laser intensity I_L . f'_a and f'_b are the fractional populations within the lower and upper manifold of the lower and upper levels of the pump transition respectively. Similarly, f_a and f_b are the fractional

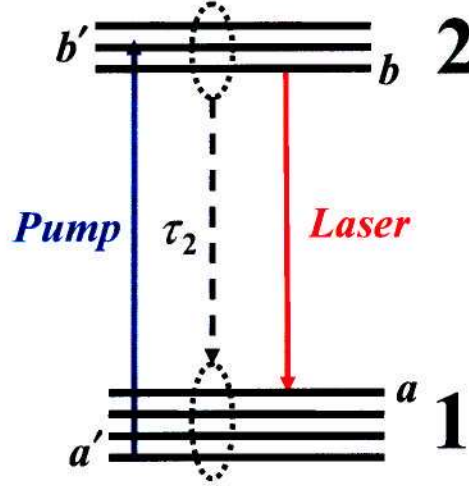


Figure 8.1: A schematic diagram of a quasi-three-level laser model. See text for a description of all the symbols.

populations within the lower and upper manifold of the lower and upper levels of the laser transition respectively. The spectroscopic absorption cross-section at the pump wavelength is denoted by σ_P , while σ_L the spectroscopic emission cross section at the laser wavelength. τ_2 is the spontaneous emission lifetime of the entire upper laser manifold. $h\nu_P$ is the energy of a pump photon while $h\nu_L$ is the energy of a laser photon. The total doping concentration is given by $N_T = N_1 + N_2$. The first term in equation 8.1 describes the pumping process, the second term represents the stimulated emission process while the last term is due to spontaneous emission. The population densities as well as the pump and laser light intensities in this section are all functions of the spatial coordinates x, y, z and time t . For notational purposes, the dependence isn't indicated in this section.

Note that the spectroscopic cross sections are defined between individual Stark levels. When it is not possible to determine the spectroscopic cross sections for all the possible individual Stark level transitions due to many overlapping transitions, the effective cross sections are used instead of the spectroscopic cross sections (Fan, 1995). For the pump transition, the effective absorption cross section is given by (Fan, 1995)

$$\sigma_P^{abs} = f'_a \sigma_P \quad (8.2)$$

Similarly, the effective emission cross section is defined as

$$\sigma_P^{em} = f'_b \sigma_P \quad (8.3)$$

The effective cross-sections for the laser transition are defined in the same way with the P subscript that is replaced by L . By making use of the effective cross sections, equation 8.1 can now be written as

$$\frac{dN_2}{dt} = \left(\frac{I_P^+ + I_P^-}{h\nu_P} \right) (\sigma_P^{abs} N_1 - \sigma_P^{em} N_2) - \left(\frac{I_L^+ + I_L^-}{h\nu_L} \right) (\sigma_L^{em} N_2 - \sigma_L^{abs} N_1) - \frac{N_2}{\tau_2} \quad (8.4)$$

Equation 8.4 is more convenient to use than equation 8.1 since it is not necessary to know the spectroscopic cross section for all the possible Stark level transitions that contribute to a particular wavelength. The measured effective cross section already includes all the possible transitions that contribute to a particular wavelength. For example, suppose that there are two transitions that contribute to the laser wavelength. The first transition has a spectroscopic emission cross section of σ_{2b} and occurs from Stark level b (with population density N_{2b}) in manifold 2 into Stark level a in manifold 1. The second transition has a spectroscopic emission cross section of σ_{2d} and occurs from Stark level d (with population density N_{2d}) in manifold 2 into Stark level c in manifold 1. The stimulated emission term in equation 8.4 can then be written as

$$\begin{aligned} \frac{dN_2}{dt} &= \dots - \left(\frac{I_L^+ + I_L^-}{h\nu_L} \right) (\sigma_{2b} N_{2b} + \sigma_{2d} N_{2d} - \sigma_L^{abs} N_1) \dots \\ \frac{dN_2}{dt} &= \dots - \left(\frac{I_L^+ + I_L^-}{h\nu_L} \right) (\sigma_{2b} f_b N_2 + \sigma_{2d} f_d N_2 - \sigma_L^{abs} N_1) \dots \\ \frac{dN_2}{dt} &= \dots - \left(\frac{I_L^+ + I_L^-}{h\nu_L} \right) (\sigma_L^{em} N_2 - \sigma_L^{abs} N_1) \dots \end{aligned} \quad (8.5)$$

with $\sigma_L^{em} = \sigma_{2b} f_b + \sigma_{2d} f_d$ the effective emission cross section that is measured at the laser wavelength. The same approach is taken for σ_L^{abs} , σ_P^{abs} and σ_P^{em} . The measured effective cross sections account for degeneracies in the same way. Suppose that the upper laser Stark level b has a degeneracy of 2. Then it follows that the measured effective emission cross section is simply $\sigma_L^{em} = \sigma_{2b} f_b + \sigma_{2b} f_b$.

8.1.2 Pump Light Distribution

Assume a normalised transverse pump light distribution function ψ_P^+ so that

$$\int \int \psi_P^+(x, y, z) dx dy = 1 \quad (8.6)$$

for all z . The xy -plane is defined perpendicular to the incident pump light while z denotes the pump beam propagation direction. In each x - y slice of the crystal the integrated value of ψ_P^+ must be 1. This definition of a pump light distribution function is general enough to allow for pump beams with Gaussian, super-Gaussian or top-hat

transverse intensity profiles. The + superscript describes the pump light travelling in one direction as previously noted so that it can be changed to a – for the other propagating direction. Also assume that ψ_P^+ is independent of the population inversion and time. As an example, consider the case where ψ_P^+ is a Gaussian distribution and $w(z)$ is the pump beam radius at distance z from the pump beam waist so that

$$\psi_P^+(x, y, z) = \frac{2}{\pi w(z)^2} e^{-2(x^2+y^2)/w(z)^2} \quad (8.7)$$

The pump light intensity can be determined by

$$I_P^+(x, y, z, t) = P_P^+(z, t) \psi_P^+(x, y, z) \quad (8.8)$$

with P_P^+ the pump power. The propagation of the pump power along z can be described in analogy to (Fan, 1992) as

$$\frac{dP_P^+}{dz} = -P_P^+ \int \int \psi_P^+(x, y, z) (\sigma_P^{abs} N_1 - \sigma_P^{em} N_2) dx dy \quad (8.9)$$

Note that P_P^+ , N_1 and N_2 are functions of the spatial coordinates x, y, z and time t . For notational purposes, the dependence isn't indicated in this equation.

8.1.3 Total Laser Photon Number and Laser Light Distribution

In the case of the pump light, the distribution was normalised in each xy -slice for a given z . In contrast, the laser light distribution ϕ_L is normalised over the entire volume of the resonator so that it is defined as

$$\int_{V_r} \phi_L(x, y, z) dV = 1 \quad (8.10)$$

where V_r is the volume of the laser beam inside the resonator.

If the output coupler has a relatively low transmission at the laser wavelength (typically less than 20%), then as a first approximation the laser power that travels towards the output coupler is roughly the same as the laser power that is reflected back into the resonator by the output coupler. From the low-loss approximation it follows that

- The laser power P_L doesn't vary with the propagation distance $\rightarrow \frac{dP_L}{dz} = 0$
- The laser light propagating towards the left (-) and the right(+) have equal power and intensity $\rightarrow P_L^+ = P_L^-$ and $I_L^+ = I_L^-$

The total laser light intensity ($I_L = I_L^+ + I_L^-$) is defined as (Rustad & Stenersen, 1996)

$$I_L(x, y, z, t) = \frac{h\nu_L c \Omega \phi_L(x, y, z)}{n(x, y, z)} \quad (8.11)$$

where Ω is the total number of laser photons in the resonator, $h\nu_L$ is the energy of a laser photon and $n(x, y, z)$ the refractive index at a point (x, y, z) in the resonator. The time dependence of Ω can be described by (Fan & Byer, 1987) (Risk, 1988)

$$\frac{d\Omega}{dt} = \frac{c\Omega}{n} \int_{V_r} (\sigma_L^{em} N_2(x, y, z) - \sigma_L^{abs} N_1(x, y, z)) \phi_L(x, y, z) dV - \frac{\Omega}{\tau_c} \quad (8.12)$$

where τ_c is the cavity lifetime as defined by equation 7.7.

The coupled differential equations 8.4 & 8.12 form the basis of the spatially resolved rate-equation model that can be used to describe the transient behaviour of the population densities and laser power.

8.2 Single-Element Plane-Wave Approximation

The single-element plane wave rate-equation approximation is based on the equations that were discussed in Section 8.1. Additional assumptions are implemented in order to make it easier to translate the model into a computer simulation of the laser. The main assumption in the single element approximations is that all the parameters in the model are assumed to be independent of their spatial coordinates (Figure 8.2). Instead of discretising the entire resonator volume and gain medium into finite elements and then solving the governing rate-equations for each finite element, the spatial dependence essentially collapses into a single element. The parameter values in the single element are then considered to be representative of that throughout the entire volume.

8.2.1 Energy-Level Population Densities

The approach in this section is to make use of the fact that parameters are spatially constant in order to reduce equation 8.4 into an equation that describes the transient behaviour of the upper laser manifold population density for the single-element plane-wave rate-equation model.

Pump Rate

The first term in equation 8.4 represents the transition of atoms from the ground manifold into the upper laser manifold via the optical pumping process. In the spatially resolved rate-equation model, the pump intensity is a function of the propagation distance in the laser gain medium. However, in the plane-wave single-element model,

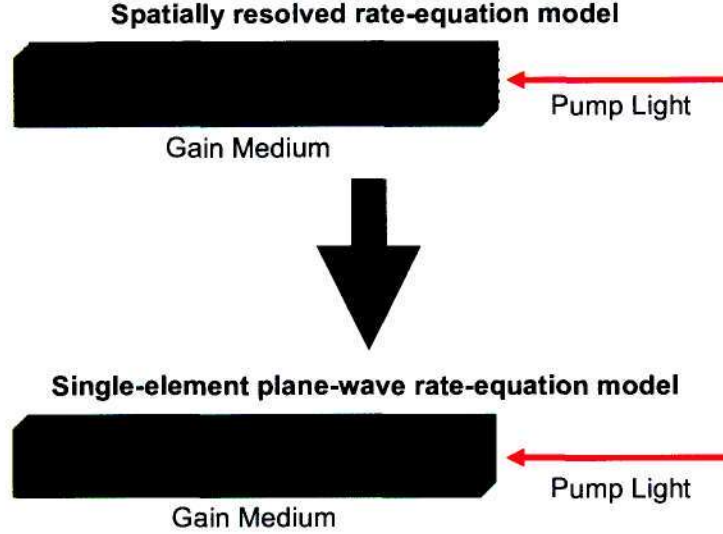


Figure 8.2: A comparison between the laser gain medium in the spatially resolved and single-element plane-wave models.

the pump light intensity in the gain medium is assumed to be constant and is taken as the average pump light intensity of the spatially resolved model. The propagation of the pump light in the gain medium is described by equation 8.9. Since the population densities are assumed to be spatially constant, it follows from equation 8.6 that equation 8.9 can be written as

$$\begin{aligned} \frac{dP_P}{dz} &= -P_P(\sigma_P^{abs} N_1 - \sigma_P^{em} N_2) \int \int \psi_P(x, y, z) dx dy \\ &= -P_P(\sigma_P^{abs} N_1 - \sigma_P^{em} N_2) \end{aligned} \quad (8.13)$$

Note that the pump power in equation 8.13 only accounts for the pump power that travels in one direction ($P_P = P_P^+$). For the case of double-pass pumping or pumping from both ends, the pump power from the other direction should also be taken into account. The Beer-Lambert absorption of the pump light in the gain medium is obtained by solving equation 8.13 so that

$$P_P(z) = \eta_P P_0 e^{-\alpha z} \quad (8.14)$$

where $\alpha = \sigma_P^{abs} N_1 - \sigma_P^{em} N_2$ is the absorption coefficient at the pump wavelength, η_P is the pump efficiency (i.e. the average number of ions in the upper laser manifold

CHAPTER 8. A SINGLE-ELEMENT PLANE-WAVE RATE-EQUATION MODEL

that are created per absorbed pump photon) and P_0 is the incident pump power. The average pump power in the laser gain medium (with length L_c) is given by

$$\begin{aligned} P_P^{ave} &= \left(\int_0^{L_c} P_P dz \right) / L_c \\ P_P^{ave} &= \left(\int_0^{L_c} \eta_P P_0 e^{-\alpha z} dz \right) / L_c \\ &= \frac{\eta_P P_0 (1 - e^{-\alpha L_c})}{\alpha L_c} \end{aligned} \quad (8.15)$$

The average intensity of the pump beam in the laser gain medium is then determined as

$$\begin{aligned} I_P^{ave} &= \frac{P_P^{ave}}{A} \\ &= \frac{\eta_P P_0 (1 - e^{-\alpha L_c})}{\alpha A L_c} \\ &= \frac{\eta_P P_0 (1 - e^{-\alpha L_c})}{\alpha V_c} \end{aligned} \quad (8.16)$$

By substituting the average intensity of equation 8.16 into the first term of equation 8.4 the following pump rate is attained

$$R_P = \frac{\eta_P P_0 (1 - e^{-\alpha L_c})}{h\nu_P V_c} \quad (8.17)$$

In the single-element plane-wave approximation, R_P denotes the rate at which atoms are excited into the upper laser manifold via the optical pumping process.

Stimulated Emission

The second term in equation 8.4 represents the transition of atoms from the upper laser manifold into the ground manifold via stimulated emission. The approach is to determine the average laser light intensity in the gain medium for the spatially resolved model and then to assume that to be the value of the laser light intensity for the single-element plane wave model.

The integral over the entire resonator volume of the laser photon distribution is determined in the following way (Figure 8.3)

$$\begin{aligned} \int_{V_r} \phi_L dV &= \int_{V_r} \phi_L dV \\ &= \int_{V_c} \phi_L dV + \int_{V_a} \phi_L dV \\ &= \int_A \int_0^{L_c} \phi_L dA' dz + \int_A \int_0^{L_a} \phi_L dA' dz \\ &= K(nL_c + L_a) \end{aligned} \quad (8.18)$$

CHAPTER 8. A SINGLE-ELEMENT PLANE-WAVE RATE-EQUATION MODEL

with

$$K = \int_A \phi_L dA \quad (8.19)$$

where A is the cross-sectional area of the laser beam. V_c is the volume of the laser beam inside the gain medium while V_r is the volume of the laser beam in the entire resonator so that $V_a = V_r - V_c$. The additional factor of n in the laser gain medium is due to the photons that travel slower in the gain medium so that there is a higher laser photon density in this region than in free space.

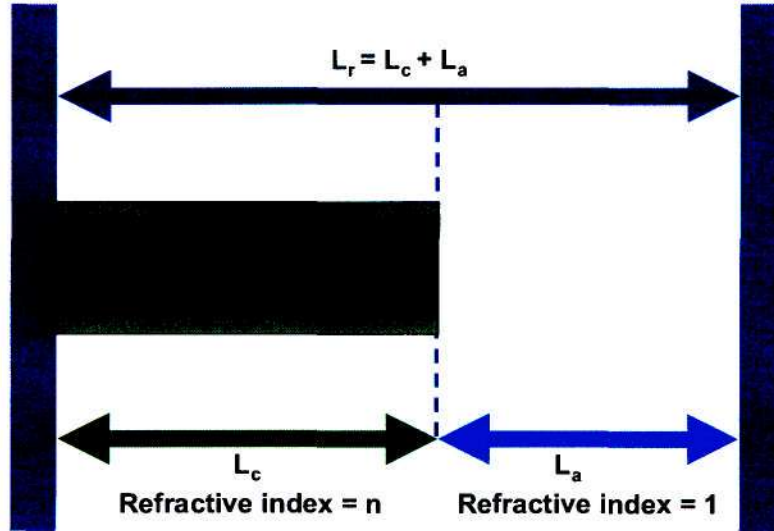


Figure 8.3: A schematic diagram of the resonator.

By combining equations 8.10 & 8.18 it follows that

$$\begin{aligned} \int_{V_c} \phi_L dV &= \frac{KnL_c}{K(nL_c + L_a)} \\ &= \frac{nL_c}{L_a + L_c + (n-1)L_c} \\ &= \frac{nL_c}{L_r + (n-1)L_c} \\ &= \frac{nL_c}{L_0} \end{aligned} \quad (8.20)$$

CHAPTER 8. A SINGLE-ELEMENT PLANE-WAVE RATE-EQUATION MODEL

where L_0 is the optical length of the resonator. Since the laser light distribution is considered to be uniform in the case of the single-element plane-wave approximation, equation 8.20 can be written as

$$\begin{aligned}\phi_L &= \frac{nL_c}{L_0V_c} \\ &= \frac{nL_c}{L_0AL_c} \\ &= \frac{n}{L_0A}\end{aligned}\tag{8.21}$$

For the single-element plane-wave rate-equation model, equation 8.21 can now be substituted into equation 8.11 so that the laser intensity in the gain medium is written as

$$I_L = \frac{h\nu_L c\Omega}{L_0A}\tag{8.22}$$

One of the assumptions in the spatially resolved rate-equation model is that $\frac{dP_L}{dz} = 0$. If it is assumed that the cross-sectional area of the beam (A) is constant in the gain medium it follows that $\frac{dI_L}{dz} = 0$ so that the laser intensity in the gain medium is constant. This implies that I_L is in fact the average laser intensity in the gain medium ($I_L^{ave} = I_L$).

By substituting the pump rate (equation 8.17) into the first term of equation 8.4 and equation 8.22 into the laser intensity of the second term of equation 8.4, the rate-equation then describes the transient behaviour of the upper laser manifold population density in the single-element plane-wave rate-equation model is

$$\frac{dN_2}{dt} = \frac{\eta_P P_0 (1 - e^{-\alpha z})}{h\nu_P V_c} - \frac{c\Omega}{AL_0} (\sigma_L^{em} N_2 - \sigma_L^{abs} N_1) - \frac{N_2}{\tau_2}\tag{8.23}$$

8.2.2 Total Laser Photon Number

Equation 8.12 describes the transient behaviour of the number of laser photons in the resonator. Since the population densities of the energy manifolds are zero outside of the gain medium, the integral limits change from the volume of the laser mode in the entire resonator (V_r) to the volume of the laser mode in the gain medium (V_c). From equation 8.20 and the fact that the population densities are spatially constant it follows that

$$\begin{aligned}\frac{d\Omega}{dt} &= \frac{c\Omega}{n} \int_{V_c} (\sigma_L^{em} N_2 - \sigma_L^{abs} N_1) \phi_L dV - \frac{\Omega}{\tau_c} \\ \frac{d\Omega}{dt} &= \frac{c\Omega (\sigma_L^{em} N_2 - \sigma_L^{abs} N_1)}{n} \int_{V_c} \phi_L dV - \frac{\Omega}{\tau_c}\end{aligned}$$

$$\begin{aligned}\frac{d\Omega}{dt} &= \frac{c\Omega \left(\sigma_L^{em} N_2 - \sigma_L^{abs} N_1 \right) n L_c}{n L_0} - \frac{\Omega}{\tau_c} \\ \frac{d\Omega}{dt} &= \frac{c\Omega L_c}{L_0} \left(\sigma_L^{em} N_2 - \sigma_L^{abs} N_1 \right) - \frac{\Omega}{\tau_c}\end{aligned}\quad (8.24)$$

In the single-element plane-wave rate-equation mode, equation 8.24 now replaces equation 8.12 to describe the transient behaviour of the number of laser photons in the resonator.

8.3 Summary

The spatially resolved rate-equations that describe the transient and spatial behaviour of the energy manifold population densities and the total number of laser photons in the resonator have been taken from literature and discussed in detail. A disadvantage of the spatially dependent rate-equation model is that the coupled rate-equations have to be solved for each point in space, which will ultimately result in a complex computer program that is computationally intense.

In order to simplify the implementation of the rate-equation model as a computer simulation, the spatial variation of the parameters are ignored so that the laser gain medium is treated as a single-element with spatially constant parameters. Since the spatial dependence is ignored, the pump and laser beams are treated as plane waves that are incident on the gain medium. With these assumptions, the set of coupled rate equations that govern the behaviour of the laser reduces to the following

$$\begin{aligned}\frac{dN_2}{dt} &= \frac{\eta_P P_0 (1 - e^{-\alpha z})}{h\nu_P V_c} - \frac{c\Omega}{AL_0} (\sigma_L^{em} N_2 - \sigma_L^{abs} N_1) - \frac{N_2}{\tau_2} \\ \frac{d\Omega}{dt} &= \frac{c\Omega L_c}{L_0} (\sigma_L^{em} N_2 - \sigma_L^{abs} N_1) - \frac{\Omega}{\tau_c}\end{aligned}$$

In order to describe the population dynamics and laser photon number in the single-element plane-wave rate-equation model, only these two coupled differential equations need to be implemented and solved in a computer simulation.

Chapter 9

Nd:YLF Laser

In this chapter, the single-element plane-wave rate equation model that has been developed in the previous chapter, is applied to a four-level Nd:YLF laser (Bollig *et al.*, 2008) (Bernhardi *et al.*, 2008c). The parameters that were used in the model as well as additional information on the laser are noted in Appendix A. These parameters were not adjusted in any way to fit the experimental data.

The model has been implemented in MATLAB where the two coupled ordinary differential equations (equations 8.23 & 8.24) were solved with MATLAB's ODE15s solver. A major advantage of this particular solver is that it has a variable time-step where the derivative of the function is validated with each time step. When the derivative is large (high activity) the time steps are decreased, whereas the time steps are increased when the derivative is small (little/no activity). This approach allows for a very quick and efficient way to solve the governing differential equations.

In addition to the numerically solved differential equations that are used to predict the laser's operation, analytical equations are also used to predict parameter behaviour where possible.

9.1 Experimental Setup

The experimental setup of the Nd:YLF laser is illustrated in Figure 9.1. A Jenoptik fibre-coupled diode module, capable of delivering a maximum power of 158 W at 805 nm, was used to pump the two Nd:YLF crystals. The fibre that was coupled onto the diode module had a core 0.6 mm and a numerical aperture of 0.22. Since the power that the diode-pump delivered was too much to pump a single crystal, the pump beam was split with a 55% mirror into two pump beams in order to pump the two crystals individually. For pulsed operation, an acousto-optic modulator (AOM) with a maximum loss of 65% was inserted into the resonator.

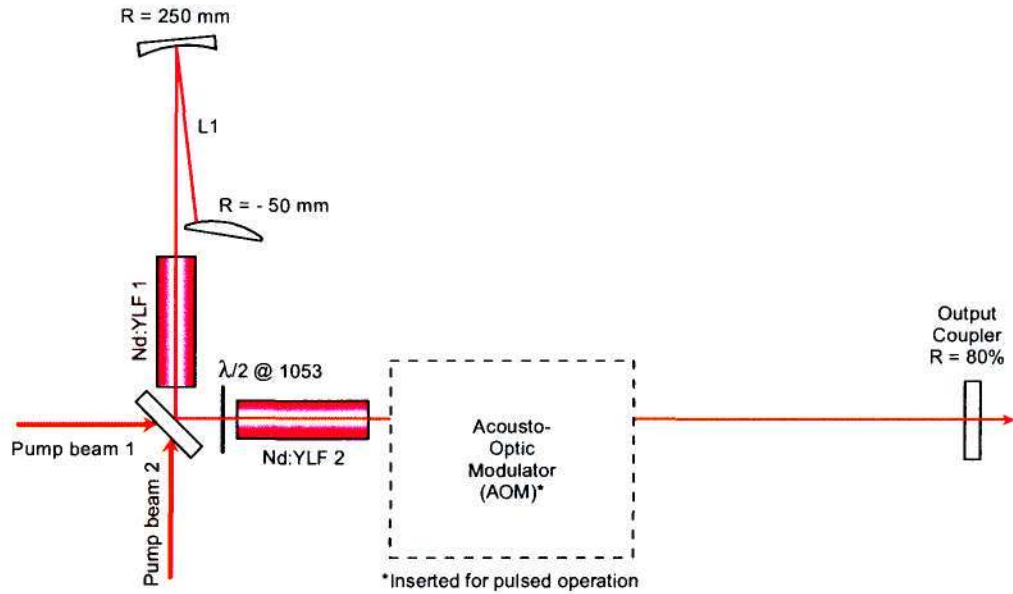


Figure 9.1: The experimental setup of the Nd:YLF laser (Bollig *et al.*, 2008).

9.2 CW Operation

9.2.1 Threshold and Efficiency

The laser threshold and efficiency are two of the most important values that the rate-equation model must be able to predict. For a four-level laser such as this Nd:YLF laser, there exist analytical estimations of the threshold and efficiency. The analytical solutions act as a further confirmation of the numerical rate-equation solution.

The threshold of the laser with respect to the absorbed pump power is given by (Fan & Byer, 1988)

$$P_{TH} = \frac{h\nu_P}{4\eta_P\sigma_L^{em}\tau}(A_P + A_L)(I + L) \quad (9.1)$$

where $h\nu_P$ is the energy of a pump photon, η_P the pump efficiency (the number of atoms that are excited into the upper laser manifold per absorbed pump photon), σ_L^{em} the effective emission cross section and τ the lifetime of the laser transition. A_P and

A_L are the cross-sectional areas of the pump and laser beams respectively. T is the output coupler transmission at the laser wavelength and L includes all other losses in the resonator except for the output coupler.

The slope efficiency of a four-level laser with respect to the absorbed pump power is given by (Fan & Byer, 1988)

$$\eta_{slope} = \eta_P \frac{h\nu_L}{h\nu_P} \left(\frac{T}{T + L} \right) \quad (9.2)$$

where $h\nu_L$ is the energy of a laser photon.

The laser had a threshold of 9.5 W and a maximum output power of 60.3 W at 158 W of incident pump power with a slope efficiency of 44% (Figure 9.2). The laser wavelength was measured to be 1053 nm.

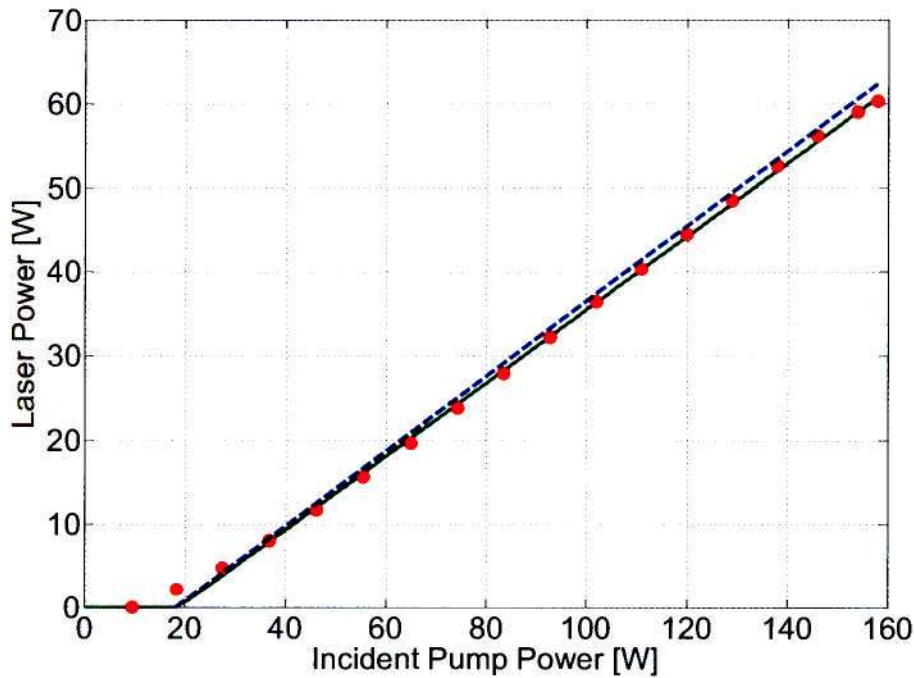


Figure 9.2: Power scaling of the Nd:YLF laser. The red dots represent experimental data while the green and blue lines are rate-equation and analytical solutions respectively.

Both the analytical equations and the rate-equation model are consistent with measured data as they both predict a threshold of 19 W with slope efficiency of $\sim 44\%$.

The reason for the slight overestimation of the threshold is due to the fact that the laser was optimised at full pump power, but not re-adjusted at lower powers. The rate-equation model is more versatile than the analytical equations since it can also be used to investigate time-dependent variations of the laser such as relaxation oscillations.

9.2.2 Relaxation Oscillations

Relaxation oscillations as it is referred to in this work, refers to the large amplitude spikes in the laser output power that are observed in most solid-state lasers when they are initially switched on. This behaviour is due to the recovery time of the population inversion that is much longer than the cavity decay time.

Figure 9.3 shows the photon number and population inversion of the Nd:YLF laser during the main relaxation oscillation spikes at full pump power (158 W). This particular laser has a cavity decay time of 28 ns and an upper manifold lifetime of 520 μs .

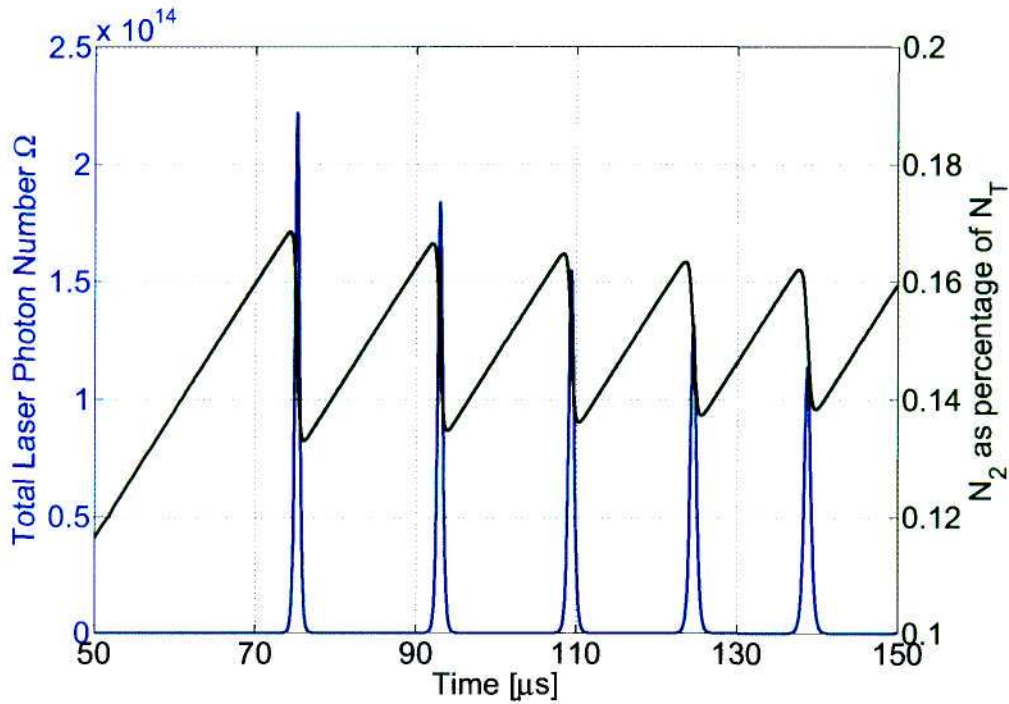


Figure 9.3: The total laser photon number (blue) and upper manifold population density (green) N_2 (as a percentage of the total doping N_T) of the Nd:YLF laser during the main relaxation oscillation spikes at full pump power (158 W).

Siegman describes a single relaxation oscillation pulse in the following way (Siegman, 1986):

As the laser is switched on initially, the number of laser photons in the resonator is roughly zero. When the population inversion exceeds the threshold inversion N_{TH} , the total gain in the resonator exceeds the total loss so that the number of laser photons start increasing exponentially. As the number of photons in the resonator reaches the steady-state oscillation level, the laser signal in the resonator is so strong that it depletes the atoms in the excited state quicker than the pump can provide them. At this point the population inversion starts to decrease, but since it is still above N_{TH} , the number of laser photons are still increasing. When the population inversion reaches N_{TH} , the total gain equals the total loss. At this point, the laser photon number reaches a maximum and then starts to decrease as the population inversion decreases even further. The nett loss in the resonator is now greater than the nett gain so that the photon number decreases sharply. When the photon number reaches the steady-state level, the the population inversion is at a minimum. From here the entire process repeats itself. The damping behaviour in the relaxation oscillation spikes are due to the fact that neither the photon number nor the population inversion decreases all the way to zero after each spike so that the initial conditions of each pulse are closer to the steady-state behaviour of the laser (Siegman, 1986).

The relaxation oscillation damping rate of a four-level laser is given by (Siegman, 1986)

$$\gamma_{RO} = \frac{P_P \gamma_2}{2P_{TH}} \quad (9.3)$$

where P_P is the incident pump power and P_{TH} is the incident threshold pump power, while $\gamma_2 = \frac{1}{\tau_2}$ is the upper manifold decay rate with τ_2 the upper manifold lifetime.

The decay rate of the relaxation oscillations that are produced by the rate-equation model compares very well with the analytical theory. Figure 9.4 shows the relaxation oscillations of the Nd:YLF laser at 158 W incident pump power. An analytical expression for the decay of the relaxation oscillations is given by

$$D(t) = L_P(1 - e^{-\gamma_{RO}t}) + L_{max}(e^{-\gamma_{RO}t}) \quad (9.4)$$

where L_P is the steady-state laser output at an incident pump power of P W and L_{max} is the maximum power of the first relaxation oscillation pulse. The red curve in Figure 9.4 was produced by using $P_{TH} = 14$ W, which is roughly the average between the experimental and numerical values for the threshold.

The relaxation oscillation frequency can be expressed by (Siegman, 1986)

$$\omega_{RO} = \sqrt{\left(\frac{P_P}{P_{TH}} - 1\right) \gamma_2 \gamma_c} \quad (9.5)$$

where γ_c is the cavity photon decay rate.

The analytical equation 9.5 predicts a $\omega_{RO} = 2\pi \times 125$ kHz which corresponds to a period of $8 \mu\text{s}$ between pulses. Figure 9.5 shows relaxation oscillation pulses according to the rate-equation model at two different periods during the relaxation oscillation process. In the initial large amplitude region, the rate-equation predicts a period of $18 \mu\text{s}$ between pulses. The larger predicted value is not unusual since the experimentally measured period between pulses in the large amplitude region can be 2-3 times larger than the analytical value (Siegman, 1986). In the small amplitude region, the pulse period as determined by the rate-equation model is $8.1 \mu\text{s}$ which is in perfect agreement with the analytical value.

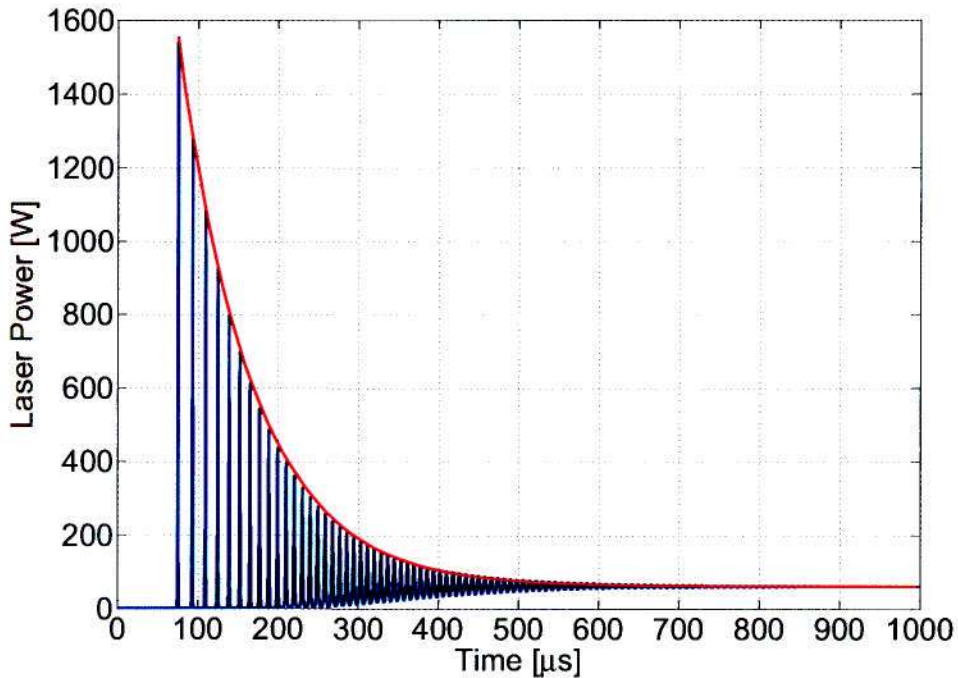


Figure 9.4: The relaxation oscillation spikes at full pump power (158 W). The blue curve is the rate-equation model solution while the red curve represents the analytical decay rate $D(t)$.

The relaxation oscillations that are produced by the single-element plane-wave rate-equation model exhibit pulses that have a decay rate, frequency and period that is consistent with analytically determined values.

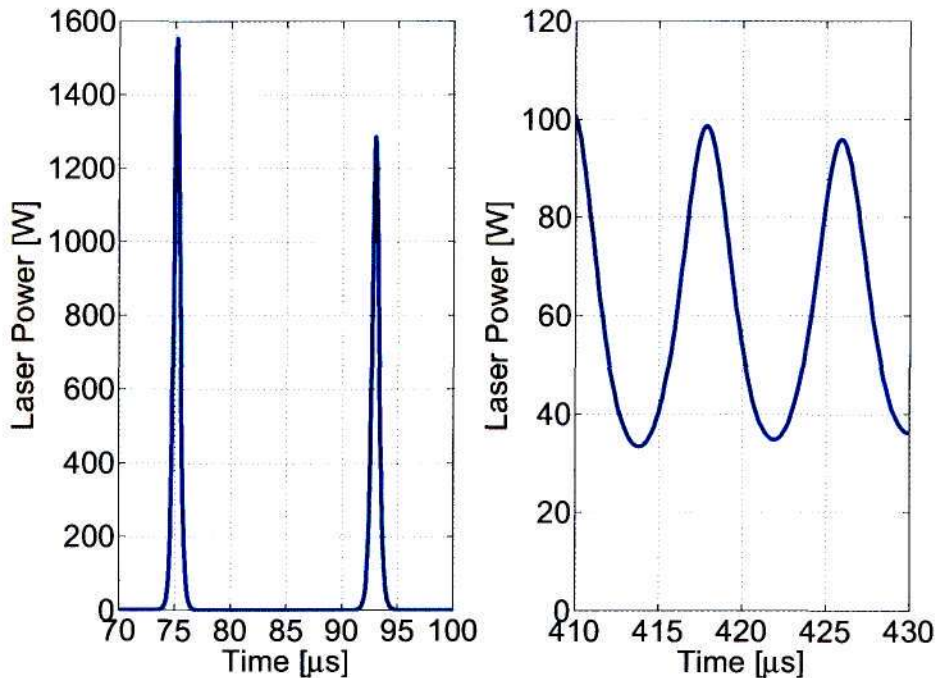


Figure 9.5: Relaxation oscillation pulses according to the rate-equation model at two different periods during the relaxation oscillation process. The figure on the left is during the initial large amplitude spikes while the figure on the right is during the small amplitude pulses.

9.2.3 Output Coupler Transmission

A great feature of the rate-equation model is the ability to optimise the laser's performance by determining the optimum parameter values. Some of the parameters that can be investigated and optimised include the output coupler transmission, crystal length and pump size.

Per illustration, the influence of the output coupler transmission on the laser output power is investigated. All the laser parameters in the rate-equation model are fixed while the output coupler transmission at the laser wavelength is varied. By making use of equations 9.1 & 9.2, the laser output power as a function of output coupler transmission can also be investigated analytically. Both the rate-equation and analytical solutions are shown in Figure 9.6.

From Figure 9.6 it is clear that the rate-equation provides a much better fit to the experimental data point than the analytical solution. The rate-equation model predicts

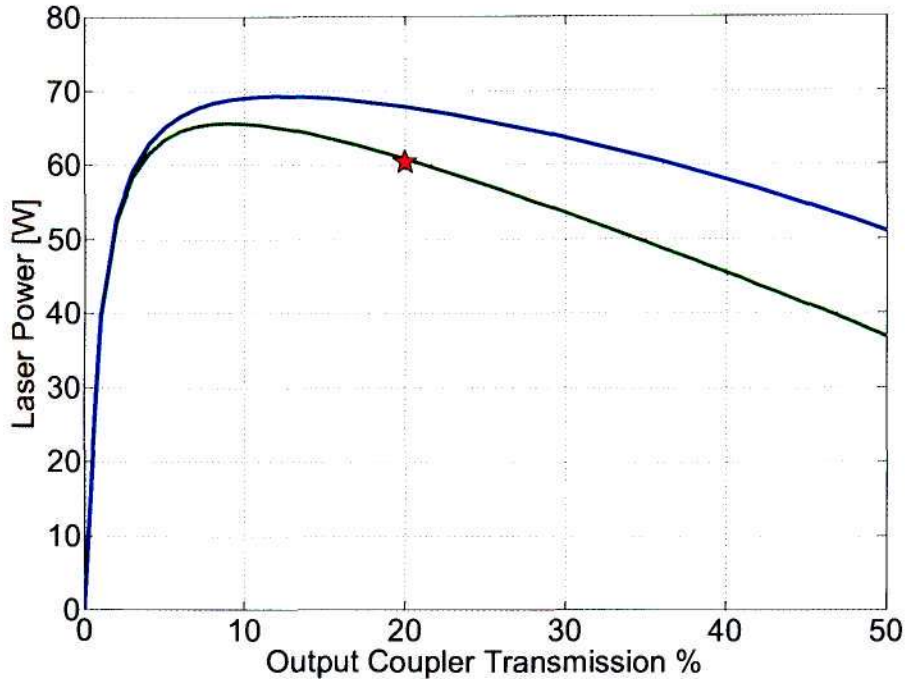


Figure 9.6: The laser power as a function of output coupler transmission. (Rate-equation: green and Analytical: blue) The red star indicates the point where the laser operated at.

the maximum laser power of 65 W at $\sim 10\%$ output coupler transmission at the laser wavelength. Since there is a relatively small difference between the laser output with a 10% and 20% transmission output coupler respectively, the laser was built with a 20% transmission output coupler in order to reduce the power in the resonator, which minimises the risk of damaging any of the optics.

9.3 Q-Switched Operation

In addition to the modelling of the CW operation of the laser, the single-element plane-wave rate-equation model can also be used to simulate a Q-switched laser.

The main difference between the CW and Q-switched lasers is an additional modulated loss that is introduced in the case of the Q-switched laser due to the Acousto-Optic-Modulator (AOM). In the rate-equation model the loss of the AOM is assumed to be modulated between 0% and 100%. In reality, the maximum loss of this particular

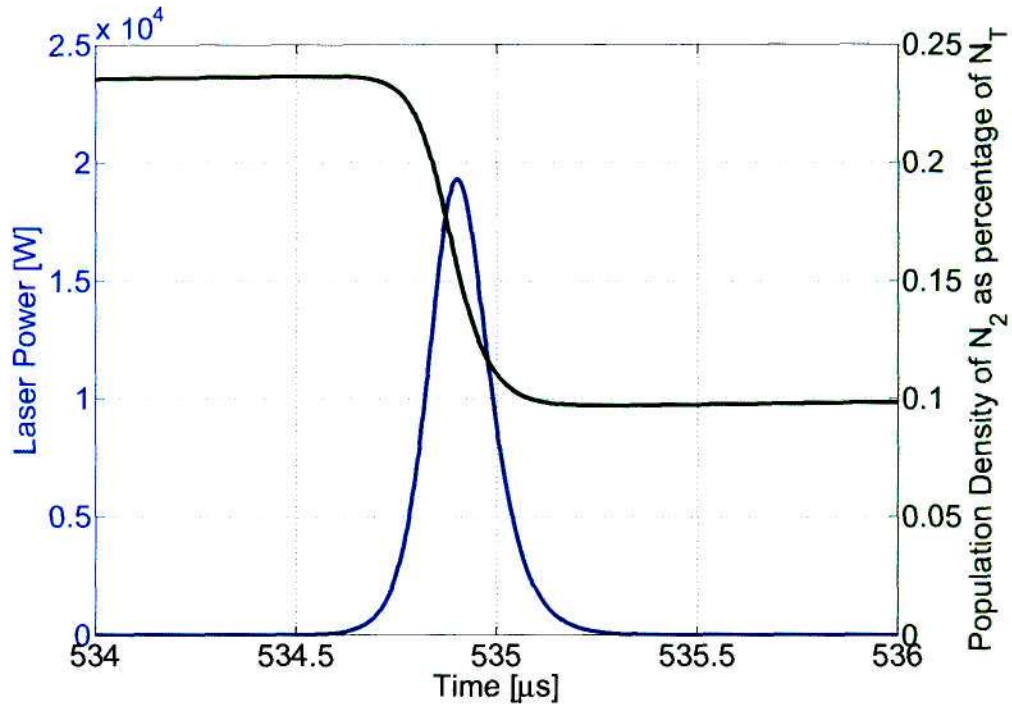


Figure 9.8: A single Q-switched pulse (blue) along with the population density of N_2 (green) according to the rate-equation model.

As the Q-switch is switched on, the loss in the resonator is very high (loss \rightarrow 100% in the case of the rate-equation model). Due to the loss in the resonator that is higher than the gain, the population inversion will keep on increasing without any laser action in this period so that energy is stored in the gain medium. As soon as the AOM is switched off, the loss in the resonator is small. At this point the gain is much higher than the loss in the resonator. The high gain will initiate the lasing action, which depletes the population inversion via stimulated emission. When the population inversion is depleted so that it reaches the threshold value, the laser power is at a maximum. There are still a lot of laser photons in the resonator at this point, so that they reduce the population inversion to below the threshold value via stimulated emission. From here the pump needs to replenish the population inversion again. Before the pump absorption causes the population inversion to reach the threshold value, the AOM is switched on again so that the loss is very high so that the laser can not lase.

The single-element plane-wave rate-equation model predicts Q-switched pulses with a width of 175 ns (FWHM) while a Q-switch pulse width of 143 ns was measured. Figure 9.9 shows a modelled Q-switched pulse in comparison with an oscilloscope trace

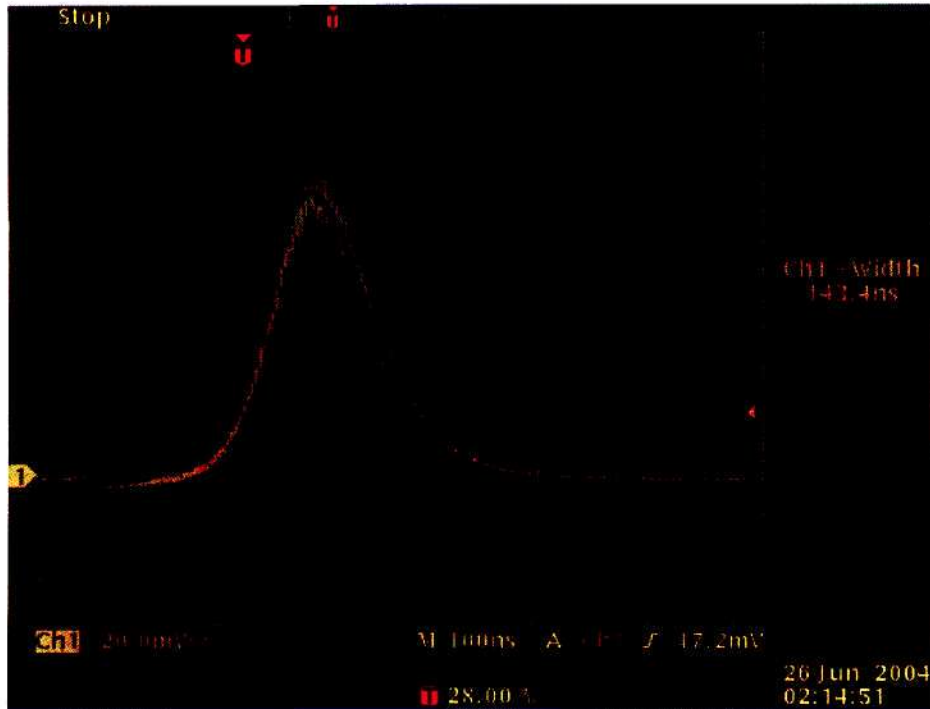


Figure 9.9: An oscilloscope trace of a single pulse (yellow) along with a pulse as produced by the rate-equation model (blue). The measured pulse FWHM is 143 ns while the rate-equation model predicts the pulse FWHM to be 175 ns.

of a pulse. The high-frequency oscillations on the oscilloscope pulse are due to mode-beating between various longitudinal modes. This effect is not considered in the rate-equation model.

The rate-equation model manages to reproduce the pulse train as can be seen in Figure 9.10. The pulse train was simulated by using an AOM repetition frequency of 15 kHz with an off-time of $3 \mu\text{s}$ at an incident pump power of 158 W.

The initial couple of pulses in the pulse train are unstable but then stabilises very soon (after 5 pulses) to deliver stable pulses with a peak power of 19.1 kW. After the pulses stabilise, they have an average power of 57.3 W and an energy of 3.8 mJ per pulse.

The population density of the upper manifold N_2 that produces the pulse train in Figure 9.10 is shown in Figure 9.11. The population density of N_2 increases to $\sim 0.24\%$ of N_T just before a Q-switch pulse. After a pulse, the population density of N_2 is decreased all the way to $\sim 0.1\%$ of N_T which is less than the threshold inversion of $\sim 0.15\%$ of N_T .

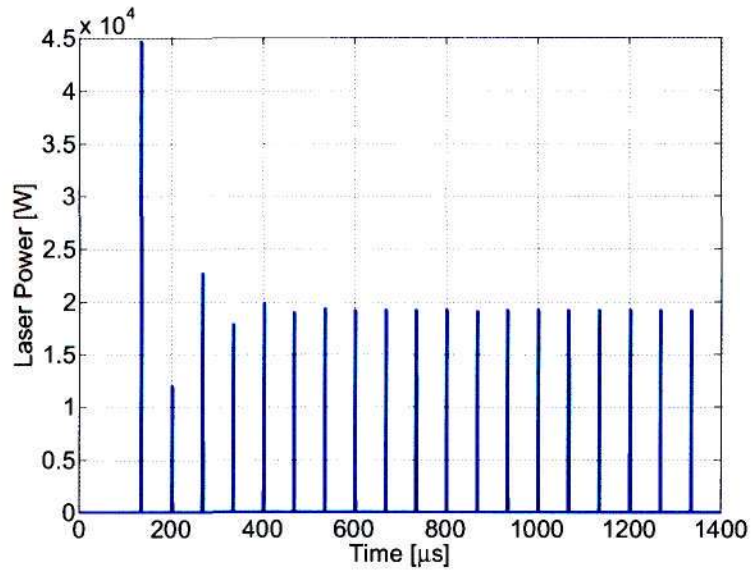


Figure 9.10: The pulse train during Q-switch operation as produced by the rate-equation model.

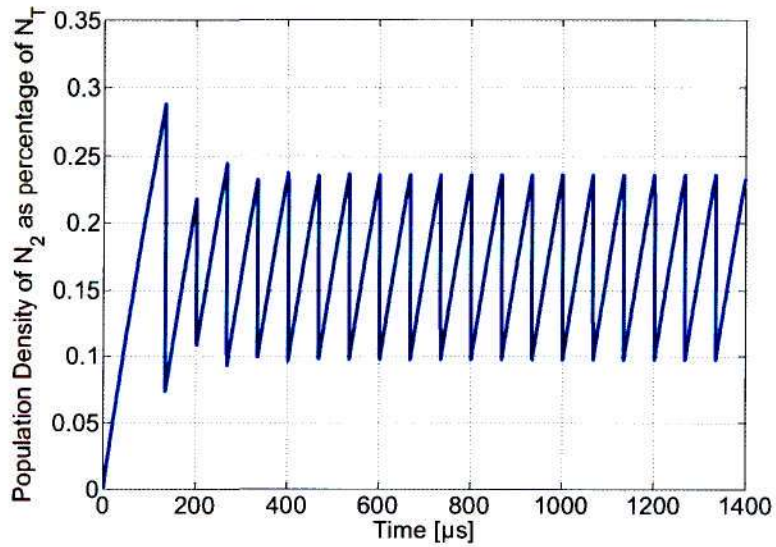


Figure 9.11: The population density of N_2 during Q-switch operation as delivered by the rate-equation model.

9.3.2 Average Power and Pulse Energy

The rate-equation model was used to determine the average power and pulse energy of the laser as a function of pulse repetition frequency (Figure 9.12). An average power of 52 W was achieved at 5 kHz, which increased to a value of 59.1 W at 30 kHz. As expected, the average power converges to the CW power of 60.3 W at high pulse repetition rates. The pulse energy decreased from 10.4 mJ at a repetition rate of 5 kHz to 2 mJ at 30 kHz. The rate-equation provides a very good fit to the experimental data for both the average power and the energy per pulse. Unfortunately, one of the two Nd:YLF crystals fractured at 5 kHz while taking the measurements, so that the experiment could not be continued to even lower repetition rates.

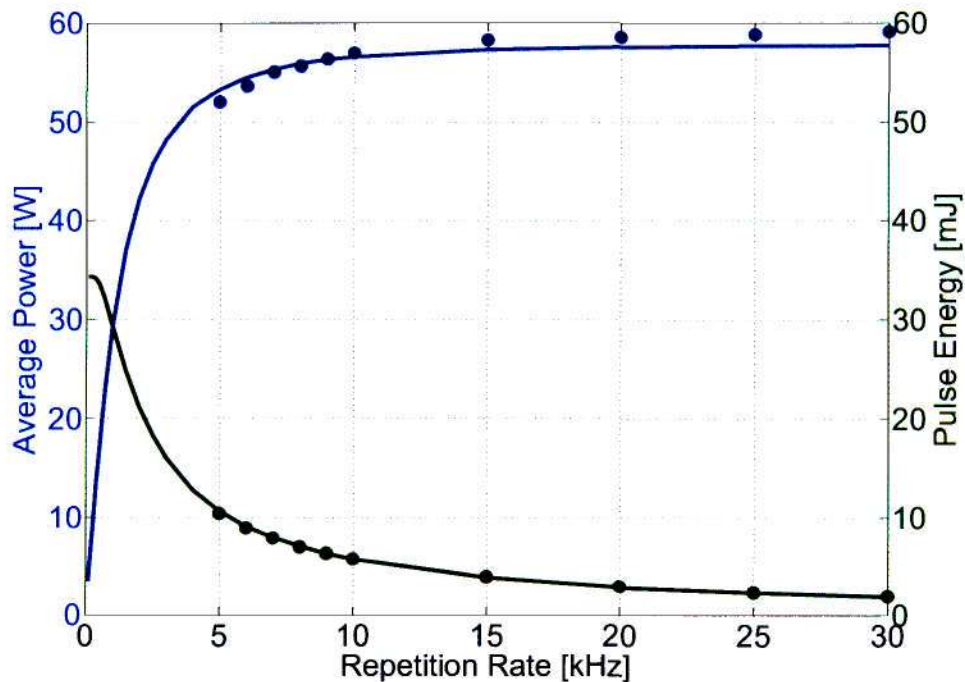


Figure 9.12: The average power (blue) and pulse energy (green) of the laser as a function of pulse repetition frequency. The solid curves represent the rate-equation solutions while the dots are experimental data.

9.4 Summary

The single-element plane-wave rate-equation model was applied to a four-level Nd:YLF laser to predict its behaviour during CW and Q-switched operation.

The rate-equation model predicts a threshold power and slope efficiency for the CW laser that compares very well with experimental data. The relaxation oscillations were investigated and their behaviour was found to be in very good agreement with analytical solutions. The laser power as a function of output coupler transmission was compared with experimental data and analytical solutions where a good agreement with experimental data was found.

During Q-switched operation, the pulse train with its corresponding population inversion was produced accurately by the rate-equation model. The pulse width and peak power is consistent with experimental data. Even though the example that was presented in this chapter was at a pulse repetition rate of 15 kHz, the rate-equation model predicted the laser operation accurately for other pulse repetition rates as well. The rate-equation produces the average power and pulse energy as a function of pulse repetition rate that agrees extremely well with measured data.

The single-element plane-wave quasi-three-level rate-equation model manages to simulate and predict the behaviour of a four-level Nd:YLF laser during CW and Q-switched operation accurately.

Chapter 10

Tm:GdVO₄ Laser

In this chapter, the single-element plane-wave rate-equation model that has been developed in Chapter 8, is applied to quasi-three-level Tm:GdVO₄ laser (Esser *et al.*, 2007) (Esser *et al.*, 2008). A major advantage of using the Tm:GdVO₄ is that it has a strong and broad absorption spectrum centered at 799 nm, which makes it perfect to be pumped with commercially available high power laser diodes (Esser *et al.*, 2007). The population dynamics of the active ion, Thulium (Tm), is more complicated than the Neodymium (Nd) of the laser in the previous chapter. Thulium exhibits an additional energy transfer processes between ions, known as cross-relaxation.

Cross-relaxation is the process where a Thulium ion which has been excited to the ³H₄ energy manifold, transfers energy to a neighbouring Thulium ion that is in the ³H₆ ground manifold (Rustad & Stenersen, 1996). This process increases the efficiency of the laser since a single absorbed pump photon can result in two Thulium ions in the ³F₄ upper laser manifold (Figure 10.1).

In the single-element plane-wave rate equation model, cross-relaxation is accounted for by using a pump efficiency that is larger than 1. With the correct doping concentration, the pump efficiency can approach a value of 2. As a comparison, note that Neodymium lasers have a pump efficiency of ~ 0.7 (Fan & Byer, 1988). A good agreement between the rate-equation model predictions and experimental data is found when a pump efficiency of 1.3 is used for the Tm:GdVO₄ laser. It should be mentioned that upconversion is neglected in the rate-equation model of the Tm:GdVO₄ laser.

The rate-equation model is implemented in MATLAB in the same way as described in the introductory paragraph of chapter 9. Where possible, analytical expressions are compared to the rate-equation solutions. The rate-equation model parameters as well as additional information of the laser are noted in Appendix B.

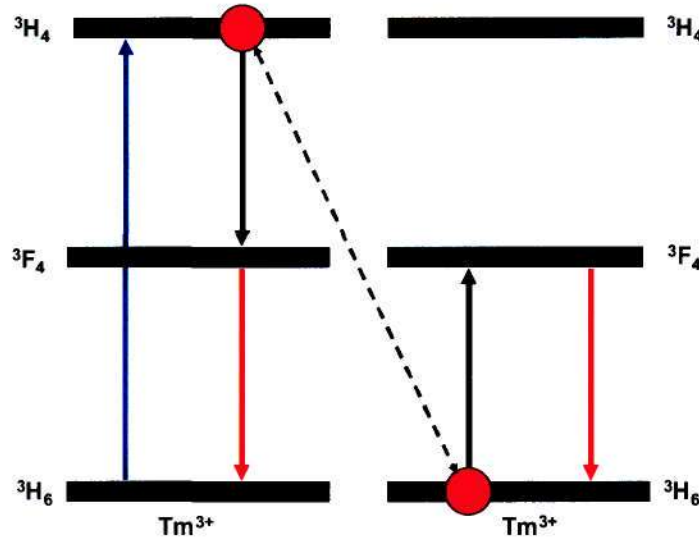


Figure 10.1: The cross-relaxation process in Tm³⁺. The blue arrow indicates the pump process, the black arrows the cross-relaxation process while the red arrows indicate the stimulated laser emission.

10.1 Experimental Setup

The experimental setup of the laser is shown in Figure 10.2. The Tm:GdVO₄ crystal was pumped with a quasi-CW (QCW) fibre-coupled diode. The power supply that was connected to the laser diode pump was modulated by a pulse generator so that QCW pulses could be delivered by the diode pump. The pump light exiting the fibre was collimated and then focused into the crystal to a radius of 220 μm . The diode pump was capable of delivering a maximum of 75 W at 803 nm. The optical fibre had a core diameter of 0.4 mm and a numerical aperture of 0.22. The resonator was designed with a length of 26 mm. This length was adjusted slightly to compensate for the thermal lens in the crystal. An output coupler with a 5% transmission at the laser wavelength of 1915 nm was chosen.

10.2 QCW Operation

The Tm:GdVO₄ crystal was pumped with a QCW beam in order to reduce the average pump power in the crystal to limit thermally induced stresses which ultimately cause crystal fracture. The QCW pump was set to an on-time of 20 ms at 5 Hz to provide an overall duty cycle of 10%.

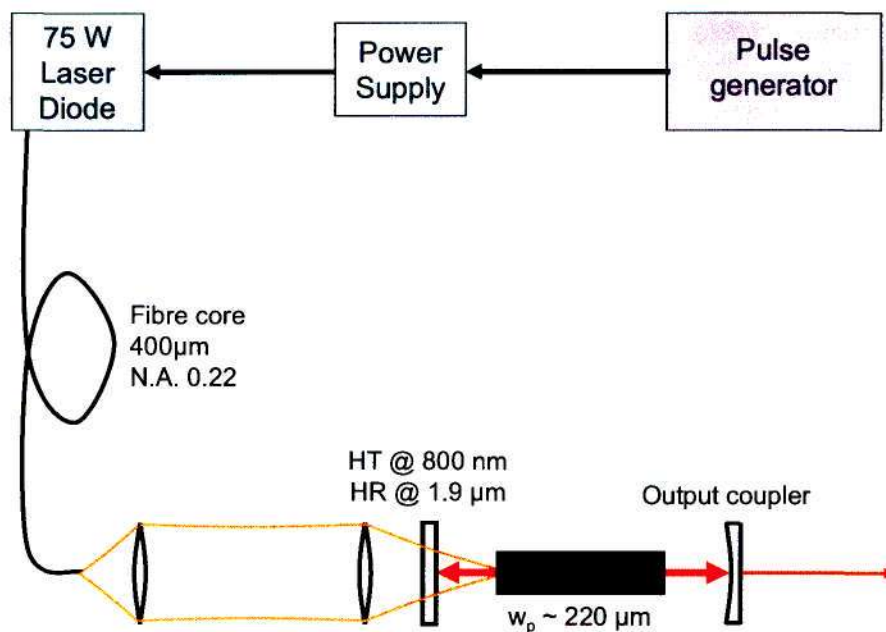


Figure 10.2: The experimental setup of the Tm:GdVO₄ laser (Esser *et al.*, 2008).

10.2.1 Threshold and Efficiency

Note that in this section, any reference to pump power or laser power refers to the peak value during a QCW pump pulse.

An analytical expression for the laser threshold with respect to the absorbed pump power of a quasi-three-level laser is given by (Fan & Byer, 1987)

$$P_{TH} = \frac{h\nu_P}{4l_P\sigma_L^{em}\tau} (A_P + A_L)(T + L + 2N_0\sigma_L^{abs}l) \quad (10.1)$$

This expression is the same as the analytical threshold of a four-level laser (equation 9.1) except for the last term. This term accounts for the reabsorption loss that occurs in quasi-three-level lasers due to the lower laser level that is thermally populated. N_0 is the concentration of active ions in the medium, σ_L^{abs} is the effective absorption cross-section at the laser wavelength and l is the length of the crystal.

By making use of equation 10.1, it is possible to determine the laser threshold as a function of laser wavelength since the effective absorption- and emission cross sections are functions of wavelength. The laser will operate at the wavelength for which the

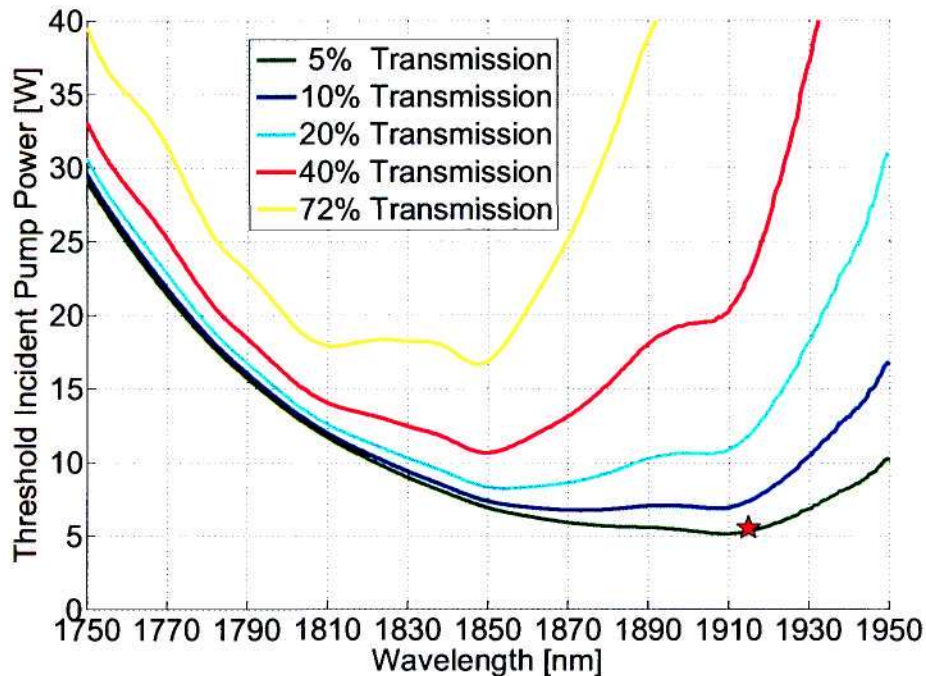


Figure 10.3: The laser threshold as a function of wavelength (sigma polarization) for various output couplers. The red star indicates the point at which the laser operated with a 5% transmission output coupler.

threshold is a minimum. Figure 10.3 shows the threshold of the laser as a function of wavelength for various output couplers.

The analytical approach predicts that the laser will operate at a wavelength of 1910 nm with a threshold of 6 W incident pump power. It is very close to the experimental measured values of a laser wavelength at 1915 nm with a threshold of 5.6 W. The rate-equation model predicts a threshold of 5.5 W which is even closer to the experimental value than the analytical expression.

The measured slope efficiency for the laser was 28.4%, while the rate-equation model predicts 32% (Figure 10.4). The rate-equation fits the experimental data very well up to about 20 W incident pump power. At larger pump powers, a decrease in the laser's slope efficiency was observed experimentally. It is very likely that the decrease in the slope efficiency at higher pump powers is due to the very strong thermal lens that is induced in Tm:GdVO₄. Since the rate-equation model doesn't include any thermal effects such as thermal lensing, it is not able to predict the decrease in slope efficiency. The YLF laser in the previous chapter, has a negative thermal lens due to the negative

temperature dependence of the refractive index of YLF. The negative thermal lens is then compensated for by the positive lens formed by the bulging effect on the pumped face of the crystal. This results in an overall weak thermal lens. In contrast, the refractive index of GdVO₄ has a positive temperature dependence which induces a positive thermal lens so that the thermal lens contribution of the bulging effect just adds to the overall strength of the thermal lens. From equation 2.29, it is estimated that the focal length of the thermal lens (due to the temperature profile in the GdVO₄ crystal) can be as strong as 20 mm at an incident power of 37 W. Thus, the thermal lens varies from very weak (at the start of a QCW pump pulse) to extremely strong during a single QCW pump pulse. Since it is very difficult to design a resonator that is stable for such a highly variable thermal lens, it is possible that the overlap between the pump and laser modes at high pump power is not so good as at lower pump powers. This would cause a decrease in the slope efficiency at high pump powers. It should be noted that thermal fracture of the Tm:GdVO₄ crystal was observed at an incident pump power of 37.3 W.

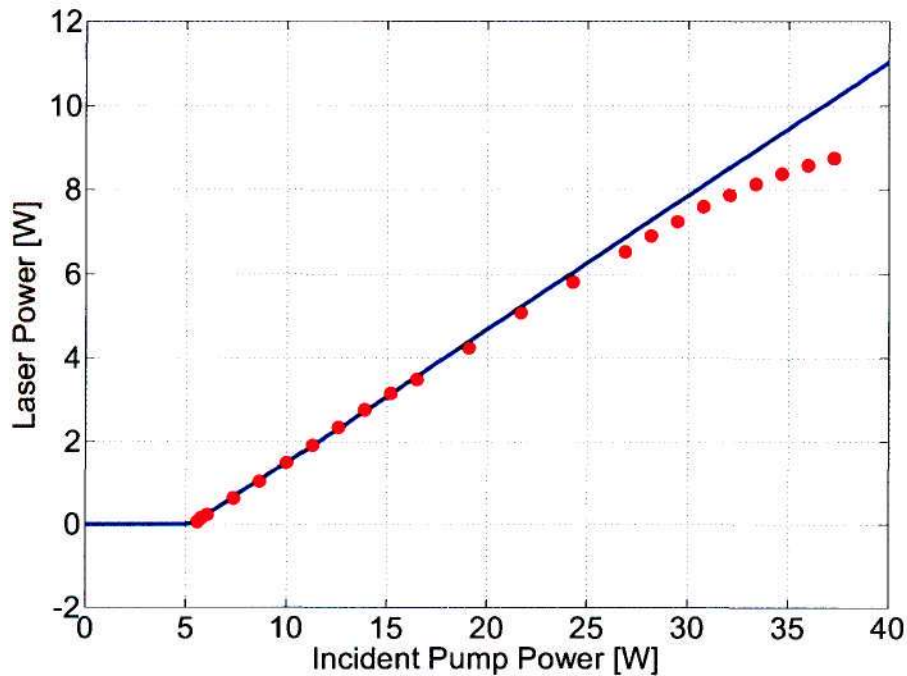


Figure 10.4: Power scaling of the Tm:GdVO₄ laser. The blue line represents the rate-equation solution and the red dots the experimental values.

10.2.2 Relaxation Oscillations

The rate-equation model was also implemented to investigate the relaxation oscillations during each QCW pump pulse. At full pump power (37.3 W), the relaxation oscillation spikes reach a maximum power of 220 W from where the spikes decay to a CW power of 10 W. Figure 10.5 shows the relaxation oscillations for the laser at full pump power. Even at pump powers just above threshold, the relaxation oscillations have already stabilised to a constant laser output within the QCW pulse duration of 20 ms.

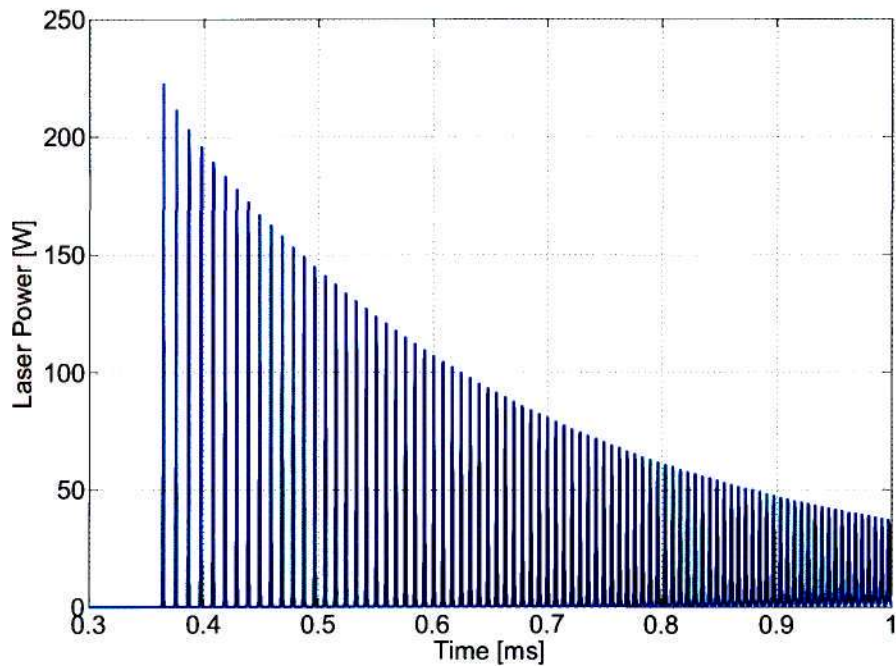


Figure 10.5: The relaxation oscillations of the Tm:GdVO₄ laser at an incident pump power of 37.3 W.

As expected, the upper laser manifold population density for the quasi-three-level laser is higher than the four-level laser of the previous chapter. For the four-level Nd:YLF laser, the upper laser manifold population as a percentage of the total ion density was $N_2/N_T = 0.15\%$. For the quasi-three-level Tm:GdVO₄ laser the upper laser manifold population density as a percentage of the total ion density converges to $N_2/N_T = 21.55\%$. The higher upper laser manifold population density for the quasi-three-level laser is required to overcome the thermally populated lower laser manifold. This means that a higher upper laser manifold population density is required in order

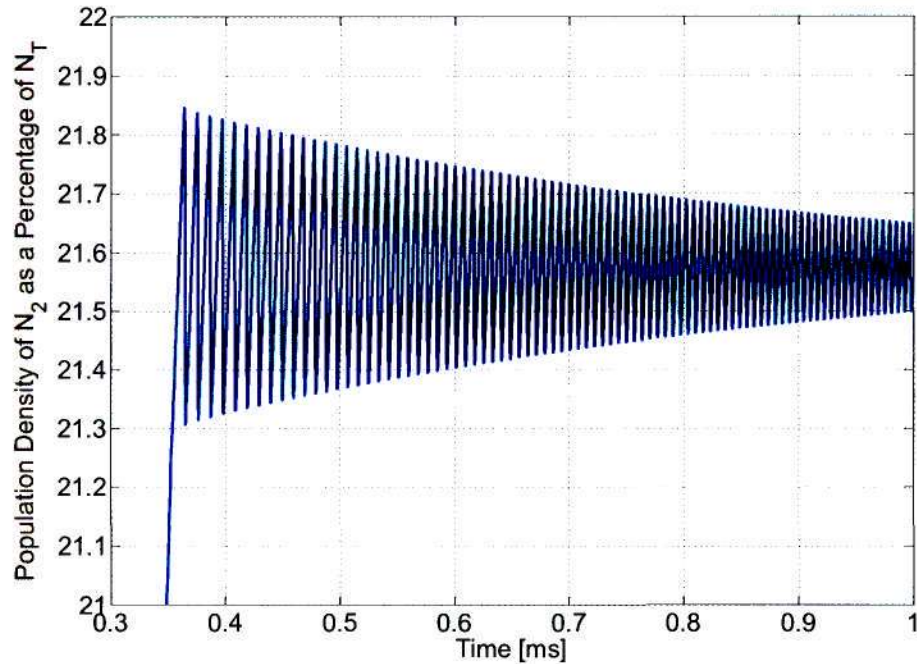


Figure 10.6: The population inversion density during the relaxation oscillations of the Tm:GdVO₄ laser at an incident pump power of 37.3 W.

to reach threshold. Figure 10.6 shows the upper laser manifold population density during the relaxation oscillations of the Tm:GdVO₄ laser at an incident pump power of 37.3 W.

10.2.3 Output Coupler Transmission

A change in the output coupler transmission will influence the threshold and cause a shift in the laser wavelength (Figure 10.7). As the output coupler transmission is increased, the laser wavelength changes from 1915 nm (sigma-polarization) at an output coupler transmission of 5% to 1850 nm at an output coupler transmission of 25%. Between an output coupler transmission of 25% and 50%, the laser wavelength is unchanged. It should be noted that an output coupler transmission of 72% resulted in a change in the polarization of the laser light. This is because the pi-polarization results in a lower threshold at this particular output coupler and wavelength (1818 nm).

As the laser wavelength is changed, the effective emission and absorption cross-sections also change (equation 10.1). When the changing laser wavelength (as a func-

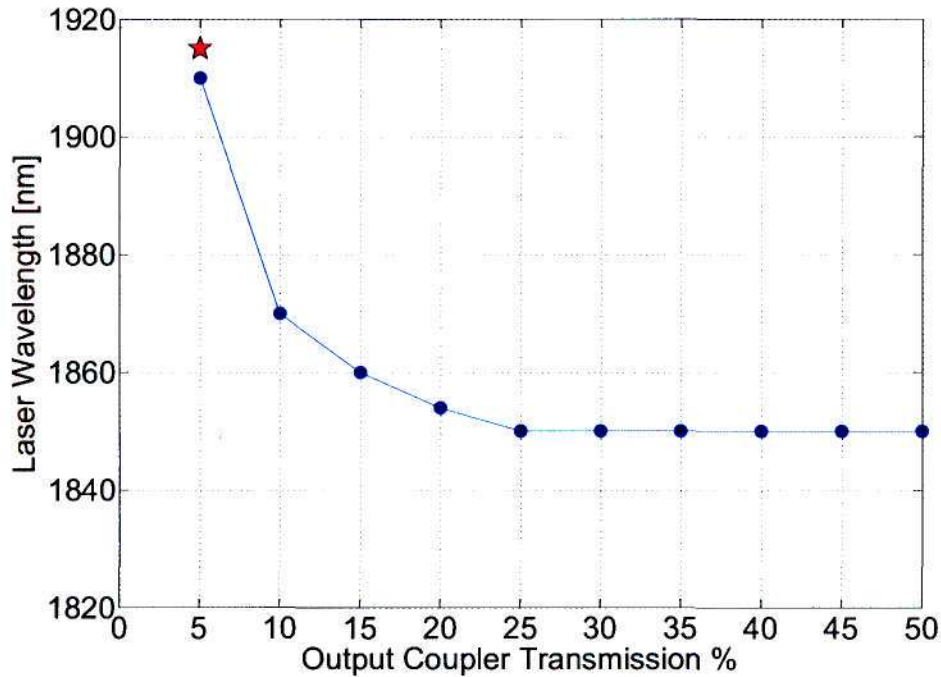


Figure 10.7: The Tm:GdVO₄ laser wavelength as a function of output coupler transmission. The red star represents the point at which the laser operated.

tion of output coupler transmission) and the corresponding change in effective cross sections are ignored, the rate-equation model predicts the optimum laser output power at an output coupler transmission of 10% (Figure 10.8). If the change in the laser wavelength and effective cross sections are taken into account, the optimum output coupler transmission is estimated to be 15%. Although there is not a big difference in the optimum output coupler transmission as predicted by the two models, the difference in the slope of the two curves is significant.

In the rate-equation prediction (solid blue curve) in Figure 10.8, the effective cross-sections (sigma-polarization) at 1915 nm were used to predict the laser output at all output coupler transmissions. The blue dots in Figure 10.8 show the the rate-equation solution with the effective cross sections adapted for the shifted laser wavelength. From Figure 10.8 it is evident that it is necessary to account for the change in laser wavelength and thus the effective absorption and emission cross sections in order to predict the laser power as a function of output coupler transmission.

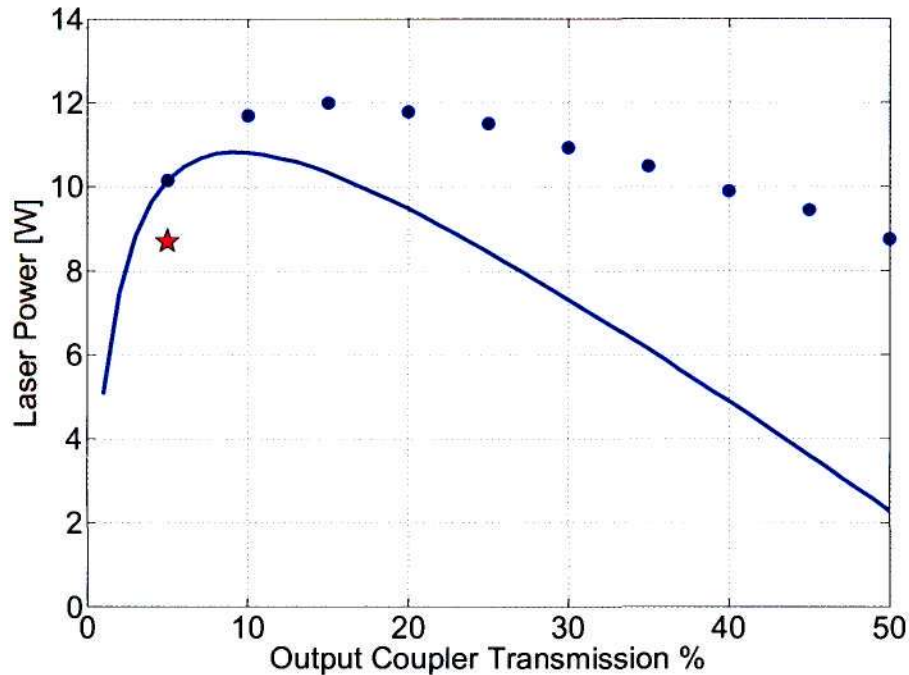


Figure 10.8: The output power of the Tm:GdVO₄ laser (at an incident pump power of 37.3 W) as a function of the output coupler transmission. The red star indicates the point at which the laser operated. The solid blue line shows the rate-equation solution (constant effective cross sections) and the blue dots show the rate-equation solution with the effective cross sections adapted for the shifted laser wavelength.

10.3 Summary

The quasi-three-level single-element plane-wave rate-equation model has been applied to a quasi-three-level Tm:GdVO₄ laser. The rate-equation model managed to predict the threshold of the laser accurately. An analytical expression for the laser threshold was used as a further confirmation. The analytical expression also predicts the wavelength at which the laser will operate for a given output coupler transmission. The wavelength prediction of 1910 nm at a 5% output coupler transmission is very close to the observed wavelength of 1915 nm.

The rate-equation model predicts the laser output accurately up to pump powers of ~ 20 W. At higher pump powers, a decrease in the slope efficiency of the laser was observed. This is due to the highly variable thermal lens in the crystal that influences the overlap between the pump and laser modes and reduces the efficiency of the laser.

Since the rate-equation model doesn't account for a thermal lens, the decrease in the slope efficiency of the laser is not predicted.

The relaxation oscillations and the corresponding population dynamics were investigated with the rate-equation model. As expected, the population inversion density for the quasi-three-level Tm:GdVO₄ laser is much higher than that of the four-level Nd:YLF laser in the previous chapter. The higher population inversion that is required for the quasi-three-level laser is to overcome the reabsorption loss due to the lower laser level that is thermally populated.

The laser power as a function of output coupler transmission was investigated. For the rate-equation model to accurately predict the laser power as a function of output coupler transmission, the changing laser wavelength and the corresponding change in effective absorption and emission cross sections should be taken into consideration.

Part IV

Conclusion and Summary

Conclusion and Summary

The first part of this thesis is mainly an introduction to diode-pumped solid-state lasers. The basic operation principles of diode-pumped solid-state lasers are explained. The interaction processes between electromagnetic radiation and matter are discussed. Solid-state gain media, end- and side-pump geometries as well as basic resonators are among the other topics that were considered.

The second part consists of a detailed discussion of the thermal effects in solid-state lasers. The temperature distribution in a pumped laser rod was determined by solving the heat diffusion equation. Analytical solutions for isotropic cylindrical laser rods were discussed, while finite element methods were employed in order to determine the temperature distribution in more complex anisotropic materials of various geometries. The effects and the theory surrounding temperature induced thermal lensing and thermally induced stresses were discussed. Analytical solutions for the thermal lens and thermally induced stresses were investigated for isotropic cylindrical laser rods. After all the theory surrounding thermal effects were explained, the temperature distribution, thermal lens and thermal stresses were determined for a CW pumped Nd:YAG rod. The analytical expressions and numerical solutions for the thermal effects were found to be consistent with experimental data. Next, the analytical expression that predicts the maximum stress in isotropic cylindrical rods was extended to predict the maximum stress in isotropic slabs. A good agreement with numerical models was found if the ratio of the pump beam diameter to the slab width was greater than 0.7. A coupled-thermal stress finite element analysis of an anisotropic QCW-pumped Tm:YLF rod was performed in the commercially available software package, ABAQUS. The goal was to investigate the time-dependent thermal stresses in order to determine the average pump power at which crystal fracture occurs as a function of the QCW pump duty cycle. The final chapter in this section consists of a summary of a time-dependent analytical thermal model for end-pumped isotropic laser rods that was developed after the completion of this dissertation..

In the final part of this thesis, a single-element plane-wave quasi-three-level rate-equation model was developed. The section started off with a detailed discussion of idealised three- and four-level rate-equation models. This was followed by the discussion and development of a spatially resolved quasi-three-level rate-equation model.

CONCLUSION AND SUMMARY

However, in order to simplify the implementation of the rate-equation model as a computer simulation, the spatial dependence of the parameters was ignored by reducing the model to a single-element plane-wave quasi-three-level rate-equation model. The model was then applied to a four-level Nd:YLF laser as well as a quasi-three-level Tm:GdVO₄ laser. For both lasers, the rate-equation model predicted a threshold and slope efficiency that was consistent with experimental data. Population inversion, relaxation oscillations and the effect of the output coupler transmission on the laser behaviour, were some of the other dynamics that were predicted successfully by the rate-equation model. Where possible, analytical expressions were also implemented to explain and predict the behaviour of some laser parameters such as the laser wavelength. Overall, the single-element plane-wave rate-equation model managed to provide quick and accurate explanations for the laser dynamics during CW, Q-switch and QCW laser operation.

The work that is presented in this thesis illustrates the successful development and implementation of numerical and analytical thermal models which explain and predict the thermal effects in diode-pumped solid-state lasers as well as a quasi-three-level rate-equation model that explains the population dynamics of such a laser.

Future work will include the development of an analytical time-dependent model that determines the temperature distribution in the laser rod for an arbitrary pump profile. This will enable an analytical time-dependent analysis of the thermal lens and thermally induced stresses in laser rods of QCW-pumped lasers. The next step in the rate-equation model will be to extend the model to account for the spatial dependence of parameters. Additional effects such as upconversion and cross-relaxation will also be included. There is a complex interplay of parameters between the thermal and rate-equation models so that ultimately, the thermal and rate-equation models should be merged into one comprehensive laser model.

Appendix A

Nd:YLF Laser Model - Additional Information

This Appendix consists of additional information about the Nd:YLF laser that is described in chapter 9.

Table A.1: The parameters of the Nd:YLF laser that were used in the rate-equation model.

Parameter	Value	Reference
Doping at. %	0.5	(Bollig <i>et al.</i> , 2008)
Nd:YLF Refractive Index (1050 nm)	1.46	(Barnes & Gettemy, 1980)
Crystal length [mm]	80	(Bollig <i>et al.</i> , 2008)
Effective absorption cross-section [cm ²]	2.35e-20	(Cross, 2004)
Effective emission cross-section [cm ²]	14e-20	(Czeranowsky, 2002)
Upper level lifetime [μ s]	525	(Ryan & Beach, 1992)
Pump Efficiency	0.7	(Fan & Byer, 1988)
Density of active ions in 1% doping [cm ³]	1.4e20	(VLOC Catalog, 2008)
Pump Wavelength [nm]	805	(Bollig <i>et al.</i> , 2008)
Pump beam diameter [mm]	2	(Bollig <i>et al.</i> , 2008)
Laser Wavelength [nm]	1053	(Bollig <i>et al.</i> , 2008)
Resonator length [mm]	773	(Bollig <i>et al.</i> , 2008)
Output Coupler Transmission % at 1053 nm	20	(Bollig <i>et al.</i> , 2008)
Other Losses %	1	(Bollig <i>et al.</i> , 2008)

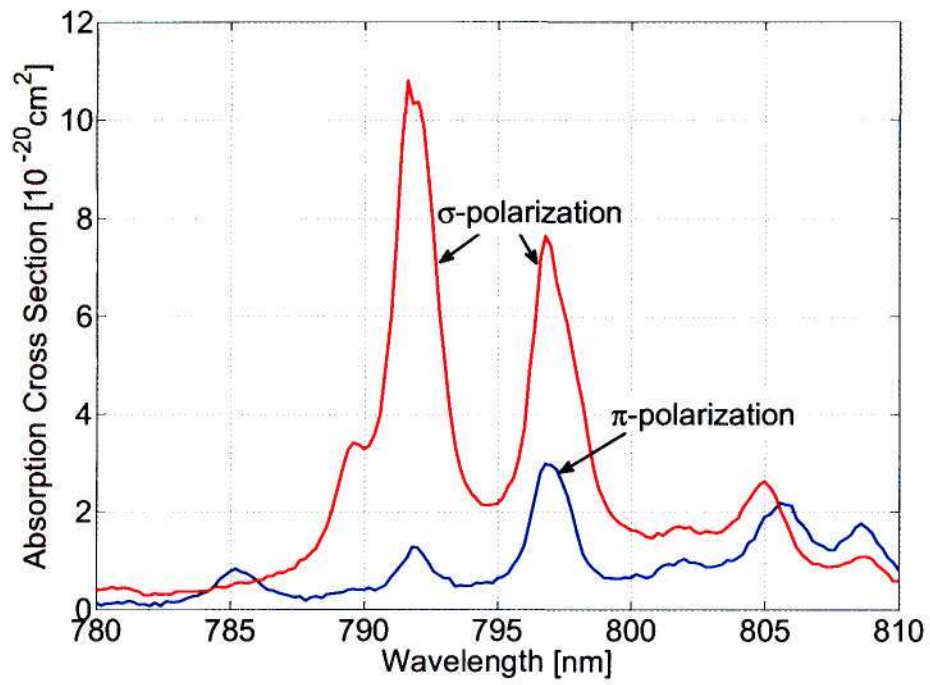


Figure A.1: The effective absorption cross-sections of Nd:YLF on the sigma (red) and the pi (blue) polarizations (Cross, 2004).

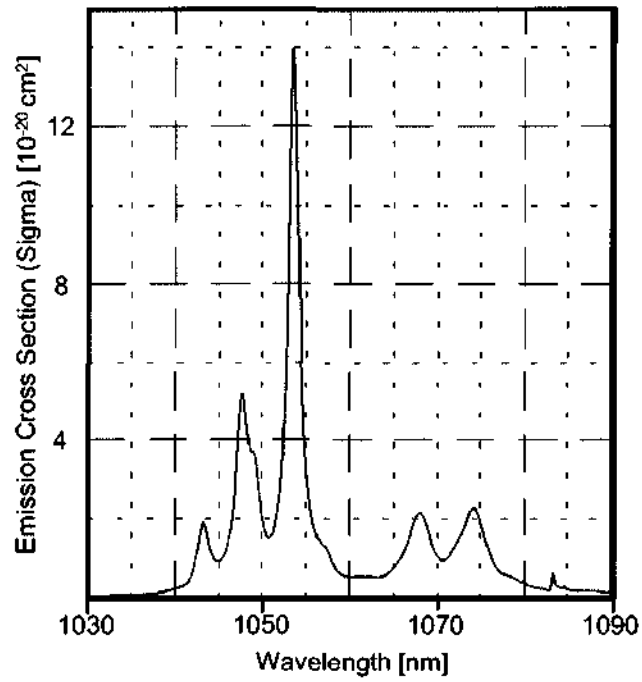


Figure A.2: The effective emission cross-sections (sigma-polarization) of Nd:YLF (Czeranowsky, 2002).

Appendix B

Tm:GdVO₄ Laser Model - Additional Information

This Appendix consists of additional information about the Tm:GdVO₄ laser that is described in chapter 10.

Table B.1: The parameters of the Tm:GdVO₄ laser that were used in the rate-equation model.

Parameter	Value	Reference
Doping at. %	3	(Esser <i>et al.</i> , 2008)
Tm:GdVO ₄ Refractive Index (1064 nm)	1.9	(Zagumennyi <i>et al.</i> , 2003)
Crystal length [mm]	3	(Esser <i>et al.</i> , 2008)
Effective absorption cross-section at λ_P [cm ²]	1.6e-20	(Esser <i>et al.</i> , 2008)
Effective emission cross-section at λ_P [cm ²]	2.6e-20	(Esser <i>et al.</i> , 2008)
Effective absorption cross-section at λ_L [cm ²]	0.02e-20	(Esser <i>et al.</i> , 2008)
Effective emission cross-section [at λ_L cm ²]	0.22e-20	(Esser <i>et al.</i> , 2008)
Upper level lifetime [ms]	1.85	(Lisiecki <i>et al.</i> , 2006)
Pump Efficiency	1.3	Estimated
Density of active ions in 1% doping [cm ³]	1.25e20	(Zagumennyi <i>et al.</i> , 2003)
Pump Wavelength [nm]	803	(Esser <i>et al.</i> , 2008)
Pump beam diameter [μ m]	440	(Esser <i>et al.</i> , 2008)
Laser Wavelength [nm]	1915	(Esser <i>et al.</i> , 2008)
Resonator length [mm]	26	(Esser <i>et al.</i> , 2008)
Output Coupler Transmission % at 1915 nm	5	(Esser <i>et al.</i> , 2008)
Other Losses %	2	(Esser <i>et al.</i> , 2008)

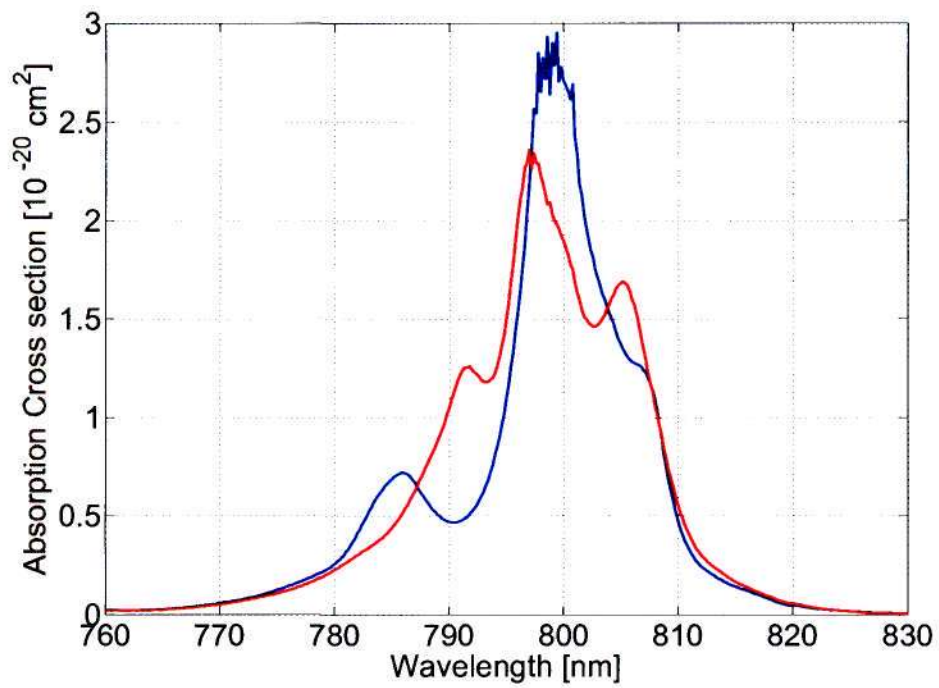


Figure B.1: The effective absorption cross-sections of Tm:GdVO₄ on the sigma (red) and the pi (blue) polarizations (Esser *et al.*, 2008).

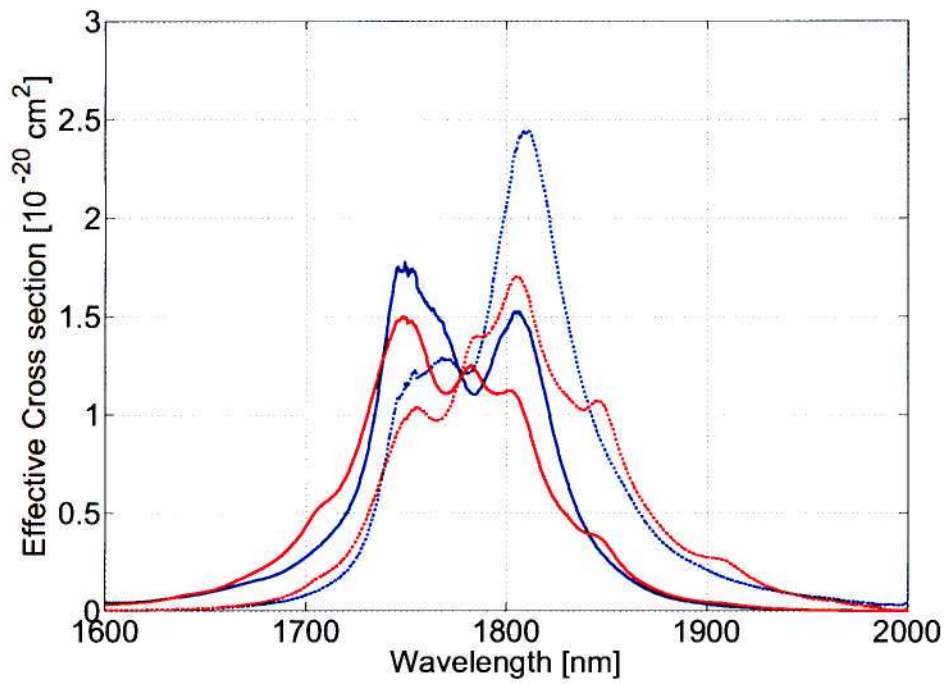


Figure B.2: The effective absorption (solid curves) and emission (dashed curves) cross-sections on the sigma (red) and pi (blue) polarizations of Tm:GdVO₄ (Esser *et al.*, 2008).

List of Publications

Peer-Reviewed Journal Papers

1. **E.H. Bernhardt**, A. Forbes, C. Bollig and M.J.D. Esser, Estimation of thermal fracture limits in quasi-continuous-wave end-pumped lasers through a time-dependent analytical model, *Optics Express*, 16, 11115-11123, July, 2008
2. **E.H. Bernhardt**, C. Bollig, M.J.D. Esser, A. Forbes, L.R. Botha and C. Jacobs, A Single-Element Plane-Wave Solid-State Laser Rate Equation Model, Invited to be submitted to a special edition of the *South African Journal of Science*, August, 2008
3. M.J.D. Esser, D. Preussler, **E.H. Bernhardt**, C. Bollig and K. Petermann, Diode-end-pumped Tm:GdVO₄ laser operating at 1818 nm and 1915 nm, To be submitted to *Optics Express* after approval of client, August, 2008
4. C. Bollig, C. Jacobs, M.J.D. Esser, **E.H. Bernhardt** and H.M. von Bergmann, Elimination of Lifetime Quenching through Gain Optimization in a Q-switched high-power end-pumped Nd:YLF Laser, To be submitted to *Optics Express*, August, 2008

International Conference Papers

1. **E.H. Bernhardt**, C. Bollig, A. Forbes and M.J.D. Esser, A Time-Dependent Analytical Thermal Model To Investigate Thermally Induced Stresses In Quasi-CW Pumped Laser Rods, In Proceedings of the *3rd EPS-QEOD Europhoton Conference*, Paris, France, 31 August - 5 September, 2008
2. C. Bollig, W.S. Koen, H. Strauss, **E.H. Bernhardt**, R. Botha, M.J.D. Esser and D. Preussler, Exploiting the natural doping gradient of Nd:YLF crystals for high power end-pumped lasers, In Proceedings of the *3rd EPS-QEOD Europhoton Conference*, Paris, France, 31 August - 5 September, 2008
3. **E.H. Bernhardt**, C. Bollig, M. Eichhorn, M.J.D. Esser, P. Fuhrberg, A. Hirth, C. Kieleck, M. Schellhorn and K. Scholle, High-Power Diode-Pumped 2 Micron

LIST OF PUBLICATIONS

Lasers, In Proceedings of the *17th International Laser Physics Workshop*, Trondheim, Norway, 30 June - 4 July, 2008

4. **E.H. Bernhardt**, C. Bollig, L. Harris, M.J.D. Esser and A. Forbes, Investigating Thermal Stresses in Quasi-CW Pumped Tm:YLF Laser Crystals, In Proceedings of the *Advanced Solid-State Photonics International Conference*, ISBN 1-55752-850-0, Nara, Japan, 27 - 30 January, 2008
5. M.J.D. Esser, C. Bollig, D. Preussler, C. Jacobs, W.S. Koen and **E.H. Bernhardt**, High power diode and pumped Tm:GdVO₄ laser operating at 1818 nm and 1915 nm, In Proceedings of the *Marie Curie Chair Conference Recent advances in laser spectroscopy and laser technology*, Lodz, Poland, 29 - 31 May, 2007

National Conference Papers

1. **E.H. Bernhardt**, A. Forbes, C. Bollig and M.J.D. Esser, A Time-Dependent Analytical Thermal Model To Investigate Thermally Induced Stresses In Quasi-Continuous-Wave Pumped Laser Rods, In Proceedings of the *53rd South African Institute of Physics Conference*, University of Limpopo, South Africa, July, 2008
2. **E.H. Bernhardt**, C. Bollig, A. Forbes and M.J.D. Esser, Modelling Mid-Infrared Diode-Pumped Solid-State Lasers, In Proceedings of the *52nd South African Institute of Physics Conference*, University of the Witwatersrand, Johannesburg, South Africa, July, 2007
3. C. Bollig, D. Preussler, M.J.D. Esser, S. Ngcobo, C. Jacobs, R.C. Botha, W.S. Koen, **E.H. Bernhardt**, A.R. Sarmani and L.R Botha, Solid-State Laser Source Research at the CSIR National Laser Centre, In Proceedings of the *52nd South African Institute of Physics Conference*, University of the Witwatersrand, Johannesburg, South Africa, July, 2007
4. M.J.D. Esser, C. Bollig, D. Preussler, C. Jacobs, W.S. Koen and **E.H. Bernhardt**, Diode-end-pumped Tm:GdVO₄ laser at selected wavelengths, In Proceedings of the *52nd South African Institute of Physics Conference*, University of the Witwatersrand, Johannesburg, South Africa, July, 2007

References

- Barnes, N.P., & Gettemy, D.J. 1980. Temperature variation of the refractive indices of yttrium lithium fluoride. *J. Opt. Soc. Am.*, **70**, 1244.
- Bernhardi, E.H., Forbes, A., Bollig, C., & Esser, M.J.D. 2008a. Estimation of thermal fracture limits in quasi-continuous-wave end-pumped lasers through a time-dependent analytical model. *Optics Express*, **16**, 11115–11123.
- Bernhardi, E.H., Bollig, C., Harris, L., Esser, M.J.D., & Forbes, A. 2008b. Investigating Thermal Stresses in Quasi-CW Pumped Tm:YLF Laser Crystals. *Advanced Solid-State Photonics International Conference*, ISBN 1–55752–850–0, 27–30 January, Nara, Japan.
- Bernhardi, E.H., Bollig, C., Esser, M.J.D., Forbes, A., Botha, L.R., & Jacobs, C. 2008c. A Single-Element Plane-Wave Solid-State Laser Rate Equation Model. Invited to be submitted to a special edition a special edition of the *South African Journal of Science*.
- Bollig, C., Jacobs, C., Esser, M.J.D., Bernhardi, E.H., & von Bergmann, H.M. 2008. Elimination of Lifetime Quenching through Gain Optimization in a Q-switched high-power end-pumped Nd:YLF Laser. To be submitted to *Optics Express* in August.
- Chen, T.S, Anderson, V.L., & Kahan, O. 1990. Measurements of heating and energy storage in diode-pumped Nd:YAG. *IEEE J. Quantum Electron.*, **26**, 6–8.
- Chénais, S., Balembois, F., Druon, F., Lucan-Leclin, G., & Georges, P. 2004. Thermal Lensing in Diode-Pumped Ytterbium Lasers-Part I: Theoretical Analysis and wavefront Measurements. *IEEE J. Quantum Electron.*, **40**, 1217–1234.
- Clarkson, W.A. 2001. Thermal effects and their mitigation in end-pumped solid-state lasers. *J. Phys. D: Appl. Phys.*, **34**, 2381–2395.
- Cousins, A.K. 1992. Temperature and Thermal Stress Scaling in Finite-Length End-Pumped Lasers Rods. *IEEE J. Quantum Electron.*, **28**, 1057–1069.

REFERENCES

- Cross, P.L. 2004. Database of laser materials. *Laser Systems Branch, NASA Langley Research Center, USA*, [http : //aesd.larc.nasa.gov/gl/laser/dbmain.htm](http://aesd.larc.nasa.gov/gl/laser/dbmain.htm) [Accessed March 2005].
- Czeranowsky, C. 2002. *Resonatorinterne Frequenzverdopplung von diodengepumpten Neodym-Lasern mit hohen Ausgangsleistungen im blauen Spektralbereich*. Ph.D. thesis, University of Hamburg.
- Didierjean, J., Hérault, E., Balembois, F., Georges, P., Altmann, K., & Pflaum, C. 2003. Comparison of absolute temperature measurements in diode-end-pumped laser crystals with FEA simulations. [https : //www.las - cad.com/files/PP_FEA_comparison.pdf](https://www.las-cad.com/files/PP_FEA_comparison.pdf).
- Egglestone, J.M., Kane, T.Y., Kuhn, K., Unternahrer, J., & Byer, R.L. 1984. The Slab geometry laser - Part I: Theory. *IEEE J. Quantum Electron.*, 289–301.
- Esser, M.J.D., Bollig, C., Preussler, D.R., Jacobs, C., Koen, W.S., & Bernhardt, E.H. 2007. High power diode and pumped Tm:GdVO₄ laser operating at 1818 nm and 1915 nm. *Marie Curie Chair Conference Recent advances in laser spectroscopy and laser technology*, 29–31 May, Lodz, Poland.
- Esser, M.J.D., Preussler, D., Bernhardt, E.H., Bollig, C., & Petermann, K. 2008. Diode-end-pumped Tm:GdVO₄ laser operating at 1818 nm and 1915 nm. To be submitted to *Optics Express* in August after approval of client.
- Fan, T.Y. 1992. Optimizing the Efficiency and Stored Energy in Quasi-Three-Level Lasers. *IEEE J. Quantum Electron.*, 28, 2692–2697.
- Fan, T.Y. 1993. Heat generation in Nd:YAG and Yb:YAG. *IEEE J. Quantum Electron.*, 29, 1457–1459.
- Fan, T.Y. 1995. Diode-Pumped Solid-State Lasers. *Chap. 6, pages 163–193 of: Miller, A., & Finlayson, D.M. (eds), Laser Sources and Applications*. St Andrews: SUSSP Publications and Institute of Physics Publishing.
- Fan, T.Y., & Byer, R.L. 1987. Modeling and CW Operation of a Quasi-Three-Level 946 nm Nd:YAG Laser. *IEEE J. Quantum Electron.*, 605–612.
- Fan, T.Y., & Byer, R.L. 1988. Diode Laser-Pumped Solid-state Lasers. *IEEE J. Quantum Electron.*, 24, 895–912.
- Koechner, W. 1988. *Solid-State Laser Engineering*. 2nd edn. Heidelberg, Germany: Springer-Verlag.

REFERENCES

- Koechner, W. 1996. *Solid-State Laser Engineering*. 4th revised and updated edn. Heidelberg, Germany: Springer-Verlag.
- Koechner, W., & Rice, D.K. 1970. Effect of birefringence on the performance of linearly polarized YAG:Nd lasers. *IEEE J. Quantum Electron.*, **6**, 557–566.
- Kracht, D., Frede, M., Wilhelm, R., & Fallnich, C. 2005. Comparison of crystalline and ceramic composite Nd:YAG for high power diode end-pumping. *Optics Express*, **13**, 6212–6216.
- Kumar, G. A., Lu, J., Kaminskii, A. A., Ueda, K., Yagi, H., T., Yanagitani, & Unnikrishnan, N. V. 2004. Spectroscopic and Stimulated Emission Characteristics of Nd³⁺ in Transparent YAG Ceramics. *IEEE J. Quantum Electron.*, **40**, 747–758.
- LASCAD. 2008. Homepage: <https://www.las-cad.com/>.
FEA Manual: https://www.las-cad.com/files/PP_FEA.pdf.
- Lienhard, J.H., & Lienhard, J.H. 2008. *A Heat Transfer Textbook*. 1.31 edn. Cambridge, Massachusetts, USA: Phlogiston Press.
- Lisiecki, R., Solarz, P., Dominiak-Dzik, G., & Ryba-Romanowski, W. 2006. Comparative optical study of thulium-doped YVO₄, GdVO₄, and LuVO₄ single crystals. *Physical Review B*, **74**.
- Loudon, R. 1983. *The Quantum Theory of Light*. 2 edn. Walton Street, Oxford: Oxford University Press.
- Maiman, A.H. 1960. Stimulated Optical Radiation in Ruby. *Nature*, **187**, 493–494.
- Pachotta, R., Aus der Au, J., & Keller, U. 2000. Thermal effects in High-Power End-Pumped Lasers with Elliptical-Mode Geometry. *IEEE J. Quantum Electron.*, **6**, 636–642.
- Peng, X., Xu, L., & Asundi, A. 2005. High-power efficient continuous-wave TEM₀₀ intracavity frequency-doubled diode-pumped Nd:YLF laser. *Applied Optics*, **44**, 800–807.
- Pfistner, C., Weber, R., Weber, H.P., Merazzi, S., & Gruber, R. 1994. Thermal Beam Distortions in End-Pumped Nd:YAG, Nd:GSGG and Nd:YLF Rods. *IEEE J. Quantum Electron.*, **30**, 1605–1615.
- Pollak, T.M., Wing, W.F., Grasso, R.J., Chicklis, E.P., & Jenssen, H.P. 1982. CW Laser Operation of Nd:YLF. *IEEE J. Quantum Electron.*, **18**, 159.

REFERENCES

- Pollnau, M., Hardman, P.J., Kern, M.A., Clarkson, W.A., & Hanna, D.C. 1998. Upconversion-induced heat generation and thermal lensing in Nd:YLF and Nd:YAG. *Physical Review B*, **58**, 16076–16092.
- Qi, Y., Zhu, X., Lou, Q., Ji, J., Dong, J., & Wei, Y. 2005. Nd:YAG ceramic laser obtained high slope efficiency of 62% in high power applications. *Optics Express*, **13**, 8725–8729.
- Risk, W.P. 1988. Modeling of longitudinally pumped solid-state lasers exhibiting re-absorption losses. *J. Opt. Soc. Am. B*, **5**, 1412–1423.
- Rustad, G. 1994. *Modelling and experimental investigation of laser-diode end-pumped and side-pumped thulium- and holmium doped lasers*. Ph.D. thesis, University of Oslo.
- Rustad, G., & Stenersen, K. 1996. Modeling of Laser-Pumped Tm and Ho Lasers Accounting for Upconversion and Ground-State Depletion. *IEEE J. Quantum Electron.*, **32**, 1645–1656.
- Ryan, J.R., & Beach, R. 1992. Optical absorption and stimulated emission of neodymium in yttrium lithium fluoride. *J. Opt. Soc. Am. B*, **9**, 1883.
- Schellhorn, M., & Hirth, A. 2002. Modeling of Intracavity-Pumped Quasi-Three-Level Lasers. *IEEE J. Quantum Electron.*, **38**, 1455–1464.
- Schmid, M., Graf, Th, & Weber, H.P. 2000. Analytical model of the temperature distribution and the thermally induced birefringence in laser rods with cylindrically symmetric heating. *J. Opt. Soc. Am. B*, **17**, 1398–1404.
- Siegman, A.E. 1986. *LASERS*. Mill Valley, California: University Science Books.
- So, S., Mackenzie, J.I., Shepherd, D.P, Clarkson, W.A, Betterton, J.G., & Gorton, E.K. 2006. A power-scaling strategy for longitudinally diode-pumped Tm:YLF lasers. *Appl. Phys. B.*, **84**, 389–393.
- Sousa, J.M., Salcedo, J.R., & Kuzmin, V.V. 1997. Simulation of laser dynamics and active Q-switching in Tm,Ho:YAG and Tm:YAG lasers. *Appl. Phys. B*, **64**, 25–36.
- VLOC Catalog. 2008. www.vloc.com/PDFs/VLOCcat.pdf, February.
- VLOC YAG Brochure. 2008. www.vloc.com/PDFs/YAGBrochure.pdf, February.
- Walsh, B. 1995. *Spectroscopy and excitation dynamics of the trivalent lanthanides Tm and Ho in LiYF₄*. M.Phil. thesis, Boston College.

REFERENCES

- Weber, R., Neuenschwander, B., & Weber, H.P. 1999. Thermal effects in solid-state laser materials. *Optical Materials*, **11**, 245–254.
- Yan, L., & Lee, C.H. 1994. Thermal effects in end-pumped Nd:phosphate glasses. *J. Appl. Phys.*, **75**, 1286–1292.
- Zagumennyi, A.I., Mikhailov, V.A., Vlasov, V.I., Sirotkin, A.A., Podreshetnikov, V.I., Kalachev, Yu.L., Zavartsev, Yu.D., Kutovoi, S.A., & Shcherbakov, I.A. 2003. Diode-Pumped Lasers Based on GdVO₄ Crystal. *Laser Physics*, **13**, 311–318.

Estimation of thermal fracture limits in quasi-continuous-wave end-pumped lasers through a time-dependent analytical model

E. H. Bernhardt^{1,2}, A. Forbes^{1,2,*}, C. Bollig^{1,*} and M. J. D. Esser¹

¹Council for Scientific and Industrial Research, National Laser Centre, PO Box 395, Pretoria 0001, South Africa

²School of Physics, University of KwaZulu-Natal, Private Bag X54001, Durban 4000, South Africa

Corresponding authors: aforbes1@csir.co.za and cbollig@csir.co.za

Abstract: A time-dependent analytical thermal model of the temperature and the corresponding induced thermal stresses on the pump face of quasi-continuous wave (qcw) end-pumped laser rods is derived. We apply the model to qcw diode-end-pumped rods and show the maximum peak pump power that can be utilized without fracturing the rod. To illustrate an application of the model, it is applied to a qcw pumped Tm:YLF rod and found to be in very good agreement with published experimental results. The results indicate new criteria to avoid fracture when operating Tm:YLF rods at low qcw pump duty cycles.

©2008 Optical Society of America

OCIS codes: (140.3480) Lasers, diode-pumped; (140.6810) Thermal effects.

References and links

1. W. Koechner, *Solid-State Laser Engineering* 4th ed., (Springer-Verlag Berlin, Heidelberg, Germany, 1996).
2. C. Pfistner, R. Weber, H. P. Weber, S. Merazzi and R. Gruber, "Thermal Beam Distortions in End-Pumped Nd:YAG, Nd:GSGG and Nd:YLF," *IEEE J. Quantum Electron.* **30**, 1605–1615 (1994).
3. A. K. Cousins, "Temperature and Thermal Stress Scaling in Finite-Length End-Pumped Lasers Rods," *IEEE J. Quantum Electron.* **28**, 1057–1069 (1992).
4. L. Yan, and C. H. Lee, "Thermal Effects in End-Pumped Nd:phosphate Glasses," *J. Appl. Phys.* **75**, 1286–1292 (1994).
5. S. Chénais, S. Forget, F. Druon, F. Balembois and P. Georges. "Direct and Absolute Temperature Mapping and Heat Transfer Measurements in Diode-End-Pumped Yb:YAG," *Appl. Phys. B* **79**, 221–224 (2004).
6. X. Peng, L. Xu and A. Asundi, "High-power efficient continuous-wave TEM₀₀ intracavity frequency-doubled diode-pumped Nd:YLF laser," *Appl. Opt.* **44**, 800–807 (2005).
7. G. Barton, *Elements of Green's Functions and Propagation*, (Oxford University Press, Oxford, 1995).
8. H. S. Carslaw and J. C. Jaeger, *Conduction of Heats in Solids*, (Oxford University Press, Oxford, 1959).
9. T. Y. Fan, "Heat Generation in Nd:YAG and Yb:YAG," *IEEE J. Quantum Electron.* **29**, 1457–1459 (1993).
10. S. P. Timoshenko and J. N. Goodier, *Theory of Elasticity* 3rd ed., (McGraw-Hill, New York, 1970).
11. B. A. Boley and J. H. Weiner, *Theory of Thermal Stresses*, (Courier Dover Publications, New York, 1997).
12. LASCAD Manual, (LASCAD, 2008), https://www.las-cad.com/files/PP_FEA.pdf.
13. ABAQUS Finite Element Software Package (ABAQUS, 2008) http://www.simulia.com/products/abaqus_fea.html.
14. E. H. Bernhardt, C. Bollig, L. Harris, M. J. D. Esser and A. Forbes, "Investigating thermal stresses in quasi-cw pumped Tm:YLF laser crystals," in *Proceedings of Advanced Solid-State Photonics*, (Nara, Japan, 2008), Poster WB11.
15. S. So, J. I. Mackenzie, D. P. Shepherd, W. A. Clarkson, J. G. Betterson and E. K. Gorton, "A power-scaling strategy for longitudinally diode-pumped Tm:YLF lasers," *Appl. Phys. B* **84**, 389–393 (2006).
16. M. Pollnau, P. J. Hardman, M. A. Kern, W. A. Clarkson, and D. C. Hanna, "Upconversion-induced heat generation and thermal lensing in Nd:YLF and Nd:YAG," *Phys. Rev. B* **58**, 16076–16092 (1998).
17. B. M. Walsh, N. P. Barnes, M. Petros, J. Yu, and U. N. Singh, "Spectroscopy and modeling of solid state lanthanide lasers: Application to trivalent Tm³⁺ and Ho³⁺ in YLiF₄ and LuLiF₄," *J. Appl. Phys.* **95**, 3255–3271 (2004).

1. Introduction

The power scaling of diode-end-pumped solid-state lasers is a very active area of research. The main problem that limits the power scaling of these lasers is the generation of heat inside the laser gain medium; the generated heat causes steep temperature gradients inside the crystal, which in turn produce stress, leading to fracture. Fracture of the laser material occurs when the thermally induced stress exceeds the ultimate strength of the material [1]. When the continuous wave (cw) pump power exceeds the power at which crystal fracture occurs, the pump source is often modulated in time, creating a so called quasi-continuous wave (qcw) pump, with the effect of reducing the average pump power to below the fracture limit, while maintaining a high output power during the on-time of the pump pulse.

In order to investigate the thermally induced stresses and the power limitations due to fracture, a thermal model of the laser gain medium is required. Existing analytical thermal models that describe the temperature and stresses in laser crystals are restricted to special cases and approximations, such as cw pump sources and steady-state conditions [1–5]. In this paper an analytical thermal model that determines the transient behaviour of the temperature and the corresponding induced stresses on the pump face of an isotropic laser rod is derived from first principles. To the best of our knowledge this is the first time that such a time-dependent analytical model has been reported. We validate the model through finite element analysis, and apply the model to qcw pumped Tm:YLF laser rods, and find favourable agreement between the calculated fracture limits and the experimentally determined values reported in the literature.

We have particularly chosen to apply the model to a YLF rod because power scaling with this material is limited by the relatively low fracture limit of 40 MPa, which is ~5 times lower than that of YAG [6]. Despite being derived for isotropic rods, we show that the model may be applied to anisotropic rods on condition that the highest linear expansion and the lowest thermal conductivity of the respective a- and c-axis of the crystal are used in the calculation. Finally, we illustrate how the model may be used to estimate the peak pump power that can safely be used to qcw pump a laser rod at a given duty cycle, opening the way to fracture-free power scaling with qcw pump sources.

2. Theory

In this section the transient temperature and stress profiles on the pump face of a longitudinally pumped isotropic laser rod are derived. We assume that the Rayleigh range of the pump beam is much longer than the length of the rod so that the pump beam is treated as perfectly collimated inside the rod. This implies that only the pump face need be considered since the pump light in the gain medium follows an exponential decay, with the steepest temperature gradient (and thus stress) on the pump face [2,4]. A closed form solution for the time dependent temperature profile on the surface of the crystal rod, $u(r,t)$, may be found by solving the non-homogeneous heat diffusion equation [7,8]:

$$\frac{\partial u(r,t)}{\partial t} - D\nabla^2 u(r,t) = Q(r,t), \quad (1)$$

for a generalized source term $Q(r,t)$. Here $D = k/\rho C_p$ is the diffusivity, k is the thermal conductivity, ρ is the density and C_p is the heat capacity of the laser material respectively, while all other terms have their usual meaning. We will assume that the rod has a length l and a radius R , and is homogenous and isotropic. Furthermore, we will assume that the boundary of the rod is at a constant temperature, $u(R,t) = 0$, with no initial temperature profile on its pump face: $u(r,0) = 0$. With these boundary conditions, Eq. (1) may be solved directly by use of an appropriate Green's function, with the solution given in integral form as:

$$u(r,t) = \int_0^t \int_0^R Q(\xi,\tau) G(r,\xi,t-\tau) d\xi d\tau, \quad (2)$$

with the Green's function $G(r, \xi, t)$ given by [7]:

$$G(r, \xi, t) = \sum_{m=1}^{\infty} \frac{2\xi}{R^2 J_1^2(\mu_m)} J_0(\mu_m r/R) J_0(\mu_m \xi/R) \exp\left(-\frac{D\mu_m^2 t}{R^2}\right). \quad (3)$$

The summation is over the positive roots (μ_m) of the zeroth order Bessel function, J_0 . For the common experimental configuration where the pump beam is imaged onto the rod face from a multimode fibre, the pump intensity may be approximated as having a top-hat spatial intensity profile. Figure 1 shows an example of a measured top-hat transverse intensity profile as produced by a fibre-coupled diode pump. If in addition the pump is not assumed to be cw but rather the more general qcw, consisting of a pulse train of on-off pulses with on-time τ_{on} (with τ_{on} usually longer than the upper-state lifetime of the laser gain medium) and period T , we may write the source term as:

$$Q(r, t) = \begin{cases} \frac{\alpha\eta E}{\pi w^2 \rho C_p \tau_{on}} & ; nT \leq t \leq nT + \tau_{on} \\ 0 & ; nT + \tau_{on} \leq t \leq (n+1)T \end{cases}, \quad (4)$$

where n is the number of pulses, E is the energy in each pulse and w is the radius of the top-hat beam. α is the absorption coefficient in units of inverse length of the crystal, while η is a parameter to account for the fact that not all the absorbed pump light is converted into heat. This model can be applied under lasing or non-lasing conditions by choosing an appropriate value for η . Typical values for the heat load efficiency are $\eta=0.32$ (lasing) and $\eta=0.4$ (non-lasing) [9].

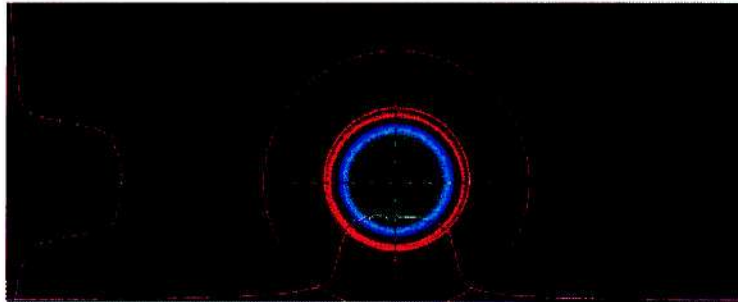


Fig. 1. An example of a measured top-hat transverse intensity profile produced by a fibre coupled diode laser pump (own experimental results).

Substituting Eqs. (3) and (4) into Eq. (2) and solving both the time and spatial integrals separately yields the following analytical expression for the temperature on the pump face of the rod:

$$u(r, pT+t) = \frac{2\alpha\eta ER}{k\pi w \tau_{on}} \sum_{m=1}^{\infty} \frac{J_0(\mu_m r/R) J_1(\mu_m w/R) f(p, t, \mu_m)}{\mu_m^3 J_1^2(\mu_m)}, \quad (5)$$

with the time dependence given by $f(p, t, \mu_m)$ as:

$$f(p, t, \mu_m) = \exp\left(-\mu_m^2 \frac{t}{\tau_D}\right) \left\{ \frac{\left[\exp\left(\mu_m^2 \frac{\tau_{on}}{\tau_D}\right) - 1 \right] \exp\left(-\mu_m^2 \frac{pT}{\tau_D}\right) - 1}{1 - \exp\left(\mu_m^2 \frac{T}{\tau_D}\right)} \left[1 - \exp\left(\mu_m^2 \frac{\tau}{\tau_D}\right) \right] \right\}, \quad (6)$$

with $\tau = \min[t, \tau_{on}]$. Here we have introduced a new variable, $\tau_D = R^2/D$, which we refer to as the diffusion relaxation time of the system, and for convenience the temperature is calculated after p complete pulses plus some time t into the $p+1$ pulse, so that the total elapsed time from the start of the pumping process is $pT + t$. While the summation in Eq. (5) is carried to infinity, in practice one finds that 30 terms or above leads to very good convergence of the series. Equation (5) may easily be rewritten in terms of peak pump power (P_p) or average pump power (P_{av}) rather than pump energy (E) by noting that for the source term in this study $P_p = E/\tau_{on}$ and $P_{av} = E/T$ (note: here we have assumed that the time pulse envelope is a square pulse; for other cases the peak pump power expression may have to be modified in an appropriate manner). In the special case of a cw pump source, $T = \tau_{on}$ so that the peak and average pump powers are identical.

By making use of a plane-strain approximation and assuming that the stress in the axial direction is zero, we may calculate the radial and tangential stresses from the temperature profile from [10,11]:

$$\sigma_r(r, t) = C \left[\frac{1}{R^2} \int_0^R u(r, t) r dr - \frac{1}{r^2} \int_0^r u(r, t) r dr \right]; \quad (7a)$$

$$\sigma_\theta(r, t) = C \left[\frac{1}{R^2} \int_0^R u(r, t) r dr + \frac{1}{r^2} \int_0^r u(r, t) r dr - u(r, t) \right], \quad (7b)$$

where $C = \gamma Y / (1 - \nu)$, with γ the linear coefficient of expansion, Y is Young's modulus and ν is Poisson's ratio. The plain-strain approximation is valid for $l/R \gg 1$ (a long rod) [11]. For the case where $l/R \ll 1$ (a thin disk), the plane-stress approximation is used where Eqs. (7a) and (7b) also hold with $C = \gamma Y$ [11]. One can readily show that Eqs. (7a) and (7b) can be solved analytically to yield:

$$\sigma_r(r, pT + t) = \frac{2C\alpha\eta ER}{k\pi w\tau_{on}} \sum_{m=1}^{\infty} \frac{J_1(\mu_m w/R)}{\mu_m^3 J_1^2(\mu_m)} \left[\frac{J_1(\mu_m)}{\mu_m} - \frac{RJ_1(\mu_m r/R)}{r\mu_m} \right] f(p, t, \mu_m); \quad (8a)$$

$$\sigma_\theta(r, pT + t) = \frac{2C\alpha\eta ER}{k\pi w\tau_{on}} \sum_{m=1}^{\infty} \frac{J_1(\mu_m w/R)}{\mu_m^3 J_1^2(\mu_m)} \left[\frac{J_1(\mu_m)}{\mu_m} + \frac{RJ_1(\mu_m r/R)}{r\mu_m} - J_0(\mu_m r/R) \right] f(p, t, \mu_m). \quad (8b)$$

Due to the fact that the stress tensor alone does not provide enough information regarding crystal fracture, we use the maximum shear stress to predict fracture [12]. This is also known as the stress intensity or the Tresca failure criterion, which in the plain-strain approximation reduces to:

$$\begin{aligned} \sigma_T(r, pT + t) &= |\sigma_\theta - \sigma_r| \\ &= \left| \frac{2C\alpha\eta ER}{k\pi w\tau_{on}} \sum_{m=1}^{\infty} \frac{J_1(\mu_m w/R)}{\mu_m^3 J_1^2(\mu_m)} J_2(\mu_m r/R) f(p, t, \mu_m) \right|, \end{aligned} \quad (9)$$

where we have made use of the well known relation $J_2(x) = 2J_1(x)/x - J_0(x)$. Equations (5), (8) and (9) allow the temperature, stresses and fracture limit to be calculated for any qcw pulse train, as a function of both time and position in the crystal rod.

3. Model validation

As a verification of the analytical thermal model, a time-dependent three dimensional coupled thermal-stress finite element analysis was implemented in a commercial software package, ABAQUS [13,14]. The average computation time of each finite element simulation (5560 discretization) was approximately 5.5 hours on a dual-core 2.4 GHz processor (the analytical model takes ~1–2 s). In analogy with convective heat transfer, we have specified a Neumann boundary condition with a heat transfer coefficient at the interface between the crystal and the copper heat sink. We have used a heat transfer coefficient of $0.9 \text{ Wcm}^{-2}\text{K}^{-1}$, which corresponds to a layer of indium foil between the crystal and the heat sink [5]. In the remaining text the finite element analysis will be referred to as the *numerical* model [14].

The analytical and numerical models have been applied to reported results [15] of a cw pumped, 4% doped, Tm:YLF laser rod with $l = 12 \text{ mm}$ and $R = 1.5 \text{ mm}$ ($l/R=8$ so that we make use the plain-strain approximation as discussed in section (2)). The pump beam was a near top-hat profile with $M^2 \sim 100$ and a pump radius of $w = 470 \mu\text{m}$ in the middle of the crystal. The onset of fracture was reported at an incident power of 47.2 W ($\alpha = 1.43 \text{ cm}^{-1}$; $\eta = 0.33$). While the actual stress values at fracture are not reported, it is known that the fracture limit of YLF crystals is in the 33–40 MPa range [1,6]. The parameters that were used in the numerical and analytical thermal models are shown in Table 1.

The analytical model predicts a maximum Tresca stress of 42 MPa which agrees very well with the reported 33–40 MPa fracture limit range [1,6]. The numerical model results in a maximum Tresca stress of 41 MPa. This shows that for a cw pump, the analytical thermal model is consistent with both the experimental fracture data and with the numerical solutions of a three-dimensional finite element analysis. Since the analytical thermal model proved to be accurate for a cw pump beam, the transient behaviour of the temperature and the induced stresses were determined for various qcw pump duty cycles, defined as τ_{on}/T . Figure 2(a) and 2(b) show the predicted time-dependence of the temperature in the centre of the pump face of the Tm:YLF rod for a 10% and a 50% pump duty cycle respectively ($\tau_{on} = 10 \text{ ms}$). The upper and lower boundaries of the shaded red region in Fig. 2 indicate the analytical model's predictions of the temperature when the thermal conductivity of the c- and the a-axis of Tm:YLF were used respectively. It is clear from the graphs that there is very good agreement between the analytical and numerical models when the lowest thermal conductivity is used in the calculations. Figure 3 illustrates that the thermally induced stresses as calculated by the two models show very good agreement when the highest linear expansion coefficient is used in the analytical model. The upper and lower boundaries of the shaded red region in Fig. 3 indicate the analytical model's predictions of the maximum stress on the pump face when the two respective linear expansion coefficients of Tm:YLF were used along with the lowest thermal conductivity.

By considering the transient stress distribution on the entire pump face with a qcw pump source, it is evident that the maximum stress does not always occur on the edge-surface ($r = R$) of the rod; this is contrary to the case of a cw pump beam [4]. The position of the maximum stress changes during a single qcw pump pulse as well as between qcw pulses. Figure 4(a) shows an animation of the analytically predicted σ_r on the pump face of the Tm:YLF rod when subjected to a 90 W peak power pump beam at 50 Hz ($T = 20 \text{ ms}$; $\tau_{on} = 10 \text{ ms}$), while Fig. 4(b) shows an animation of the numerically predicted σ_r throughout the bulk of the Tm:YLF rod. A cross-section of the stress is overlaid on the analytical animation, and clearly shows the "peak" where the stress is maximum and its movement in time as the pulses accumulate. Note that the numerical solution does not exhibit the same symmetrical stress distribution on the pump face as the analytical solution since the anisotropic characteristics of Tm:YLF were accounted for in the numerical model and not in the analytical model.

Table 1. Parameter values of the pumped Tm:YLF rod that were implemented in the simulations.

Parameter	Thermal Model	Reference
Pump beam radius (w) [mm]	0.47	[15]
Rod radius (R) [mm]	1.5	[15]
Absorption coefficient (α) [cm^{-1}]	1.43	[15]
Thermal conductivity (k) [$\text{W}\cdot\text{m}^{-1}\cdot\text{K}^{-1}$]	7.2 (a-axis), 5.8 (c-axis)	[1,16]
Linear expansion coefficient (β) [10^{-6}K^{-1}]	13 (a-axis), 8.0 (c-axis)	[1,17]
Fractional heat load (η)	0.33	estimated
Poisson's ratio (ν)	0.33	[1,16]
Young's modulus (Y) [GPa]	75	[1,2]
Density (ρ) [$\text{g}\cdot\text{cm}^{-3}$]	3.9	[1,17]
Specific heat capacity (C_p) [$\text{J}\cdot\text{g}^{-1}\cdot\text{K}^{-1}$]	0.79	[1,17]

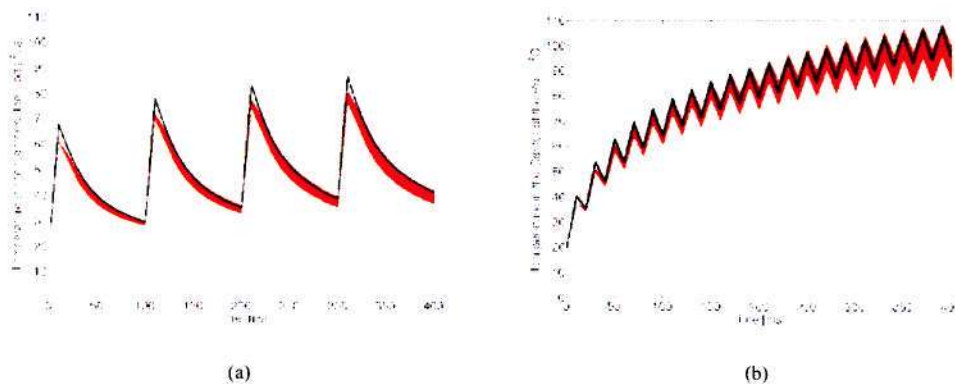


Fig. 2. The analytically (red) and numerically (black) predicted temperature in the centre of the Tm:YLF rod as a function of time while the rod is subjected to a qcw pump with a peak power of (a) 200 W at 10 Hz ($\tau_m = 10$ ms) and, (b) 90 W at 50 Hz ($\tau_m = 10$ ms).

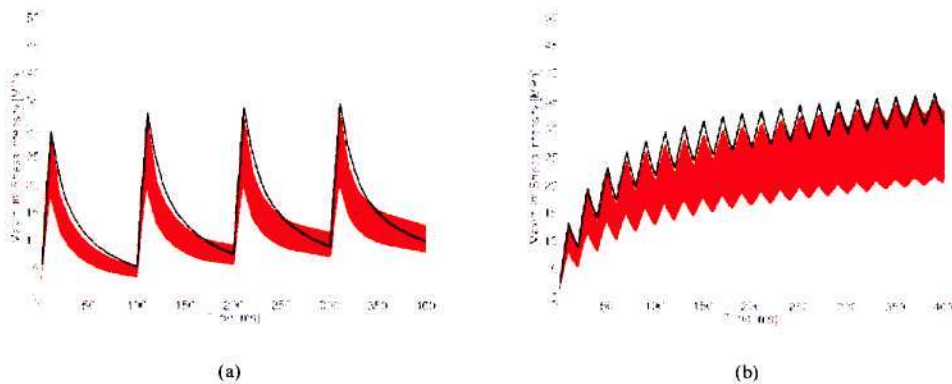


Fig. 3. The maximum stress on the pump face of the Tm:YLF rod as a function of time while the rod is subjected to a qcw pump with a peak power of (a) 200 W at 10 Hz ($\tau_m = 10$ ms), and (b) 90 W at 50 Hz ($\tau_m = 10$ ms). The analytical (red) and numerical (black) solutions are shown.

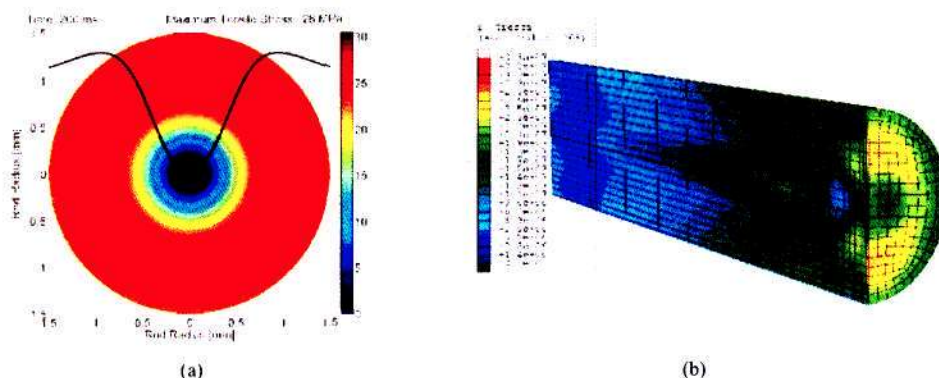


Fig. 4. (0.75 MB and 0.33 MB respectively) Animations of (a) the analytical stress distribution on the pump face and (b) the numerical stress distribution in volume of the Tm:YLF rod while it is subjected to a 90 W peak power qcw pump beam at 50 Hz ($\tau_{on} = 10$ ms).

4. Power scaling of Tm:YLF rods by qcw pumping

To achieve ever higher output powers from a diode-end-pumped solid state laser, the pump power itself must be increased in a concomitant manner. When the pump is a cw source, the high average powers required in some applications leads to high thermal loads, and the onset of fracture. A standard solution to this problem is to employ a qcw pump source, with the advantages that: (i) the average thermal load is reduced through a reduced duty cycle, and (ii) the qcw pulsing leads to higher peak pump power, resulting in much higher laser output power during the qcw pump pulses.

During the qcw operation of a solid-state laser, the generally accepted criteria to avoid thermal fracture is to pump the crystal with an average power (P_{av}) that is below the cw fracture pump power (P_{cw}):

$$P_{av} \leq P_{cw} \quad (10)$$

The thermal model developed in section (2) provides a more comprehensive criterion for safe qcw operation, through direct application of Eq. (9), and the results are shown in Fig. 5. The green shaded area in Fig. 5(a) shows the analytically predicted average power with which the Tm:YLF crystal can be pumped without causing thermal fracture, while the red region indicates the predicted onset of fracture using Eq. (10). The yellow region then indicates the region of disagreement between the two models. It is clear that for qcw pump duty cycles of 40% and higher, fracture of the Tm:YLF rod will indeed occur at average pump powers which are equal or greater to the cw fracture pump power, so that Eqs. (9) and (10) are in agreement. At pump duty cycles that are lower than 40%, the analytical model predicts that crystal fracture will occur at average powers that are significantly lower than the cw fracture pump power. By way of example, consider a qcw pump duty cycle of 10% ($T = 100$ ms; $\tau_{on} = 10$ ms) where the fracture limit of Tm:YLF is at $P_{cw} = 47$ W. For this qcw duty cycle, fracture would occur at $P_{av} > 26$ W, with the region $47 \text{ W} > P_{av} > 26 \text{ W}$ indicating the error of using Eq. (10). This error is indicated for all duty cycles as the yellow shaded area in Fig. 5(a). The implication is that Eq. (10) is a necessary but not sufficient condition for fracture-free qcw operation in Tm:YLF lasers.

An alternative approach to illustrate the results of the analytical thermal model is to consider the peak power during a qcw pump pulse and to note the peak power at which fracture occurs. The green shaded area in Fig. 5(b) indicates the qcw peak power that can be used to pump the Tm:YLF rod without fracturing it as predicted by the analytical model, while the red region indicates the fracture limit using Eq. (10); the yellow region is once again the region of discrepancy.

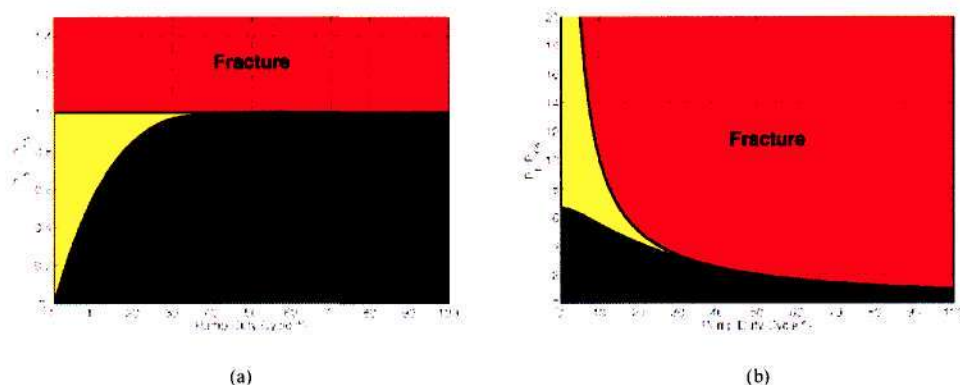


Fig. 5. (a) The average pump power (as a fraction of the cw fracture power P_{cw}) at which fracture of the Tm:YLF rod occurs as a function of qcw pump duty cycle ($\tau_{on} = 10$ ms). The green shaded region indicates the average pump power at which the Tm:YLF rod can be pumped without fracturing according to the analytical model. The yellow shaded region indicates the difference between the analytical model and P_{cw} . (b) The same notation as in (a) but for the peak pump power (in units of P_{cw}) at which fracture of the Tm:YLF rod occurs as a function of qcw pump duty cycle.

Considering the qcw pump duty cycle of 10%, we note that the Tm:YLF rod can be pumped with a peak pump power of $5.5\times$ higher (270 W) than the cw fracture power before fracture will occur, while Eq. (10) would predict a $10\times$ higher value (470 W).

The model predictions can thus be summarised as follows: the rule of thumb given by Eq. (10) is a necessary but not sufficient condition for fracture-free power scaling of Tm:YLF through the use of qcw pump sources. This is not surprising given that this criteria is not derived from an analysis of the onset of fracture, but is based rather on intuition. Equation (9) is derived from a full thermal analysis, and we suggest that this provides the necessary criterion for any laser rod to be pumped without fracture. In the limit that the duty cycle approaches the cw case, Eq. (9) correctly converges to Eq. (10) as expected.

5. Conclusion

A time-dependent analytical thermal model was developed to investigate the transient behaviour of thermally induced stresses in qcw end-pumped laser rods. The versatility of such a model is that all the material and pump laser parameters may be varied analytically, thereby aiding physical insight. For example, the model confirms exactly that the temperature increases linearly with pump power, as expected. Similarly, one can ‘instantaneously’ determine how the rod temperature varies with any of the key parameters, enabling one to easily probe the underlying physics with questions such as: how does the temperature profile vary with pump size w ? Determining this numerically would be extremely time consuming. Furthermore, the resulting analytical expression for the temperature of the rod may be used to determine other quantities, such as the optical aberrations likely to be imparted to a propagating wave through the crystal rod. The key advantages of the analytical model are ease of computation, as highlighted above, and time of computation. We reported that the average computation time of each finite element simulation was approximately 5.5 hours on a dual-core 2.4 GHz processor; this is in stark contrast to the analytical model in which the computational time is less than a couple of seconds on a standard PC, i.e., for all practical purposes it is ‘instantaneous’ in comparison.

The analytical model was used to investigate the thermal stress in a Tm:YLF rod at various qcw pump duty cycles, and was found to be in very good agreement with that of a time-dependent coupled thermal-stress finite element analysis, and with published experimental data. We have applied the analytical model to determine the maximum peak

power at which a Tm:YLF rod can be pumped before it will fracture. We show that at all qcw duty cycles the crystal will fracture at average power levels that are lower than predicted by using the corresponding cw fracture limit. The discrepancy is largest at low duty cycles, converging to a perfect agreement in the limiting case of a 100% duty cycle (cw). Thus we suggest a new criteria to be applied for safe power scaling of Tm:YLF rods. While the implementation of the analytical model has concentrated on YLF due to its low fracture limit, the model presented here may be applied to any end-pumped laser rod pumped using qcw or cw sources as the assumptions used to develop the analytical model are not material specific. It needs to be verified for other gain materials and other pumping conditions that the same discrepancy (between the predicted average power level at which fracture will occur and the cw fracture limit) exists at low duty cycles.

Exploiting the natural doping gradient of Nd:YLF crystals for high-power end-pumped lasers

C. Bollig¹, W. Koen^{1,2}, H. Strauss^{1,3}, E. Bernhardt^{1,2}, R. Botha³, D. Esser¹, D. Preussler¹

1. Council for Scientific and Industrial Research: National Laser Centre, PO Box 395, Pretoria, 0001, South Africa

2. University of KwaZulu-Natal, Durban, 4041, South Africa

3. University of Stellenbosch, Private Bag XI, Matieland, 7602, South Africa

Of the various Neodymium-doped materials, Nd:YLF is particularly attractive for use in high-power diode end-pumped solid-state lasers due to its weak thermal lens, especially on the σ -polarisation, and its long upper laser level lifetime that enables efficient energy storage for Q -switching. However, due to the low thermal fracture limit in Nd:YLF, power scaling has proven to be difficult.

In our previous work, we addressed several issues relating to Nd:YLF in a novel fashion and were subsequently able to demonstrate the highest published power for an end-pumped Nd:YLF laser [1]. The laser delivered a total output power of 60.3 W CW and an average power of 52 W when Q -switched between 5 and 30 kHz, with good beam quality and no sign of lifetime quenching. However, we experienced fracture at 5 kHz.

In order to address the fracture problem we decided to use crystals of a doping concentration below the 0.5% previously used. In addition, we decided to exploit the natural doping gradient along the length of the boule, which is especially pronounced at low concentrations but commonly ignored. In a collaboration, VLOC estimated the doping gradient of a specially manufactured boule (Fig. 2) and maintained the crystal orientation information during the manufacturing process of the 45 mm long, 6 mm diameter crystals. Initial thermal calculations indicate that for these crystals, the lower-doping end can be pumped 58% harder than the higher-doping end before the thermal fracture limit is reached.

To be able to pump each crystal rod from its low-doping end, we implemented a folded resonator (Fig. 1). In addition to using relatively low doping concentrations, we pumped at a wavelength of 805 nm, where the absorption of Nd:YLF is ~ 5 times lower than the conventionally used 792 or 797 nm. The combination of these techniques resulted in a more even distribution of the heat load along the length of the crystals. As in our previous work, we compensated for the strong astigmatism of the crystals by using two crystals with the c-axis vertical and two with the c-axis horizontal with a $\lambda/2$ -plate in-between [1].

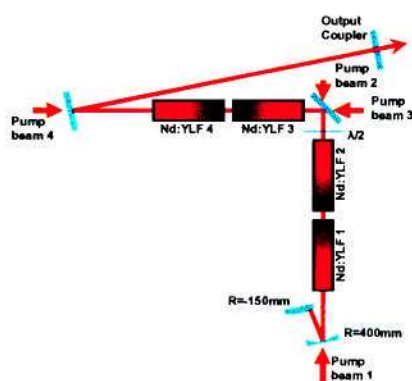


Fig. 1 Laser resonator

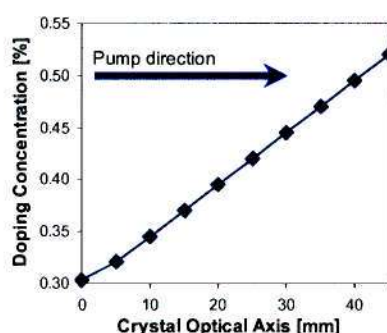


Fig. 2 Crystal doping gradient as estimated by VLOC

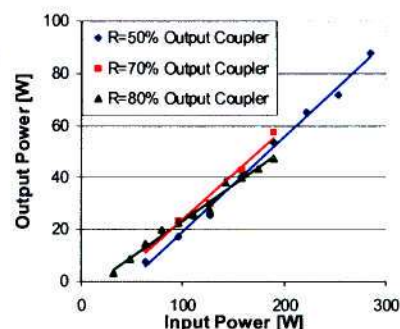


Fig. 3 Power under CW operation

With this configuration, no crystal damage occurred, even with all four fibre-coupled 75 W diode laser modules at full power. A total output power of up to 87 W CW was achieved, which is the highest reported so far but still less than expected (Fig. 3). Using Findlay-Clay and Caird analysis, the resonator loss was estimated to be 10% and 15% respectively. The crystals' total scatter loss was subsequently measured but was found to be only 1.64% round-trip loss at the laser wavelength.

We observed significant fluctuations in the output power and beam pointing. These could be because the laser operates in Zone II of the thermal stability diagram [2], which makes the laser very sensitive to misalignment and to small fluctuations in the pump overlap and variations in diffraction in the air. We believe that the lower than expected output power is due to this as well, rather than to actual resonator losses.

By redesigning the laser to operate in zone I, efficient and stable operation in excess of 100 W should be achievable. In the next step, Q -switched operation will be investigated, which has the potential to yield high average powers even at repetition rates below 5 kHz.

References

[1] C. Bollig, C. Jacobs, H. M. von Bergmann, and M. J. Esser, "High-power end-pumped Nd:YLF laser without lifetime quenching" CLEO/Europe 2005

[2] V. Magni, "Resonators for solid-state lasers with large-volume fundamental mode and high alignment stability," Appl. Opt. **25**, 107 (1986)

Investigating Thermal Stresses in Quasi-CW Pumped Tm:YLF Laser Crystals

E.H. Bernhardt^{1,2}, C. Bollig¹, L. Harris³, M.J.D. Esser¹, A. Forbes^{1,2}

¹ CSIR National Laser Centre, PO Box 395, Building 46, Pretoria, South Africa, 0001

² School of Physics, University of Kwazulu-Natal, Private Bag X54001, Durban, South Africa, 4000

³ CSIR Materials Science and Manufacturing, PO Box 395, Building 14F, Pretoria, South Africa, 0001
Emails: eberhardt@csir.co.za, cbollig@csir.co.za

Abstract: Time dependent thermally induced stresses in an end-pumped Tm:YLF laser rod are investigated numerically. The variation of the maximum incident pump power at the fracture point with respect to pump pulse length is investigated.

©2008 Optical Society of America

OCIS codes: (140.3480) Lasers, diode-pumped; (140.6810) Thermal effects

1. Introduction

The power scaling of diode end-pumped solid-state lasers is a very active area of research. The main problem that limits the power scaling of these lasers is the generation of heat inside the laser gain medium which can ultimately cause fracture. The generated heat causes steep temperature gradients inside the crystal, which in turn, produce stress. Fracture of the laser material occurs when the thermally induced stress exceeds the ultimate strength of the material [1].

When the continuous wave (CW) pump power exceeds the fracture power of the crystal, a quasi-continuous wave (QCW) pump is often used to reduce the average pump power to below the fracture pump power. In this paper we investigate the thermal stresses for a single QCW pump pulse. Due to the anisotropic nature of YLF, it is necessary to perform a three dimensional finite element analysis of the laser material in order to investigate the temporal and spatial behaviour of the thermally induced stresses [2].

In the next section, we discuss the theoretical model that we have implemented in the finite element analysis. In order to validate our numerical results, we compare the numerical solution with experimental results for a CW pump. After this has been verified, we investigate how the maximum temperature and thermally induced stresses vary with pulse length for the case of QCW pumping.

2. Theoretical Model

In this model we consider a super-Gaussian pump light distribution (in the X-Y plane). In general, the heat density added by the pump light beam to a crystal can be described by

$$Q(x, y, z) = \alpha \eta I_p(x, y, z) \quad (1)$$

where η is the fraction of absorbed pump power that is converted into heat, α is the absorption coefficient of the crystal and $I_p(x, y, z)$ is the intensity of the pump radiation [3].

For the case of a cylindrical crystal rod, pumped by a fibre-coupled diode, we assume that the pump beam radius in the x and y directions are the same so that the pump light intensity can be described by

$$I_p(x, y, z) = P_p e^{-\alpha z} C(z) e^{\left(-2 \left| \frac{\sqrt{x^2 + y^2}}{w} \right|^{SG}\right)} \quad (2)$$

where P_p is the incident pump power, $C(z)$ a normalisation factor, w the pump beam radius and SG is the super-Gaussian order. Since the propagation distance of the pump beam through the length of the crystal (12 mm) is well within the 87 mm pump beam Rayleigh range, we consider the pump beam to be collimated inside the crystal so that the pump beam radius has no z dependence.

In analogy with convective heat transfer, we have specified a heat transfer coefficient at the interface between the crystal and the copper heat sink. We used a heat transfer coefficient of $0.9 \text{ W}\cdot\text{cm}^{-2}\cdot\text{K}^{-1}$, which corresponds to a layer of indium foil between the crystal and the heat sink [4].

Equation (1) can now be used in a 3D finite element analysis to define the heat added to the laser material via the pump beam radiation.

Due to the fact that the stress tensor alone doesn't provide enough information regarding crystal fracture, we use the maximum shear stress to predict fracture [5]. This is also known as the stress intensity or the Tresca failure criterion

$$\sigma_T = \max(|\sigma_1 - \sigma_2|, |\sigma_2 - \sigma_3|, |\sigma_3 - \sigma_1|) \quad (3)$$

where σ_1 , σ_2 and σ_3 are the principal stresses.

3. Finite Element Analysis Results

We have implemented the model in the commercial finite element software package, ABAQUS [6]. In order to validate our model for the CW pump case, we have compared it with experimental results taken from [7] as well as a commercial laser modelling software package, LASCAD [8]. Since LASCAD is restricted to a CW pump beam, we implemented the time dependent simulations only in ABAQUS.

For the CW pump case, fracture of the 4% doped Tm:YLF rod was reported at 38.7 W of absorbed pump power, which corresponds to 47.2 W of incident power, assuming an absorption coefficient of 1.43 cm^{-1} [7]. We have assumed that 33% of the absorbed pump power is converted into heat. They reported a quasi-top-hat pump with M^2 of 100 and pump focus radius of $\sim 470 \mu\text{m}$ in the middle of the 12 mm long, 3 mm diameter crystal [7]. This pump setup was implemented in ABAQUS with a super-Gaussian order of 10. The maximum stress intensity was calculated to be 32.6 MPa, which agrees very well with the 33 MPa fracture limit of YLF [1]. LASCAD calculated a maximum stress intensity of 33.0 MPa. Figure 1 shows the stress intensity distribution.



Figure 1: The stress intensity distribution through a slice of the crystal as viewed from the pump face. The maximum stress is 32.6 MPa, while the minimum value is 1.9 MPa. Both figures display the same results, but the figure on the left also shows the finite element grid.

For the time dependant stress analysis, we considered the maximum stress intensity over the duration of a single QCW pulse (Figure 2a).

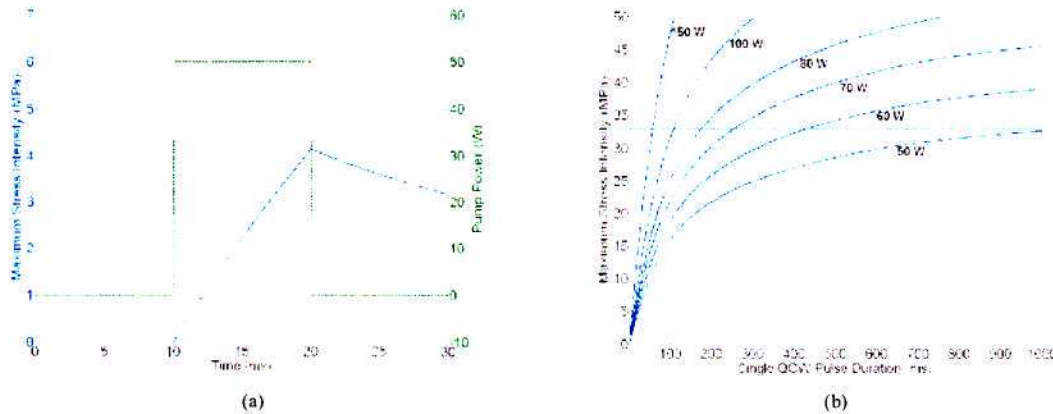


Figure 2: (a) The stress intensity during a single 50 W pump pulse of 10 ms duration. (b) The time dependence of the maximum stress intensity for various pump powers. The dotted line shows the fracture limit of YLF.

From Figure 2a it is clear that the stress increases monotonically while the pulse is present, reaching a maximum at the end of the pump pulse. This makes it possible to model a single "long" pulse and simply consider the time that it takes to reach the fracture limit for a given pump power (Figure 2b).

The time duration to reach the fracture stress was then considered to be the pulse duration that corresponds to that pump fracture power. This allows us to estimate the maximum incident pump power as a function of the pump pulse length, as illustrated in Figure 3.

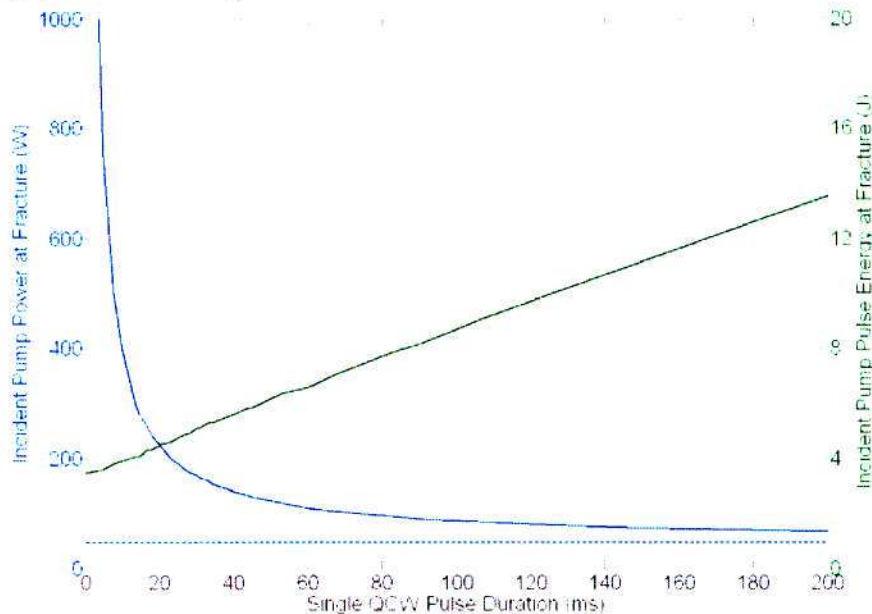


Figure 3: The variation of incident pump power and pulse energy with pulse duration. The dotted line shows the CW fracture limit.

As can be expected, for long pulses the fracture pump power converges to the CW case of 47.2 W, while for a typical QCW pulse duration of 10 ms, fracture occurs at an incident pump power of 395 W, which corresponds to an incident pump pulse energy of 3.95 J.

The maximum temperature at fracture was also considered and it was found that the maximum temperature in the crystal varies from 105 °C for the CW case to 76 °C for a single pulse duration of 347 μ s.

4. Conclusion

To calculate the thermally induced stresses inside a Tm:YLF laser rod numerically, a time dependent finite element analysis was implemented. Firstly the model was validated for the CW pump case by comparing the numerical results with experimental values as well as with a laser modelling software package. This was followed by a time dependent analysis to show the fracture pump power for different pulse lengths.

Future work will include an investigation of various crystal geometries (especially end-pumped slabs) and pump light distributions. A thorough investigation will be conducted to determine the fracture pump power for different pump duty cycles.

5. References

- [1] W. Koechner, *Solid-state laser Engineering* 5th rev and updated ed. Springer series in Optical Sciences Volume 1, Springer-Verlag Berlin Heidelberg, Germany (1999).
- [2] C. Pfister, R. Weber, H.P. Weber, S Merazzi and R. Gruber, "Thermal Beam Distortions in End-Pumped Nd:YAG, Nd:GSGG and Nd:YLF Rods," *IEEE Journal of Quantum Electronics* **30** (7), 1605-1615 (1994)
- [3] W.A. Clarkson, "Thermal effects and their mitigation in end-pumped solid-state lasers," *J.Phys.D: Appl Phys.* **34**, 2381-2395 (2001)
- [4] <http://www.las-cad.com/files/LASCAD-Photonics-West-2005.pdf> (September 2007)
- [5] LASCAD Manual, https://www.las-cad.com/files/PP_FEA.pdf (September 2007)
- [6] http://www.simulia.com/products/abaqus_fea.html (September 2007)
- [7] S. So, J.I Mackenzie, D.P. Shepherd, W.A Clarkson, J.G. Betterson and E.K. Gorton, "A power-scaling strategy for longitudinally diode-pumped Tm:YLF lasers," *Appl. Phys. B.* **84**, 389-393 (2006)
- [8] <http://www.las-cad.com/> (September 2007)

A Time-Dependent Analytical Thermal Model To Investigate Thermally Induced Stresses In Quasi-CW-Pumped Laser Rods

Edward H. Bernhardt^{1,2}, Andrew Forbes^{1,2}, Christoph Bollig¹, M.J. Daniel Esser¹

1. CSIR National Laser Centre, PO Box 395, Building 46, Pretoria, South Africa, 0001

2. School of Physics, University of Kwazulu-Natal, Private Bag X54001, Durban, South Africa, 4000

One of the main problems that limit the power scaling of diode-end-pumped solid-state lasers is the generation of heat inside the laser gain medium which can ultimately cause fracture. When the continuous wave (CW) pump power exceeds the critical power at which crystal fracture occurs, a quasi-continuous wave (QCW) pump is often used to reduce the average pump power to below the fracture pump power.

In previous work, we investigated the time-dependence of the temperature and the thermally induced stresses in QCW-pumped Tm:YLF laser rods by means of finite element numerical simulations [1]. This enabled the prediction of the incident fracture power as a function of QCW-pump duty cycle.

In this paper a time-dependent analytical thermal model that determines the temperature and the thermally induced stresses in isotropic rods is presented. Even though the model is developed for isotropic rods, it is shown that it can also be used to accurately estimate the thermal effects in anisotropic rods. By ignoring axial heat-flow in the radially symmetric rod, the temperature profile on the pumped face of the rod is given by

$$T(r, t) = \sum_{m=1}^{\infty} \int_0^R \int_0^t \frac{2s J_0(\frac{\mu_m r}{R}) J_1(\frac{\mu_m s}{R}) Q(s, \tau) e^{-\frac{D(\mu_m^2 + s^2)\tau}}}{R^2 J_1^2(\mu_m)} d\tau ds \quad (1)$$

where R is the radius of the rod, J_i is a Bessel-function of the first kind with order i , μ_m are the roots of J_0 and $D=k/(\rho c_p)$ with k the thermal conductivity, ρ the density and c_p the specific heat capacity of the laser rod. $Q(r, t)=I(r, t)\alpha/(\rho c_p)$ is the heat load where $I(r, t)$ is the transverse pump intensity profile and α is the absorption coefficient at the pump wavelength. In the case of a top-hat transverse pump profile, equation (1) reduces to

$$T(r, t) = \sum_{m=1}^{\infty} \frac{2w J_0(\frac{\mu_m r}{R}) J_1(\frac{\mu_m w}{R})}{J_1^2(\mu_m) \mu_m R} \int_0^t Q(r, \tau) e^{-\frac{D(\mu_m^2 + w^2)\tau}} d\tau \quad (2)$$

where w is the pump beam radius. The integral in equation (2) can easily be solved numerically for a QCW-pumped laser.

Figure 1 shows the temperature in the centre of the pumped-face of the Tm:YLF rod as a function of time while the rod is subjected to two different QCW-pump power and pulse repetition frequencies. The analytical model reduces the computation time of the thermal effects from ~5.5 hours in the case of the finite element numerical model to less than a minute. By using the analytical model, it is possible to efficiently calculate the thermal influence of various pump scenarios within a short time.

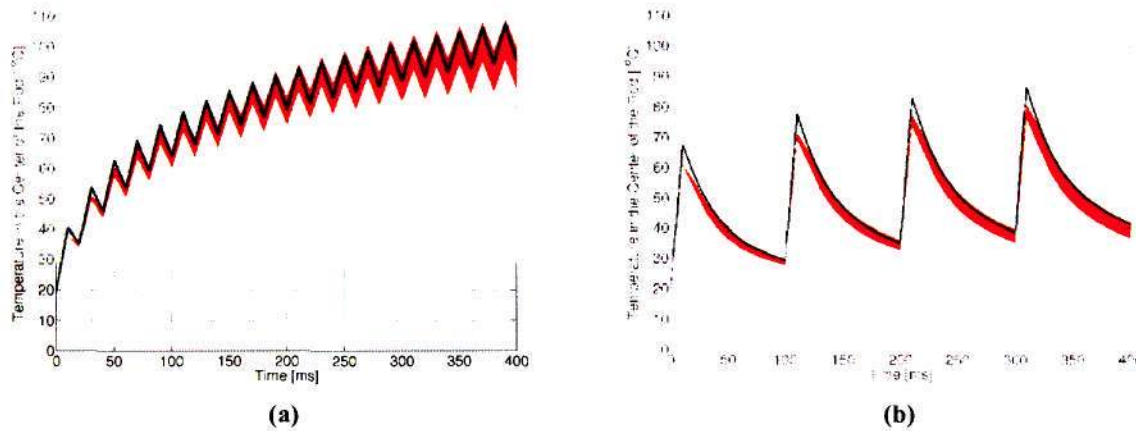


Fig. 1 The temperature in the centre of the Tm:YLF rod as a function of time while the rod is subjected to a QCW-pump of (a) 90 W @ 50 Hz (b) 200 W @ 10 Hz. The two respective boundaries of the shaded regions indicate the analytical solution as determined with the thermal conductivity of the a- and c-axis of YLF respectively. The black curve shows the solution of the three-dimensional time-dependent coupled-thermal-stress finite element numerical simulation.

References

[1] E.H. Bernhardt, C. Bollig, L. Harris, M.J.D. Esser, A. Forbes, "Investigating Thermal Stresses in Quasi-CW Pumped Tm:YLF Laser Crystals", Advanced Solid-State Photonics International Conference, ISBN 1-55752-850-0, 27-30 January, 2008, Nara, Japan